Biomechanical Evaluation of Composite Bone Following Removal of Proximal Femoral Fixation Hardware

by

Janet L. Gbur

Submitted in Partial Fulfillment of the Requirements

for the Degree of

Master of Science in Engineering

in the

Mechanical Engineering

Program

YOUNGSTOWN STATE UNIVERSITY

May, 2011

Biomechanical Evaluation of Composite Bone Following Removal of Proximal Femoral Fixation Hardware

Janet L. Gbur

I hereby release this thesis to the public. I understand that this thesis will be made available from the OhioLINK ETD Center and the Maag Library Circulation Desk for public access. I also authorize the University or other individuals to make copies of this thesis as needed for scholarly research.

Signature:

Janet L. Gbur, Student Date

Approvals:

Dr. Hazel Marie, Thesis Advisor Date

Dr. Daniel Suchora, Committee Member Date

Dr. Virgil Solomon, Committee Member Date

Dr. Peter J. Kasvinsky, Dean, School of Graduate Studies & Research Date

ABSTRACT

Few studies in literature have investigated the performance of bone following the removal of hardware (ROH) in proximal femoral fracture fixations and in particular, the material properties recovered in bone following insertion of bone cement into the holes created by ROH. Cadaveric bones suffer from high inter- and intra-specimen variability; consequently, this investigation utilized composite femurs with a standardized geometry and material properties that approximate healthy human bone. To assess the mechanical response, orthopaedic implants were inserted and removed from the composite bones. Twenty-one femurs were tested in axial compression. Three femurs served as controls (no augmentation) and the remaining eighteen were divided into three treatment groups: cannulated screws, a dynamic hip screw system, and an intramedullary hip screw system. Biomechanical testing of the femurs identified the linear relationship between load/deflection as well as overall load and deflection values at fracture. In addition, strain gages and optical elastography were employed to determine quantitative and qualitative localized strain. Computational modeling led to the development of a preliminary, simplified finite element (FE) model of the femur, which was correlated to experimental data. Overall deflection, stress, and strain were determined, as well as localized strain. Further development and validation of the FE model would allow for investigations into ROH implications for those with varying degrees of osteoporosis.

ACKNOWLEDGEMENTS

My sincerest appreciation to those who have made this project possible.

Thesis Advisor

Dr. Hazel Marie

Medical Advisor

Dr. James A. Shaer, M.D.

Thesis Committee

Dr. Virgil Solomon, Dr. Daniel Suchora

Corporate Partners

Humility of Mary Health Partners, Medical Research Committee

Synthes

Faculty

Dr. Ganesh Kudav, Dr. Robert McCoy, Dr. Elvin Shields,

Anthony Viviano, Dr. Yong Zhang

Additional Assistance

Dennis Gajdos, YSU STEM System Administrator

Amy Johnson, Pacific Research Laboratories

Don Weldon, LPed, LO, CO, Advanced Anatomical Design LLC

YSU Machine Shop

Students

Craig Butrick, Michelle K. Fleming, William Lyons, Mike McCombs,

Adam Palumbo, Rebecca Platt, Michael Sammartino, John R. Seman,

Brandon Strahin, John Terzak, Ariana Zebrasky, Thomas Zebrasky

DEDICATION

First and foremost, I give my love and deepest thanks to my mother and brother, Carole and Brian, who have given their tireless support and unparalleled enthusiasm toward the development and completion of this project. This would not have been possible without your love and encouragement.

Secondly, I give my utmost appreciation and heart-felt thanks to the three most influential professors of my academic career. Dr. Hazel Marie, Dr. Robert McCoy, and Dr. Daniel Suchora, thank you for your never-ending wisdom, your guidance, and your faith in my abilities.

TABLE OF CONTENTS

LIST OF TABLES

LIST OF FIGURES

NOMENCLATURE

Symbol	Description	Unit
ε	Strain	mm/mm
A_0	Instantaneous elastic component of creep	mm^2
$A_1 + A_2$	Creep components	mm^2
t_1	Quick phase time constant for creep	s
t_2	Slow phase time constant for creep	s
σ	Stress	N/mm^2
M_x	Moment	N mm
I_{xx}	Area moment of inertia	mm^4
E	Modulus of elasticity	N/mm^2
y	Distance from neutral axis to extreme fiber	mm
b	Base	mm
h	Height	mm
w	Weight	lbf
t	Thickness	mm
l	Distance to applied load	mm
$\varepsilon_{P, Q}$	Principal strain	mm/mm
$\varepsilon_{1, 2, 3}$	Measured strain, rosette grids 1, 2, 3	mm/mm
$\sigma_{P, Q}$	Principal stress	MPa
γ	Shear strain	mm/mm
A	Area	mm^2
d_o	Outside diameter	mm
d_i	Inside diameter	mm
P	Load	N
δ_{axial}	Axial deflection	mm

CHAPTER I

INTRODUCTION

Proximal fractures of the femur, also referred to as hip fractures, affect a significant portion of the population. It is estimated that as the baby boomer demographic matures, approximately one-third of the population will be over the age of 55 and of those over the age of 65; about 300,000 individuals will suffer a fractured hip (Magaziner et al., 2000). By 2040, the estimates increase to 650,000 hip fractures annually and of those hip fractures, 18-33% of the elderly individuals affected will die within the first year of fixation (Resnick et al., 1992). This certainly dictates a need to monitor the incidence, treatment, and follow up of hip fractures as well as research methods to improve the outcome of treatment.

A myriad of factors can affect the risk of hip fracture including but not limited to gender, race, age, ethnicity, femur and hip geometries, medications, and institutionalization (Koval & Zuckerman, 2000). The most common etiology of hip fractures in the elderly is impact trauma to the femur associated with falling. However, the actual bone failure is attributed more to the induced osteoporotic conditions of the femur, predominately in the elderly and in post-menopausal women (Testi et al., 1999). Osteoporosis is a metabolic condition that is characterized by a decrease in the bone mineral density and can be associated

with a decrease in estrogen production or increased resorption of bone mass (Koval & Zuckerman, 2000). Previous estimates of those diagnosed with osteoporosis just within the United States, Europe, and Japan exceeded 75 million people ("Who are candidates for prevention and treatment for osteoporosis," 1997) and more recent studies have shown that of 9 million new cases of osteoporotic fractures, 1.6 million occur at the hip (Johnell & Kanis, 2006). These statistics, coupled with the fact that even a 10% loss in bone at the hip can result in a 2.5 times greater risk of hip fracture, further cement the need to fully understand the biomechanical response of bone to loads that generate whole bone failure (Klotzbuecher et al., 2000).

While the investigations into the prevention and treatment of hip fractures are numerous in literature, another critical and less investigated area comes to light when the hardware that is used to compress the initial fracture(s) must be removed. Generally, the mechanical support provided by the fixation hardware, if asymptomatic is left in place; however, there are many indications where it requires removal. The decision to remove fracture fixation hardware can stem from implant failure, infection, nonunion of the fracture, and compromised soft tissue (Busam et al., 2006). There is also some debate on the removal of asymptomatic hardware, choosing removal in favor of potential problems with long-term local and systemic effects of the retained metal (Jamil et al., 2008). In either case, with a removal of hardware (ROH), the femur is left with holes formed by the initial insertion of the implants. These holes serve as stress risers and points of potential refracture. As such, an investigation of the biomechanics

of the femur and the understanding of its fracture patterns and fracture treatment devices will aid in determining the response of a loaded bone in both the healthy condition and when holes exist due ROH.

1.1 Femur Biomechanics

To best understand the natural state of the femur, a short introduction to the basic anatomy, tissue composition and location, as well as muscle loading and reaction forces need to be identified. The femur is part of the appendicular skeleton and is the longest and heaviest bone in the human body (Tortora & Anagnostakos, 1987). Classified as a long bone, the femur has a slightly curved shaft designed to absorb the stresses related the body weight. The curve occurs medially, producing a bow of the shaft, bringing the knees closer to the body's line of gravity. The bone is divided into several primary anatomical landmarks. Beginning from the most proximal end in Figures 1.1(a) and 1.1(b), a rounded head articulates with the acetabulum (hip socket) of the hip, followed by the neck, and greater and lesser trochanters, which serve as points of muscle attachment. The diaphysis (femoral shaft) links the proximal femur to the distal femur which is comprised of the medial and lateral epicondyles and finally the medial and lateral condyles wherein the patella surface is located anteriorly. The medial and lateral condyles articulate distally with the proximal tibia.

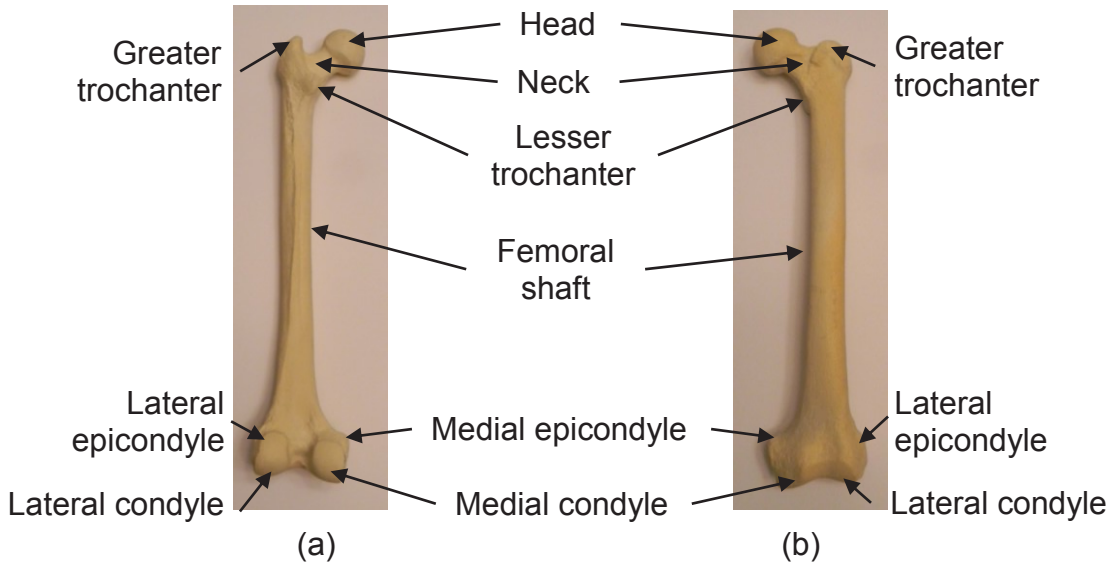

Figure 1.1. Femoral anatomy. (a) Posterior view, (b) Anterior view

Bone, as a material, is considered a composite of calcium hydroxyapatite within an organic matrix. The particular composition of the femur is divided into two types of tissue, cortical and trabecular (cancellous) bone. The cortical bone provides the rigidity and strength to the femur and encompasses the outer shell of long bone. The internal architecture of the cortical bone is composed of longitudinally-oriented osteons consisting of a Haversian (central) canal with concentrically arranged lamellae (rings), lacunae (hollow space containing bone forming cells), osteocytes (mature bone cell) and canaliculi (channels). The collective Haversian system serves as the strength behind the tissue and dictates its mechanical properties (Seligson, 1985). Behaving similar to wood, cortical bone is anisotropic and exhibits much greater strength in the longitudinal direction. Conversely, cancellous bone is a three dimensional network of interconnected rods and plates dividing into various pores providing a structure that varies in density and porosity. The classification of the bone tissue is based

on a relative density ratio wherein the density of the specimen is compared to that of fully dense cortical bone, which is assumed to have a density of 1.8 g/cc (Mow & Huiskes, 2005). This produces a range of relative densities for cancellous bone from 0.05 to 0.7 and a cortical bone range from 0.7 to 0.95 illustrating that the distinction between the denser cancellous tissue and low-density cortical tissue is somewhat ambiguous. In the intertrochanteric region of the femur, located from the neck through the trochanters to the shaft, Figure 1.2(a), the bone tissue consistency is characterized by a higher-density cancellous bone that serves to transmit and distribute stress. This tissue contains dense trabeculae (latticework) in discrete patterns having assumed functions of principal tensile and compressive trabeculae during load transfer within the proximal femur, Figures 1.2(b)-1.2(d). This network was first identified by Wolff, who postulated that bone structure corresponds to bone function (Rudman et al., 2006). The final structures to note within this proximal region are the medial femoral cortex, a very thick section of cortical bone at the level of the lesser trochanter, and the calcar femorale, a vertical wall of extremely dense cancellous bone on the posteromedial aspect of the shaft (Rudman et al., 2006). The medial femoral cortex is best viewed from the anteroposterior (AP) view and the calcar femorale, best viewed laterally, aids in redistributing loads from the femoral head to proximal shaft. Finally, extending from the lesser trochanter to a distance of approximately 5 cm distally is the subtrochanteric region which is characterized by an area of thick cortical bone that allows for transmission of both axial and torsional loads (Koval et al., 2000).

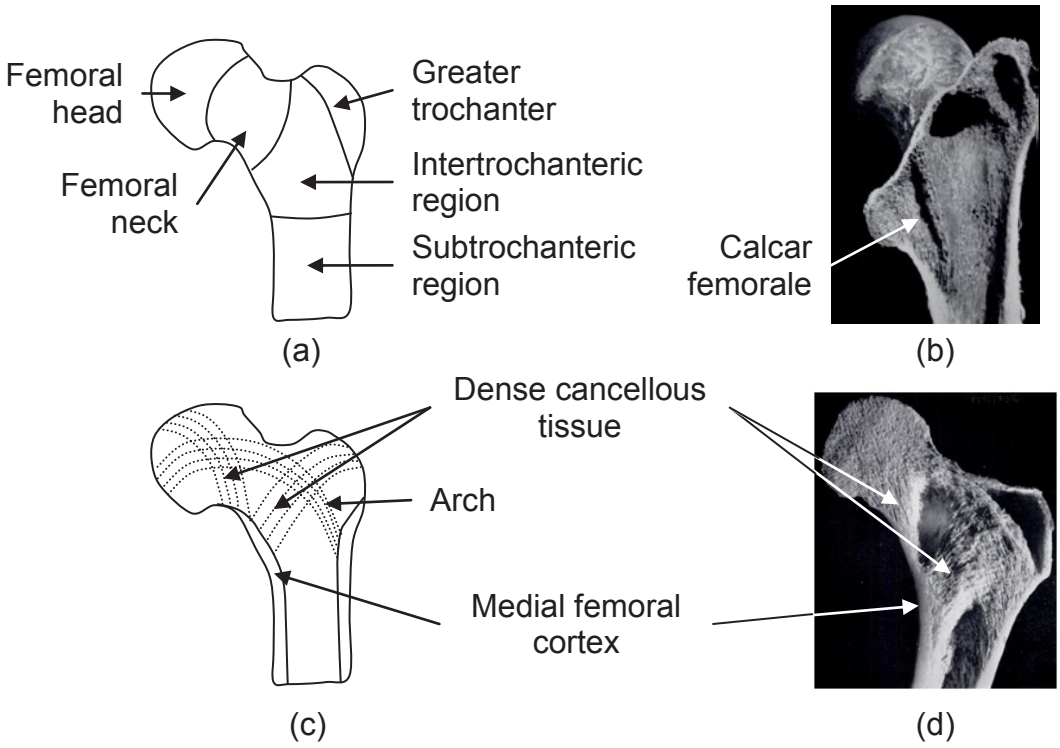

Figure 1.2. Proximal femur regions. (a) Anatomical sections, (b) Lateral bisection (Garden, 1961), (c) Diagrammatic cross section, (d) Cadaveric cross section (Garden, 1961)

Whole bone strength varies according the type of bone, location within the body, age, sex, physical activity, as well as overall health of the individual. A large collection of studies have investigated the changing composition and mechanical properties of bone throughout the aging process. Of particular interest is the decrease in mechanical properties of bone in general as a person ages, Table 1.1 (LeVeau & Williams, 1992). Findings have shown that with an increase in age the yield stress, ultimate tensile stress, compressive stress, elastic modulus, ultimate strain, and energy absorption of the femur decreases.

Table 1.1. Changes in bone properties with age.

	0-9	*10-19*	*20-29*	*30-39*	*40-49*	*50-59*	*60-69*	*70-79*
Ultimate tension (MPa)	-	116.0	125.0	122.0	114.0	95.0	88.0	88.0
Ultimate compression (MPa)	-	-	170.0	170.0	164.0	158.0	148.0	-
Ultimate percent elongation	-	1.5	1.4	1.4	1.3	1.3	1.3	1.3
Bending (MPa)	174.6 -	193.3 -	202.1 212.0	221.9 212.0	- 199.0	- 190.0	- 181.0	- 165.0

Data from Yamada, 1970; Currey and Butler, 1975; Noyes and Grood, 1976; Burstein et al., 1976.

Additionally, the material properties of long bone tissue and an understanding of how the bone is naturally loaded are important for subsequent stress analysis. The hip joint is a statically indeterminate system due to the fact that the number of forces acting across the region exceeds the number of equations from static equilibrium available to solve the problem (Bartel et al., 2006). As such, the musculoskeletal analysis of the femur has taken on many forms from two-dimensional (2D) static analysis to three-dimensional (3D) nonlinear dynamic analysis. Models have ranged from considering the simple femur itself to the inclusion of forces generated across the femur from the surrounding muscle and soft tissue.

Koch and Pauwel, individually, performed some of the initial investigations quantifying the stresses within the proximal femur, and their work is regarded as foundations for the classical approach to stress analysis in the proximal femur (Mow & Huiskes, 2005). Koch was the first to quantify load transfer within the femur by calculating the internal forces using beam theory and omitting the effect of musculature and surrounding soft tissue. His resulting work correlated with the description of the internal architecture originally identified by Wolff. Pauwel was

the first to include muscle groups in the analysis and also confirmed tensile stresses on the lateral surface and compressive stresses in the femoral neck and shaft medially. Additional work confirmed that a band of soft tissue between the greater trochanter and femoral condyles greatly reduced the bending moments imposed on the femoral shaft (Mow & Huiskes, 2005). His studies also led to an estimation of a resultant force of three times the body weight in magnitude on the femoral head from the 2D analysis of the inclusion of the gluteus medius muscle group and body weight (Imura, 1993).

Rudman et al. (2006) developed a 2D finite element model including the acetabulum, proximal femur, and ligaments of the hip. Both one-legged and two-legged stances were investigated through the use of a finite element model. A joint reaction force for the one-legged stance was calculated to be 3.6 times the body weight. Results showed that the arch-like trabeculae in the proximal femur act in compression and function similar to a flying buttress that transfers the loads from the proximal femur to the femoral shaft, Figures 1.2(c) and 1.2(d).

Duda et al. (1997) took into consideration the collection of all muscles and soft tissues as well as joint reactions at the hip, patella-femoral, and knee during various stages of the gait cycle while evaluating the load state at different locations within the femur. Analysis was performed with force/moment equations and compared to literature. The findings indicated that the muscles play a significant role in balancing the loads within the femur, indicating that the bone is loaded axially rather than in bending and that the maximum shear forces occur at the proximal and distal ends of the bone.

The models discussed simply provide a range of loading scenarios that have been investigated, understanding that numerous other variations have been studied according to the choice of muscle reduction and static versus dynamic loading. Thus, both computational and experimental studies have limitations due to the assumptions taken in creating the model. For example, while a great deal of evidence supports that the muscle and surrounding soft tissue contribute to the loads incurred by the femur, the actual applied forces are not known *in vivo* which makes it to difficult know just how accurate the assumed muscle forces are and their collective contribution on the femur (Mow & Huiskes, 2005). Therefore, in developing a model for analysis it is important to address the known limitations of creating an *in vitro* model, how it can be validated, and what relevance the results have when applied to a clinical situation considering the high variability of an *in vivo* model.

1.2 Proximal Femoral Neck Fractures

Failure of bone tissue can be the resultant of either instantaneous or fatigue fractures of the tissue. At any given time, bone in a healthy state contains numerous microcracks due to fatigue of the tissue under repetitive loading, but these cracks are generally repaired in the natural process of bone remodeling (Mow & Huiskes, 2005) and contribute to the toughening of the bone through stress redistribution (Sobleman et al., 2004). However, if the mechanical load exceeds the equilibrium that exists for remodeling, then the microcracks accumulate and can lead to whole bone fracture. Failures due to these

fluctuating forces of lower magnitudes over time are primarily related to the internal structure of the bone and can lead to stress fractures of the femur (Simon, 1994). Alternatively, an instantaneous failure results from the rapid accumulation of damage in the tissue wherein the tissue does not have time for ample repair, leading to a fracture. In this instance, the force applied could be compressive, tensile or shear or some combination of the three. In long bones, several general patterns characterize the mode of failure. For the purpose of this study, the patterns with the most significance are those related to the oblique and transverse simple fractures occurring by bending forces in the shaft and fractures occurring by shear forces in the neck, Figures 1.3(a) and 1.3(b). There are several different classification schemes of fractures according to their location across the femoral anatomy. For this study, only fractures relating to the proximal femur are considered, and because this work investigates the load to failure of the femurs, only completely displaced fractures are illustrated in this section.

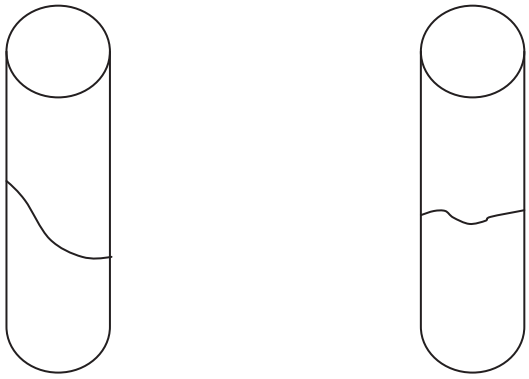

Figure 1.3. Simple fracture patterns of femoral shaft. (a) Oblique, (b) Transverse

Femoral neck fractures are categorized based on the anatomic location of the failure. Pauwel's classification characterizes the fracture by the angle of the

fracture to the horizontal plane: Type I-30°, Type II-50°, Type III-70°, Figures 1.4(a)-1.4(c), (Mostofi, 2006). In general, the more vertical the fracture angle is across the neck the more that shear forces are considered the primary basis for the failure.

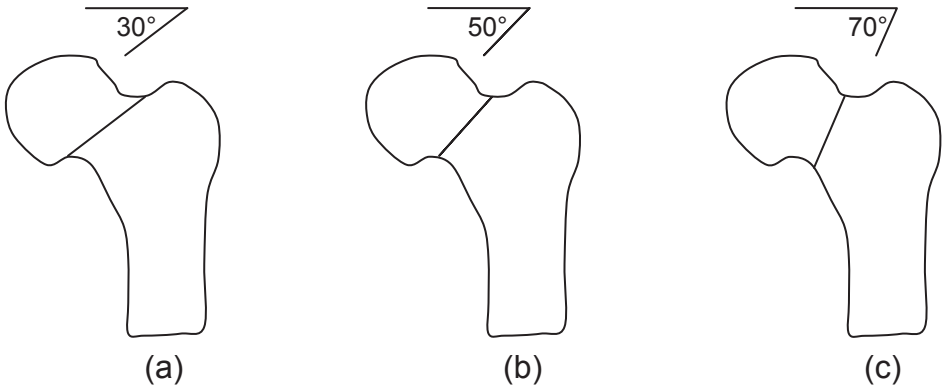

Figure 1.4. Pauwel's fracture classifications. (a) Type I, (b) Type II, (c) Type III

Common non-neck femoral failures include intertrochanteric, basicervical, and subtrochanteric fractures. Intertrochanteric fractures arise as a single fracture along the intertrochanteric line of the proximal femur, Figure 1.5(a). Basicervical fractures occur at the base of the femoral neck and can be difficult to distinguish between intertrochanteric fractures, Figure 1.5(b). Subtrochanteric fractures can occur at various levels below the lesser trochanter and are typed according the relation of the primary fracture line to the lesser trochanter, Figure 1.5(c). The subtrochanteric fractures classified by Fielding identify the level of the lesser trochanter as Type I, between the lesser trochanter and 2.5 cm below it as Type II, and those ranging from 2.5 cm to 5 cm below the lesser trochanter as Type III (Mostofi, 2006).

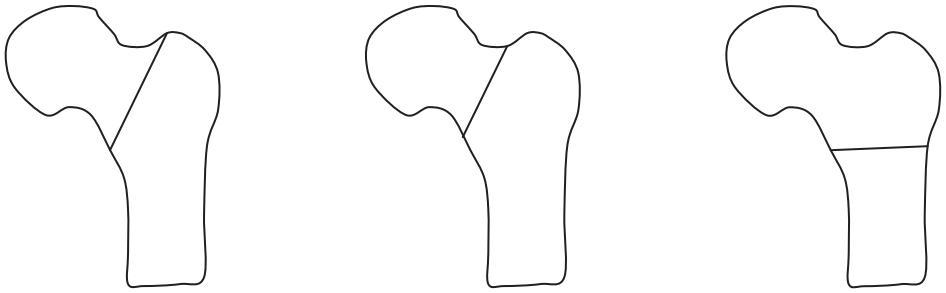

Figure 1.5. Non-neck proximal fractures. (a) Intertrochanteric, (b) Basicervical, (c) Subtrochanteric

A general understanding of the fracture patterns observed clinically in proximal hip fractures and the conditions in which they occur biomechanically aid in analyzing the resulting fractures created through the load to failure tests performed in this study. Beyond the description of the femur's biomechanics, some understanding of the fracture fixation treatment devices is beneficial. The mode and location in which the hardware is applied in order to compresses the fracture can also impose local stresses on the bones. Furthermore, in some cases where removal of hardware is indicated, only a portion of the hardware is retained which can also contribute to additional local stresses.

1.3 Proximal Femoral Fixation

Three types of proximal fracture fixation devices were considered in this work and included cannulated screws, a dynamic hip screw (DHS) system, and an intramedullary hip screw (IHS) system, Figures 1.6(a)-1.6(c). Screws are used to achieve stability of the fracture by compressing the fragments and neutralizing the forces and moments acting across the site (Mow & Huiskes, 2005). The

cannulated screws are inserted in an inverted triangular fashion and are used to compress femoral neck fractures and intercondylar femoral fractures, Figure 1.6(a). A compression plate and screw system is indicated in intertrochanteric fractures, Figure 1.6(b). The plate is used in conjunction with a lag screw in order to neutralize any bending, rotational or axial stresses on the already compressed fracture site (Egol et al., 2004). The intramedullary hip screw system, and more particularly the trochanter fixation nail (TFN), consists of a nail that is used to internally splint the femur, a distal locking screw, and a lag screw or helical blade that penetrates the head and neck to compress the fracture site, Figure 1.6(c). The screw allows for a controlled head and neck collapse while the nail that is situated within the medullary canal lessens the lever arm on the proximal fragment compared with that found in the plate system (Chirodian et al., 2005). The TFN is used to treat pertrochanteric, intertrochanteric, basal neck, subtrochanteric fractures and combinations thereof (Lenich et al., 2006).

Figure 1.6. Fracture fixation hardware. (a) Cannulated screw, (b) DHS, (c) IHS

1.4 Removal of Hardware

As mentioned previously, several indications exist wherein the hardware utilized to fix the femoral fracture must be removed either partially or in its entirety. Agreement for removal is generally met when the indications include nonunion, infection, implant failure, soft tissue injury, or chronic pain. For example, Haidukewych and Berry (2003) reviewed sixty cases of failed treatment of intertrochanteric hip fractures for consideration for salvage hip arthroplasty, finding that twenty-one of the patients experienced “cut out” of the hardware (migration of the screw and extraction) from the femoral head. However, removal of asymptomatic hardware is met with some debate as the removal process introduces a new set of concerns including but not limited to risk of refracture, neural injury, stress risers left by the removed hardware, and economic implications (Jamil et al., 2008). Statistically, about 5% of all orthopaedic procedures in the United States are related to ROH, and in a Finnish study following a seven year period at one institution, 81% of all fracture fixation hardware implants were removed (Busam et al., 2006). Though ROH is considered a common procedure, few studies have addressed the question as to whether or not asymptomatic hardware should be removed and what indications exist that would support the ROH.

Brown et al. (1993) studied the case notes for 266 fractures wherein 42% of the cases underwent ROH in the upper and lower extremities and of those cases, 19% encountered additional complications. Patients with proximal femoral fractures were not included in the study since the primary occurrence was in the

elderly population. However, data does include both femoral shaft and subtrochanteric fractures. Of the thirty-four femoral shaft fractures, twenty-two removals occurred and eleven of those experienced pain related to at the nail insertion site secondary to screw cut out. Based on their analysis of the cases, no conclusive evidence supported routine removal of hardware; rather, the risks associated with ROH far outweighed the theoretical disadvantages of the retained metalwork.

Hanson, van der Werken, and Stengel (2008) surveyed 730 attendees at the AO Principles and Masters Courses of Operative Fractures Treatment and of the respondents, 58% did not agree that routine ROH is necessary and 49% did not agree that retained implants pose an excess risk of any adverse effects. Of those surveyed, 48% felt that the risk incurred by ROH exceeds any risks to retaining the hardware, and 85% agreed that there is a significant economic burden on hospital resources to perform ROH. No current method of controlled trials exist to compare the benefits and risks of ROH; there also lacks a method wherein a surgeon can identify which patients can benefit most from ROH.

Busam et al. (2006) performed a review of literature and discussed concerns regarding particular types of ROH recommending that research be developed in the areas of economic impact and variations of the practice of ROH. Addressing the concerns of refracture surrounding the implant, studies showed that implants left in longer achieving complete fracture union and remodeling can minimize the risk of refracture. The introduction of stress risers following ROH, which have been reported to decrease load to failure by as much as 22% in

cadaver calcanei, are of significant concern immediately and upwards of four months post-ROH. However, new bone from remodeling lessens the stress-concentration effect over time. Since the bone tissue appears to remodel any deficit within two to four months after ROH, the decision to proceed with ROH or retain the hardware cannot be based on the risk of refracture alone. Other considerations include pain (highly variable from patient to patient, no guarantee of outcome), metal allergy (no current correlation exists with positive skin patch sensitivity test and increased implant failure), carcinogenicity (risk is very small), as well as other factors such as metal detection, fixation across joints, and pediatric removal. Finally, surgical considerations with ROH were also addressed. Data compiled showed a 3% complication rate from a study of 86 patients (Richards et al., 1992) and a 20% complication rate from a study of 188 patients (Sanderson et al., 1992) with the most common complications being infection and nerve injury. This further reinforces the notion that the inherent risks and benefits need to be well understood in regard to ROH and that further research into the expected benefits and details of removal is essential.

Jamil et al. (2008) surveyed 345 orthopaedic surgeons in the United Kingdom in order to estimate the current practice of ROH. Just as in other similar surveys, ROH indications included localized pain, loosening of hardware, infection, metalwork damage, skin irritation, periprosthetic fracture, and functional limitations. Retention of hardware was indicated as a potential stress riser as stress shielding can occur locally weakening the bone, whereas holes left by ROH can reduce the rotational strength and energy absorbing capacity of the

bone. From the survey, only 7% replied that there was a departmental policy on the ROH, leaving the majority to decide based on individual judgments.

Additional clinical studies by Gosling et al. (2004), Minkowitz et al. (2007), Richards et al. (1992), and Kukla et al. (2001) further reinforce the ambiguity regarding asymptomatic removal versus retention and confirm indications of ROH. Gosling et al. (2004) analyzed how various factors influenced the operation time of ROH in femoral nails and whether those who were asymptomatic prior to surgery would become symptomatic. One hundred forty-nine patients were included in the study of which fifteen had bilateral implant removal for a total of 164 removed nails. Most of the patients were advised to undergo ROH as a routine procedure and 20% of the asymptomatic patients experienced long term complaints following ROH. Their collective findings indicated that only symptomatic patients should be considered for ROH and all patients need to be strongly educated on the amount of potential soft tissue damage incurred by the procedure and that complications can arise leading to additional hospitalizations.

The study by Minkowitz et al. (2007) followed 60 patients who had been previously treated for fixation and indicated pain in the region. Of those, 53% reported a decrease in pain and 44% noted an improvement in function following the removal of hardware noting very positive outcomes for ROH.

Further supporting routine ROH is the study by Richards et al. (1992) that followed 88 patients with both symptomatic (53%) and asymptomatic hardware. Pain was recorded as the primary complaint in 65% of the symptomatic cases.

Relief from pain was observed in 91% of these cases following ROH and 95% of the asymptomatic cases were without complications.

Kukla et al. (2001) analyzed 1,334 patients with a standard gamma nail (SGN). Thirty-seven underwent ROH and of those three experienced medial neck fractures post-operatively. Over the same period, forty-one of 1,219 patients with a DHS underwent ROH and none involved secondary fractures. Further *in vitro* experiments yielding lower failure loads led the researchers to summarize that implants used to stabilize proximal femoral fractures should not be routinely removed. If ROH must occur, specific attention should be paid to the implant design effect on the hole and consider replacing the symptomatic hardware or implanting bone substitution material in the cortical defect.

In all, the case as to when and even whether asymptotic hardware should be removed is open for debate. Furthermore, guidelines for ROH not only do not exist, but the manners in which the defects left by the ROH are treated clinically are minimally investigated in literature.

Cortical defects either due to simple removal or due to implant failure still equate with a loss of bone mass and/or bone deformity and, as such, affect the overall structural integrity of the whole bone. Theoretical analysis of the residual hole as a stress concentration in the bone has shown to reduce the local strength by a factor of three. Additionally, experimental studies have revealed that while small holes have a minimal effect on long bones, as the size of the hole is increased relative to the bone diameter, the torsional strength decreases upwards of 40% (Bartel et al., 2006). Some studies have explored the response

of bone following ROH using both animal and cadaver models all confirming a loss of whole bone mechanical properties.

Rosson et al. (1991) utilized a rabbit model to quantify the weakness of bone following ROH. A cortical atrophy model was developed with rabbit tibiae to serve as comparison to the residual screw holes to determine if the weakness was due to stress shielding from the removed metal plating or due to the hole left behind by the screw. Matched-pair tibiae were treated and assigned to one of three groups using one bone for testing and the contralateral bone as the control: partial demineralization, holes in normal bone, and partial demineralization with holes. Holes of 1.5 mm, 1.5 mm tapped to 2.0 mm and 2.0 mm diameters were drilled 45° to the axis of the applied load. No hole exceeded 30% of the diameter of the bone. Loads were applied in three-point bending at a rate of 0.5 cm/min. The reduction of mineral content (75%-85% of normal mineralization) resulted in a reduction in maximum bending (75% of normal) but only a small reduction in energy absorption (95% of normal). In contrast, while the residual hole reduced the bending moment to 70% of normal, and the energy absorbing capacity was significantly less (53% of normal). Considering that the bending moment is reflective of static strength (i.e. maintaining body posture) and that the energy absorbing capacity takes into account the maximum bending moment and degree of deformation at failure, the reduction in strength was attributed to the cortical hole defect.

Remiger et al. (1997) investigated the effects of bicortical (penetrating bone cortex twice) and unicortical (penetrating bone cortex once) screw holes

created from plate removal in a sheep model. Thirty-six paired sheep tibiae were divided into categories of control vs. unicortical holes, control vs. bicortical holes, and unicortical vs. bicortical residual holes. All bones, tested in torsion, fractured in spiral fashion in the distal third of the bone, and results showed that groups with screw holes fractured through at least the distal hole. A reduction in torsional strength occurred in all groups and was reported as follows: unicortical-reduction by 21.6% of control, bicortical-reduction by 31.4% of control, and bicortical-reduction by 26.7% of unicortical. The decrease in bone strength was due to the presence of the residual hole(s), which created a reduction of bone mass and development of a stress concentration site.

Miller et al. (1993) performed a study using paired cadaver femora to determine the effect of the entry hole for an intramedullary nail on the strength of the femur. Fifteen pairs of femora were divided into three groups with the right femur serving as the control: 10 mm hole in ideal location, 14 mm hole in ideal location, and a 14 mm hole anterior to the ideal location. Strain gages were placed on the superior and inferior aspects of the neck, the femur was oriented to simulate a two-legged stance, and the bone was distally cemented in polymethylmethacrylate (PMMA). Modes of failure were consistent: the control femora exhibited an oblique subcapital fracture while all left femora, regardless of the hole size or placement, exhibited a basicervical fracture through the hole. The loads at failure of the groups with holes in the ideal locations were similar to each other and to the mean of the control. However, the group with the anteriorly placed hole failed at a mean two-thirds of the control values. No significant

differences in the strains were identified between any of the groups or with the controls. The results suggest that the placement of the hardware has a more critical effect on the strength of the bone than the size of the hole.

Kukla et al. (2001) in addition to the retrospective study of 1,334 patients with proximal femoral fractures, they designed a study with eighteen matched pair cadaver femurs to explore the response of bone following the removal of both SGN and DHS implants. One femur of each pair was used for testing and the contralateral femur served as the control. Femurs were assigned to one of three groups: SGN and removal, DHS and removal, or complete excavation of the femoral neck. The femurs were oriented in 12° adduction, distally fixed in an aluminum cylinder with potting plaster and placed under a compressive load through the femoral head at 10 mm/min to a body weight of 800 N. Incremental loads were then applied sinusoidally at a rate of 1.0 Hz, advanced in 25 N increments, and cycled until fracture. The baseline load applied was representative of a body weight and the chosen increments simulated the gradual increase in weight bearing post-surgery. The mean load at fracture of the control group was 5,751 ± 1,563 N and 4,406 ± 1,025 N for the DHS, 3,789 ± 851 N for the SGN, and 3,956 ± 2,240 for the excavation group. To determine the cycles to failure, the baseline load for the first cycle was 80 kg (800 N) and was increased an average 2.46 kg (mean 24.6 N) per cycle. Each loading increment represented one cycle, so the total number of cycles at failure was calculated by taking the load at failure and dividing by 24.6 N. All contralateral femurs failed similarly in the medial neck and those in the treated group failed primarily as a

medial neck fracture (twelve) with three displaying combined failure and the remaining three failing at the subtrochanteric level. It was postulated that complication rates vary greatly with implant design. The researchers concluded that the DHS system, which features a hip screw diameter of 8 mm, experiences a low complication rate relative to the SGN, which has a screw diameter of 12 mm. Overall, the treated femurs experienced a 34% decrease in strength compared to the control femurs.

Some limited studies also investigated the response of bone if the residual holes left by ROH were augmented with some form of cement or resorbable filler. PMMA (compressive strength 70-120 MPa) and injectable tricalcium phosphate cements (TCP-compressive strength 55 MPa) have been used to fill bony defects and improve fixation of hardware (Collinge et al., 2007). PMMA, while increasing holding power of the implant, exhibits several disadvantages including difficult handling properties, thermonecrosis, and difficulty in removal. Furthermore, it is not resorbable bone tissue. The TCP cements are non-exothermic and cure *in situ* forming an osteoconductive carbonated apatite similar to the mineral phase of bone (Strauss et al., 2007).

Strauss et al. (2007) investigated the effect of calcium phosphate cement augmentation of residual holes left by DHS removal in eight matched cadaver femurs. All femurs were drilled for the lag screw, the femoral condyles removed, then potted at 25° adduction in a steel tube with acrylic cement. One of each drilled pair was filled with cement and left to cure in a 37°C water bath for 24 hours. A compressive load of 750 N was applied cyclically through a polished,

flat applicator to the femoral head at a rate of 3 Hz for 1,000 cycles to simulate early weight-bearing. Each femur was then loaded axially at a rate of 10 mm/min until failure. Failure was defined as a 10% or more reduction in load borne by the sample. Mean load to failure for the cemented-filled holes was reported as 4,819 N (2,562 to 6,859 N), while the untreated holes failed at a mean of 3,994 N (1,833 to 5,382 N). All fractures occurred through the femoral neck (six cement/four control fractured through the neck center, one cement/one control fractured subcapital, one cement/two control fractured basicervical). The addition of cement to the residual holes created a 21% increase in the mean load to failure.

Alford et al. (2007) developed a rabbit model to evaluate the effect of resorbable fillers on the holes left by the removed screws. Seventy-five paired rabbit femurs were obtained and drilled for screws where one of each pair was treated either with a metal screw or resorbable bone screw, and the contralateral femur was left empty. Bones were drilled with a 2 mm bicortical hole in the femoral shaft comprising approximately 20% of the overall midshaft diameter. The femurs were either harvested initially, or left for healing and harvested at one week or at thirteen weeks. The specimens, once harvested, were cleaned of soft tissue then both bone ends were potted in PMMA maintaining a 45 mm gauge length of free bone between the potting surfaces. The femurs were tested in torsion at a rate of 10° per second and data was recorded at 200 Hz. At time zero (initial harvest), the resorbable filler produced an increase of 23% torque to failure and a 73% increase in the amount of energy to failure. In comparing the

resorbable fillers to their empty counterparts, an increase in peak torque and energy to failure occurred at week one but was not significantly different at week thirteen. The only significant change with the metal treatment occurred at week one, seen by an increase in energy to failure, while no significant change was noted in week thirteen. No change in stiffness occurred throughout the study between the metal and resorbable-filled femurs.

These studies illustrate the complexity of ROH both from a clinical and a biomechanical perspective. High variability exists with both forms of investigation and unlike many traditional mechanical and material property studies in engineering; standards do not exist to guide experimental model development. The use of a cadaveric model, animal or human, presents challenges due to high inter-specimen and intra-specimen variability of geometries and material properties. Therefore, the ability to develop experimental protocols and yield high reproducibility becomes exceptionally difficult. One solution to the variability problem has garnered significant attention as well as some controversy and that is the use of composite bones in place of a cadaveric model.

1.5 Composite Bone

Composed of a glass reinforced epoxy, the first mechanically realistic simulated cortical bone was introduced in 1987 (Heiner, 2008). Later refinements to the model led to the subsequent introduction of fiberglass-fabric-reinforced (FFR) bones and short-glass-fiber-reinforced (SGFR) epoxy. The most current composite model is a combination of short-fiber-filled-epoxy (simulated cortical

bone) and rigid polyurethane foam (simulated cancellous bone). The model is manufactured under the trade name Sawbones (Pacific Research Laboratories, Inc., Vashon, WA). Several researchers have performed material characterizations on the composite femurs to determine the performance under a variety of loading conditions and have compared the values to the range of those exhibited by healthy human cadavers.

Szivek and Gealer (1991) performed the first study of the second generation Sawbones (FFR) and the deformation response was compared to cadaveric femurs during a one-legged stance loading scenario. Six composite bones and two cadaver bones were instrumented with five biaxial strain gages (proximal shaft-medial, lateral, posterior, and inferior; neck-anterior), one uniaxial strain gage (proximal shaft-anterior), and one strain gage rosette (neck-posterior). The testing apparatus was designed to apply a compressive load to the head and tensile load to the trochanter causing both bending and axial loading of the proximal femur. The condyles were potted in Cerrobend to hold the bone in 10° adduction. The femoral head was fitted to a polyethylene insert inside an aluminum fixture mimicking the ball-and-socket function of the joint. A loading frame was designed to simulate the force of the adductors on the greater trochanter through the attachment of a transcortical rod. Load was applied at a rate of 1,100 N/s to a peak load of 1,000 N. Each femur was tested three times except one cadaver femur which failed after the first test. A comparison of the average strains indicated that all six composite bones were less stiff than the cadaver bones. Laterally, the strains ranged from 2,166 με to 3,176 με in the

composite model compared to the 1,439 με and 2,386 με found in the natural bone. As a result, the exact *in vivo* strain of a femur could not be determined from this composite model, however the composite bones could be used to determine how implants affect the strains pre and post-insertion.

Mechanical validation of another early composite bone was investigated by Cristofolini et al. (1996). Comparisons of fresh-frozen cadaver femurs, dried-rehydrated cadaver femurs, and composite femurs were developed through measuring the femoral head deflection under axial load, the strain distribution under axial load, the bending stiffness, and the torsional stiffness. Two composite femurs were outfitted with twenty uniaxial strain gages placed parallel to the longitudinal axis on the anterior, posterior, medial, and lateral proximal surfaces. A load of 1.6 kN was applied cyclically for ten cycles to identify any mechanical conditioning effects by physiological loading. Next, loads were incrementally applied in amounts of 0.1 kN up to 1.6 kN for linearity tests and finally a creep test was performed with a 1.6 kN load and ramp of 15 s applied and held for fifteen minutes then removed with a 15 s ramp. To measure axial deflection, eight composite femurs, four fresh-frozen femurs, and four dried-rehydrated femurs were obtained, imprints of the head and condyles were made, femurs were oriented in 11° adduction, and loaded axially with a 10 s ramp up to a 0.8 kN load. Each bone was tested ten times. In addition, twelve femurs (four of each type) were loaded in four-point bending then followed with torsional testing. The results showed that no mechanical conditioning had occurred and that the mechanical response of the femurs was linear in nature. Some creep was

observed with a maximum creep velocity of 1.5 με s^{-1} and decreasing rapidly after load application. Within the first 15 s of applied load, strain variations were recorded up to 6% of the initial with 65% of the creep occurring within three minutes. The researchers' second-order model of creep response to a step load was given by:

$$\varepsilon(t) = A_0 - A_1 e^{-t/t_1} - A_2 e^{-t/t_2} \quad (1.1)$$

The equation points out that there are two distinct phases of creep occurring during the axial loading, a quick phase (time constant t_1 in the range of 20-40 s for all strain gage positions) and a slow phase (time constant t_2 ranging from 5-10 min). The sum of the creep terms, A_1 + A_2, was always less than 8% of the instantaneous elastic component, A_0. In regard to the strain variations, there were some abnormalities observed medially and laterally which were suggested to be attributed to the epoxy's inadequate amount of glass fiber in this area, as verified by X-rays. The femurs were found be comparable geometrically, and they performed in appropriate cadaver ranges for head deflection, bending and torsion. Minor disadvantages were the finding of some local abnormality in the strain distribution and that some time (e.g. four min) needed to be allotted for the settling of the viscoelastic effect when measuring strains.

Heiner and Brown (2001) performed some of the early comparative analysis between the FFR and SGFR generations of Sawbones proposing that the SGFR embodiment would be a superior cortical analogue structurally and possess stiffness values within the range of human femurs. The SGFR models allowed the manufacturer to more closely replicate the anatomical geometry by

having the ability to better smooth out the mold surface texture. This led to improved anatomic detail, the addition of an intramedullary canal, and change from a circular diaphysis to a more realistic oval diaphysis. Axial, bending and torsional loading of six FFR and six SGFR medium femurs were performed and compared to each other and to that of natural bone. For axial testing, the femurs were distally potted, held at 11° adduction, and a compressive load was applied at 60 N/s for up to 600 N, then removed for two pre-conditioning cycles and eight additional cycles. Axial strains were measured on the medial aspect of the femurs with five linear strain gages equally spaced from the lesser trochanter to mid-shaft. Mean axial stiffness was reported as 1,895 N/mm for the FFR femurs and 1,635 N/mm for the SGFR femurs. Compressive strains decreased proximally to distally with both models with the recorded strains from the FFR at the most proximal gage recorded as 649 με and 1,225 με for SGFR. Overall, the SGFR analogs were an improvement to the FFR models due to more uniformity of geometry, increased anatomical accuracy, and decreased variability compared to cadaveric bone. However, concerns arose with significantly less stiff values and high compressive strains along the proximal-medial region of the lesser trochanter. A fourth generation of the SGFR now available shows improvements with better fracture and fatigue resistance and an increase in the tensile strength, tensile modulus, compressive strength, compressive modulus, thermal stability, and moisture resistance. The biomechanical characterization was again performed by Heiner (2008). The obtained values from the fourth generation models more closely matched those of fresh and frozen cadavers reported in

literature. Testing procedures were analogous to those used in the initial study (Heiner & Brown, 2001). Results of the fourth generation composite femur were more closely aligned with those reported in natural femurs. Strain values from the most proximal gage were reported as 708 με compared to 1,193 με with the third generation and 633 με for natural bone.

Papini et al. (2007) performed one of the first studies to measure the axial and torsional stiffness of cadaver femurs, compared results to third generation Sawbones and develop an analogous finite element (FE) model considering both healthy and poorer quality bone. Twenty-five cadaveric femurs and three large third generation composite femurs were tested in axial compression, bending and torsion. For axial testing the head of the femur was free to rotate, similarly to a ball-and-socket joint and the distal femur was pinned by a series twelve screws. The FE solid model was generated by computed tomography (CT) scans of the three composite bones, imported into Ansys 8.1 and meshed with tetrahedral elements-found from previous studies to be most optimal in femoral modeling. The simulated bone tissue was assumed to be linear elastic and isotropic. From their preliminary work, it was discovered that the removal of elements representing cancellous bone resulted in FE predicted axial stiffness, torsional stiffness and rigidity within 1% of those determined within the inclusion of the cancellous elements. The model was run neglecting the cancellous portion of the bone and Young's modulus of the cortical portion was varied in the range of 4-10 GPa to simulate poorer quality bone (healthy cortical range 11.4-19.7 GPa). The boundary conditions used to fix the model included the development of a solid

model of the top loading jig and using frictionless sliding contact between the jig and femoral head only, allowing vertical displacement to model the movement. Then, the distal femur was rigidly fixed to a distance of 25 mm above the distal end. A vertical load of 1.5 kN was applied to the top surface of the loading jig. The composite model was found to be 2.3 times stiffer in torsion and 1.7 times stiffer in axial compression that its cadaver counterpart which could be due in part to the fact that the quality of bone stock obtained was representative of elderly bone donors. In addition, the authors also tested whether an adjustment of Young's modulus alone in the FE model would result in rigidity values within the measured natural femur range. Results showed that a Young's modulus of 4.5 GPa in the FE model predicted rigidity values within one standard deviation of those found in the cadaver bones, regardless of quality, thereby allowing a FE model to be developed to fit lesser bone quality.

A sampling of studies that successfully used composite bone as an experimental model include those by Iesaka et al. (2005), Chen et al. (2008) and Zdero et al. (2008). In the first two cases, the study included both a mechanical component using the composite bone and a computational component using FEA. The latter study used composite bones exclusively.

Iesaka et al. (2005) used the composite models and FEA to study the effects of gap size, stem stability, and cortical thickness between two ipsilateral intramedullary stems. The choice to use composite bone minimized the variability related to anatomical geometry and heterogeneous material properties. In the FEA model, the bone was further reduced to a hollow cylinder with cantilever

loading and modeled as an isotropic, homogeneous material. The initiatives were to determine if the stress on the femur increases when a metal stem is inserted into a bare femur and whether the stress increases if another metal stem is inserted in addition to one already existing. From the FEA results it was noted that the tensile stress varied inversely with the cortical thickness. Stresses approximately doubled with every 2 mm reduction in thickness.

An investigation by Chen et al. (2008) used composite bones in conjunction with FEA to determine the stiffness of distal femoral fixation with retrograde intramedullary nails under various screw-locking patterns. The composite bones were chosen due to their closeness in mechanical properties with natural bone. The femurs were potted proximally in polyurethane resin and set with two screws distally fixing the medial and lateral condyles and a plate fixing the posterior condylar surface. An axial load of 1,000 N was applied at 0.05 mm/s to the treatment groups (one-transverse osteotomy, one-oblique osteotomy). The FE model was meshed with tetrahedral elements and 2 mm thick shell elements distally to more closely represent the region. Simplifications to the model included bonding elements between the reamed femur and nail surface as well as modeling fixation screws as cylinders bonded to the model. Again, isotropic, linearly elastic properties were defined and in this case the properties provided by the manufacturer were adopted. The differences between the experimental and FEA for the intact femurs were below 5% and for the treated femurs under 10%. Deviations were attributed to mismatches in the

geometry, nail-screw-bone interface bonding choices, and boundary conditions provided by the mounting fixtures not as accurately represented in the FE model.

Zdero et al. (2008) evaluated different constructs of a periprosthetic femoral shaft fracture fixation following total hip arthroplasty using twenty third generation composite femurs. In this case, the femurs were chosen to reduce variability and previous work showed good agreement to natural bone in axial and torsional stiffness. Four different constructs were prepared and tested in axial compression, torsion, and bending. The femoral condyles were removed; the bone was aligned in 25° adduction and potted in anchoring cement. The femoral head was inserted into a cup allowing rotation while a 100 N preload and 1,000 N axial load was applied at 8 mm/min. Axial load-to-failure tests were also performed with the same loading protocol with the load applied until either the first abrupt change in load occurred or when a vertical deflection of 10 mm was achieved, noting a clinically practical limit. The important and relevant message from their study was that though the composite femora exhibit similar screw pull-out, no current study shows conclusively that the failure mechanism between the composite model and natural bone is equivalent. Moreover, the composite analogue simulates healthy bone stock, not those afflicted with osteoporosis, which are most likely to require such fixation constructs.

A recent comprehensive review of the application of composite bones in biomechanical studies was performed by Hausmann (2006). The compilation included a wide range of biomedical investigations representing primarily orthopaedic surgical techniques. All agreed that the use of the composite

analogue requires one to understand that the viscoelastic properties of real bone do not carry over into the composite substitute and as such the results of any study cannot be directly transferred to *in vivo* conditions. Additionally, the effect of soft tissue and remodeling are neglected. However, an indication for use of the composite models in testing scenarios wherein the medium is secondary, for example comparison tests between different surgical techniques or implants in compression bending or torsion, is quite favorable. The author concluded that an ideal study would consider a two-phase approach wherein the composite bone is utilized to develop the first phase and generate statistically relevant data, and then a phase two to compare and generate more clinically relevant data using cadavers.

As illustrated above, the use of composite bones as an experimental analogue allows researchers to develop collections of data that can serve as a baseline for which to build comparison studies of interest, such as changes in implant parameters or surgical techniques. Data from both the composite model and cadaveric model can then be used to generate and validate a finite element model.

1.6 Femoral Finite Element Analysis

A validated, computational analogue to the femur can supply researchers with unlimited opportunities to investigate the fundamental biomechanics of the femur and serve as a medium for testing surgical techniques and implant design. Further, it allows for investigations wherein the quality of bone becomes a critical

component to the function of the aforementioned investigations. A selection of FE analyses are presented here to give a flavor of what has been investigated recently, to discuss methods of preparing the proximal femoral model, and to illustrate some applications of the FE model.

The Standardized Femur model, a CT-developed version of a composite femur (Pacific Research Laboratories, Inc.) created by Rizzoli Orthopaedic Institute served as the model used by Greer et al. (1999) to investigate the appropriateness of using this model in the proximal femur. The time required to model the femur through CT is incredibly time intensive, so the availability of such a model in the public domain would lend itself to a wide array of comparative studies. The initial graphics exchange specification (IGES) data was downloaded from the internet and imported into Pro/Engineer with a truncation of the model to include only the proximal 150 mm. The model was meshed with 2nd order tetrahedral elements with refinements in the medial neck. Three analyses were performed on the model including: model validation, stress distribution in the femoral neck cancellous tissue, and consider geometrical anomalies in the model. The results showed that the FE model can reasonably predict the deformation of the femur. However, the computed von Mises stresses in the cancellous region were an order of magnitude lower than those reported in literature (Lotz, 1988). This was attributed to the thicker wall of the composite's cortical proximal region compared to natural bone. A comparison was made with the Standard Femur geometry to the cryosections available at the National Library of Medicine's Visible Human Project finding that the thickness of the

composite cortical bone ranged from 2.7-4.9 mm while the natural bone ranged from 1-1.5 mm. As such, its use in predicting proximal femoral fractures can lead to inaccuracies.

The objective behind the work performed by Ramos and Simoes (2006) was to compare the tetrahedral and hexahedral elements utilized in model meshing and determine which was most suited for proximal femur geometries. A simplified geometric model of the femur was created (curved cylinder) wherein an analytical evaluation of the displacement and stress-strain curve could be calculated and compared with the FE results. Loading configurations represented those incurred from abductors and hip reaction forces while the distal end of the femur was fully constrained. Four different types of elements were investigated: 4-node linear tetrahedral, 10-node quadratic tetrahedral, 8-node linear hexahedral and 20-node quadratic hexahedral elements. In addition, the Standardized Femur model was used and its loading scenario also incorporated the hip contact force, and forces from the glutei, tensor fasciae latae, and vastus lateralis. To compare the results, a third generation composite femur was prepared with 20 uniaxial strain gages on the lateral, medial, anterior and posterior surfaces, oriented in 11° adduction, and loaded in a compressive cycle of 0 to 567 N, ten times. With the simplified femoral model and its respective FEA model, the first order tetrahedral and hexahedral elements produced results more closely to the theoretical values than the second order elements. In the Standardized Femur model the comparison between numerical and experimental strains showed excellent correlation, especially on the medial and lateral aspects

of the femur. In observing the lateral surface strains of the diaphysis, a trend of increasing strain occurred through midshaft then decreased travelling toward the condyles. Overall, the linear tetrahedral elements values proved closest to the theoretical values calculated from the simplified geometric model; however, the hexahedral quadratic elements were slightly more stable and less resistant to influence by mesh refinement.

Mahaisavariya et al. (2006) was one of the few studies to use FEA in order to evaluate the effects of insertion of fixation hardware and removal of hardware using the trochanteric gamma nail (TGN). The aim of their study was to evaluate the stress and strain distribution profiles of the proximal femur. The CAD model of the femur was generated from the average geometries of CT scans taken from 108 Thai cadaveric femora. The TGN was placed into the model following respective surgical technique for the TGN fixation. Four-noded tetrahedral elements were used to mesh both the femur and TGN. Material properties were distributed to reflect varying densities of both the cortical and cancellous bones. The loading conditions consisted of the joint reaction forces and loading related to various muscle groups. The results showed that the TGN produced high stresses in the surrounding bone caused by the main function of the implant which was to stabilize the region. The stresses primarily affected the cancellous bone and experienced a greater change in stress when the TFN was removed compared to the stresses observed in cortical bone's screw-hole defect. The strain in the cancellous bone was higher inside the neck as this material tends to adapt and resist bending and torsional forces under load. The higher

strain following ROH was on the cortical surface of the neck where the layer becomes the primary structure to resist bending moment and torque. With the retained hardware, higher stresses were transferred through the nail and into the surrounding bone. Because the strain in the neck was found to be higher after ROH, there exists a greater risk of femoral neck fracture after TGN removal. The study further shows that the strains are higher in the neck than in the entry point of the lag screw meaning the failure would be more likely to occur in the neck than at the subtrochanteric level.

Shi et al. (2008) used FEA to evaluate the effect of a calcar defect and restoration of that defect with various fillers. The study focused on the insertion of porous hydroxyapatite (PHAC), bone cement, or autogenic bone into a cylindrical defect created opposite the calcar. The materials were assumed linear elastic. The distal end was fixed and three groups of joint reaction forces were applied on the head to simulate the load of a 70 kg man. Aside from the results of most appropriate filler according to diameter of defect, a trend in general showed that increasing defect diameters led to increased stresses in the region.

Finally, Bessho et al. (2009) performed one of the more expansive studies on the prediction of stress and strain in the proximal femur by using a CT-based FEA method. Eleven fresh-frozen femora were used for the study. To most effectively match the loading sites, boundary conditions, and location of strain gages in the FE meshed model, a 2D image of each specimen was developed through the use of attaching eleven circular fiducials to the head, trochanter, and diaphysis. The femurs were oriented at 20° adduction, the head was fit into a

dental resin cap to a depth of 8 mm, and the distal diaphysis was embedded in wood metal (analogous to Cerrobend). Eight total stacked rosette strain gages were attached to the diaphysis, trochanter region, and neck. A pre-load of 200 N was applied and femurs were compressed at a rate of 0.5 mm/min and sampled at 2 Hz, while the strain gages were sampled continuously at 0.5 Hz. Tetrahedral elements were used for the bulk of the model reserving triangular shell elements for the outer surface of the cortex to more accurately represent the cortical shell. To remedy the underestimation of material properties related to the small CT values caused by the partial volume effect, a thickness of 0.4 mm was applied to the element. Model convergence was investigated with 2 mm, 3 mm, and 4 mm elements, keeping the aspect ratios consistent. Strain energy was calculated at 2,000 N under the same loading and boundary conditions. While the 2 mm model was the most accurate, the 3 mm was sufficient and took about one-third of the computing time. Material heterogeneity was addressed through the calculation and application of Hounsfield units and ash density values as done in CT-based FEA models. Nonlinear FEA was performed; the elements were assumed to be bi-linear elastoplastic with the post-yield modulus set as 5% of Young's modulus. While the model did assume isotropic material properties, the criteria for failure differed between compression and tension noting that the ultimate tensile strength was assumed to be 0.8 times the compressive yield stress. The failure and yield of an element was evaluated by a six step process that began with whether the Drucker-Prager equivalent stress had exceeded the elemental yield stress. Results showed that the CT-based FEA method not only is an effective

tool in determining stress/strain distributions in the bone but also can serve as a method for determining regions of high fracture risk. The author's analyses combined many details set aside in other similar studies, leading to a more robust approach in determining stress and strain distributions in the proximal femur.

1.7 Scope of Work

In consideration of the review of literature encompassing femoral biomechanics, proximal fracture fixations, removal of hardware, composite bone use, and finite element analysis, several specific aims were generated in order to develop an experimental protocol and computer model that would both simply and accurately represent a case for investigating the response of bone following ROH.

- *Create Experimental Design* – Simplify femoral loading to a scenario reasonably reproducible in an axial testing machine by eliminating soft tissue affects and consider only compressive loading
- *Minimize Variability* – Reduce variability encountered with animal and cadaver models and increase repeatability by incorporating composite bones that model a healthy human femur
- *Develop Preliminary Finite Element Model* – Develop solid models and preliminary computer simulations that mimic the experimental conditions and minimize computing time

- *Validate Computational Model* – Utilize results from literature, strain gages, and optical elastography to validate the preliminary model
- *Provide Insight to Future Work* - Compile results and discuss where trends may need further investigation, suggest steps for further FE model refinement, and application of the collected data

1.7.1 Create Experimental Design

This study focused on the removal of hardware and loss of strength incurred by the bone due to the stress risers created by the residual holes. Simplification of the statically indeterminate hip was the first critical step in designing the experimental model. As a preliminary study, a simple model focusing only on the bone itself was the most practical approach. References in literature using such a model were indicated previously in Sections 1.5 and 1.6 and met with successful results.

The orientation of the femur during testing needed to mimic, as close as possible, the anatomical conditions *in vivo*. Decisions were made to capture the function of the proximal and distal articulating surfaces of the femur. While in the testing machine, the femoral head was encased in a grip that allowed a ball-and-socket sense of mobility while under load and the condyles were cast to create an analogous articulating surface that occurs at the knee. The relative angle of the femur was set such that it would represent the worst loading scenario statically. Previous research has shown that the one-legged stance represents

the largest loads on the femur leading to a 10-12° adduction of the bone (Duda et al., 1997).

Augmentation of the bone was representative of the common proximal fracture fixation devices. Implants were obtained that corresponded to the primary means of compressing proximal fractures. Femurs were augmented with cannulated screws, DHS and IHS implants typically used in clinical practice with insertion procedures according to standard orthopaedic guidelines. In addition, plans were developed to evaluate the effect of cement augmentation on residual holes.

1.7.2 Minimize Variability

As discussed in previous sections, a high degree of variability exists both inter- and intra-specimen in cadaver bones. Geometry, internal structure, age, porosity, density, and pathology all contribute to inconsistencies when using real bone tissue. A review of composite models used in literature indicated that the range of properties, though considered isotropic compared to bone's anisotropic behavior, fall enough within the range of healthy human cadaver data that the model is well accepted for use in laboratory testing. The composite bone provides a uniform geometry and density which assists in repeatability of the experiment.

1.7.3 Develop Preliminary Finite Element Model

An advantage to using the composite model is the ability to obtain the computer aided drawings (CAD) of the manufactured part. The highly convoluted geometry of the femur was generated through a computer tomography (CT) scan of a 6 ft tall, 200 lb male cadaver femur. The model was imported into SolidWorks as three parts (simulated cortical, simulated proximal cancellous, simulated distal cancellous) and modified according to the treatment groups. One adjustment that had to be applied to all treatments groups, including the controls, was the addition of a cross pin hole that occurs during the manufacturing process and runs from the lateral surface through the midline of the neck to the medial center of the head.

CAD models were also obtained from the manufacturer of the fixation hardware in order to best represent the intricacies of the implant geometry. Each model was inserted as a part into the CAD femur at the proper surgical location, and then the geometry was subtracted from the femur leaving the appropriate residual holes.

Boundary conditions, loads and model settings were developed to best represent the experimental model and to lessen computing time within the finite element package.

1.7.4 Validate Computer Model

Tools were chosen to validate the computer model beyond the use of literature and experimental results. Strain gages were applied to the lateral

surface of the femur which experiences high tensile stresses during compressive loading. Strains that occurred locally (under the area of the gage) were compared to the same geometric regions within the finite element model (FEM). The gages were general use, linear strain gages and placed longitudinally on the midline of the lateral surface. Nodes in the FEM for the same region were located and compared to the value given by the respective strain gage.

Strain gage rectangular, planar rosettes were also chosen for use on one femur of each treatment group. These are indicated when the principle axes are not known, which is the case with the most proximal, lateral curved surface of the femur. Data from these gages, once corrected for transverse loading, can be used to calculate the principle strain axes and orientations.

Optical elastography was selected as means of non-invasive local strain detection. With this technology, strain variations could be detected through the use of high definition videography at a capture rate of 30 fps. The resulting elastogram provided information to the pixel level on the material's heterogeneity as a result of the applied treatments. Elastogram data was correlated with both experimental and FEA results.

1.7.5 Provide Insight to Future Work

Upon compilation of the experimental and computational results, trends that needed further investigation or abnormalities that needed addressed through changes in protocol were reported. Furthermore, suggestions on avenues to

pursue for the further refinement of the preliminary FEM were discussed. Finally, applications of the collected data were noted as well as future clinical relevance.

CHAPTER 2

EXPERIMENTAL TECHNIQUE

2.1 Composite Bone

The primary goal of the experimental testing was to validate the computational models of the femurs, their respective augmentation and ROH procedures under investigation. To accomplish this, twenty-one composite femurs (Sawbones, fourth generation, large left femur, model 3406, Pacific Research Laboratories, Inc., Vashon, WA) were chosen as models for the healthy, human femur, Figure 2.1. The choice to use composite models was based primarily on minimizing both the inter-specimen and intra-specimen variability that is normally found in human cadaver femurs. The composite bones provide a uniform geometry, constant density, lower attainment costs, ease of storage and do not require the additional approvals generally necessary by local internal review boards when using cadaver bones.

Figure 2.1. Sawbones fourth generation, large left, composite femur

Composite femurs have been used previously in literature and accepted as a substitute for cadavers as noted in Sections 1.6 and 1.7. This particular composite femur was modeled after a 6 ft tall, 200 lb male, information provided by Pacific Research Laboratories, Inc. (personal communication, 2011). The composite bones have material properties analogous to healthy human bone and thus are accepted substitutes for biomechanical testing. However, it is important to note that the composite bones do not exactly replicate natural bone biomechanics, especially in regard to viscoelastic properties and internal structure (Hausmann, 2006). As such, it is more appropriate to set test protocol and review results as a comparison of pre and post-treatment than as an absolute reflection of how bone would behave.

To represent the hard cortical outer layer of bone, the composite's outer material is a fiber-filled epoxy. Encased in the epoxy is the simulated cancellous bone composed of rigid polyurethane foam. Material properties of the composite bone and of human bone are shown in Table 2.1 (Simon, 1994; Pacific Research Laboratories, Inc., 2011).

Table 2.1. Material properties of the composite femur and human femur

Material	Density (g/cm^3)	Poisson's Ratio	Compressive modulus (N/mm^2)	Compressive strength (N/mm^2)
Simulated cortical fiber-filled epoxy	1.64	0.26	16,700	157
Human cortical bone	1.80-1.90	Up to 0.6	17,000	130
Simulated cancellous-polyurethane foam	0.27	0.30	155	6.0
Human cancellous bone	0.1-1	0.06-0.95	100-400	0.8-11

2.2 Test Equipment

Equipment used in the mechanical testing included: Instron 5967 materials testing machine with 30 kN load cell and Bluehill 3 acquisition software (Instron, Canton, Massachusetts); custom manufactured grips; CEA-06-125UW-350 linear strain gages and CEA-06-125UW-350 rectangular planar strain gage rosettes (Vishay, Raleigh, NC); NI cDAQ-9172 Legacy NI CompactDAQ Chassis, NI USB-9219 4-Channel Universal Analog Input Machine, NI LabView 2010 (National Instruments, Austin, TX), and Sony HDR-SR1 high-definition camcorder.

2.2.1 Compression Testing Machine

The Instron, Figure 2.2(a), allows for compression, tension, shear, and three-point bending testing of samples in a variety of orientations. For the purpose of this study, the Instron was used for uniaxial compression testing.

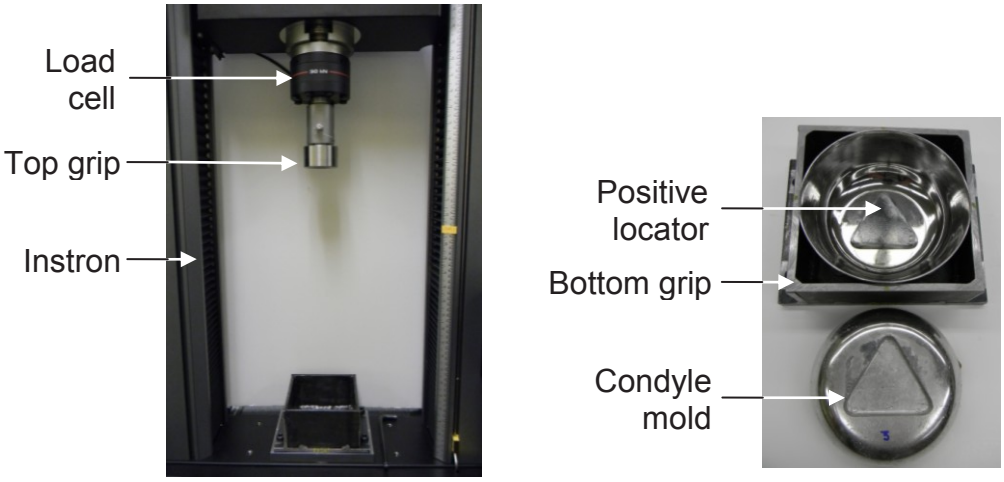

Figure 2.2. Axial test set up. (a) Instron 5967, (b) Bottom grip showing positive locator and casting

The axial testing machine was electrically connected to a Dell Precision T3500 computer containing Bluehill 3 software that both controlled the machine and collected data from the test. The load cell, attached mechanically to the Instron, Figure 2.2(a), and electronically to a personal computer was capable of accuracy equal to or better than 0.025% of the cell rated output or 0.25% of the indicated load, whichever was greater. The femoral head was positioned inside a polished steel machined cup simulating the acetabulum and was labeled as the top grip. The bottom grip was a 5x5 in steel box with a 5.5 in stainless steel bowl inset, Figure 2.2(b). The bowl was fashioned with a raised triangle to help positively locate the molded femoral condyle. The bottom grip was attached firmly to the base of the machine. The software required the input of a representative geometry of the sample in order to perform calculations chosen for the test. The shape of the femoral shaft was approximated as a cylinder and mediolateral (ML) and anteroposterior (AP) dimensions were taken at mid-shaft, Figure 2.3. Those dimensions were averaged to give the necessary diameter to perform area calculations within the software. The length of the full femur was used for the length of the cylinder.

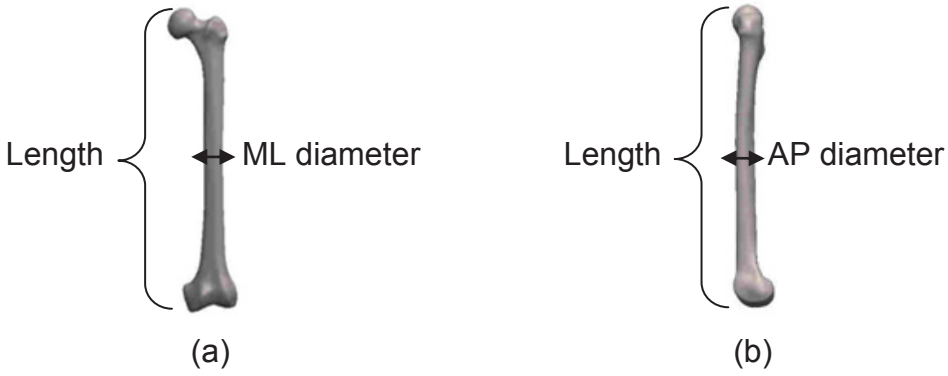

Figure 2.3. Femur measurements. (a) ML dimension, (b) AP dimension

The top grip moved vertically, applying a compressive load to the head of the femur. A pre-load of 10 N allowed the femoral head to seat within the top grip, and then the test progressed at a rate of 8 mm/min. The test was scheduled to stop with either the first abrupt change in load or a 10 mm deflection, whichever occurred first. As contact was made between the grip and the femur, the computer displayed load (N) and vertical compressive displacement (mm) in real time. Data collection was set at 16.67 ms (60 Hz). Compressive stress, compressive strain, and compressive extension at both the maximum load and at break were calculated by the software.

2.2.2 Strain Gage Data Acquisition

The CEA-06-125UW-350 linear strain gages and CEA-06-125UW-350 rectangular planar strain gage rosettes were adhered to the composite femur and connected through cables to the NI USB-9219 4-Channel Universal Analog Input Machine which was placed in the NI cDAQ-9172 Legacy NI CompactDAQ Chassis, Figure 2.4(a). In order to monitor the stain gage data continuously across multiple channels, a custom program was created in NI LabView 2010 and run on a Dell Inspirion 6000 laptop computer, Figure 2.4(b).

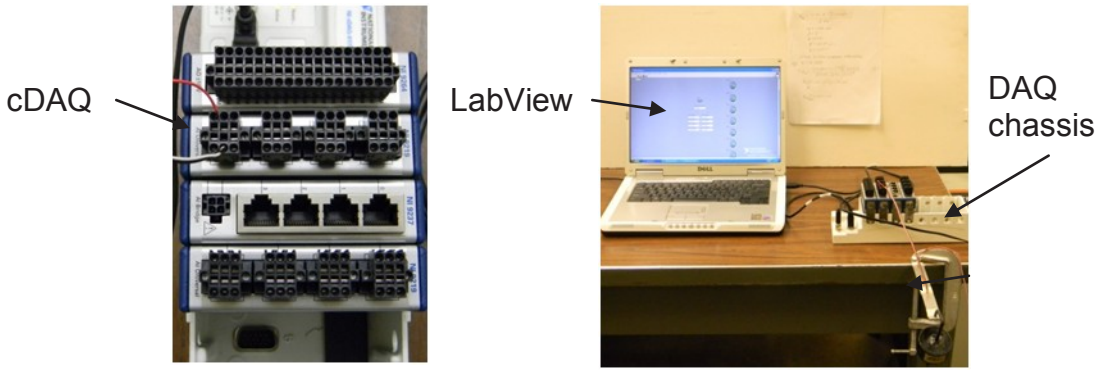

Figure 2.4. Strain gage DAQ hardware. (a) DAQ, (b) Computer, DAQ, chassis

The front panel diagram, Figure 2.5, for the data acquisition was composed of eight on/off buttons representing the maximum number of strain gages that were applied to each femur in this study. Since some of the femurs had a strain gage rosette in addition to the linear gages, provisions were made to allow for either a combination of five or eight channels to be continuously monitored. A start button was added to begin the data collection as well as boxes to display the elapsed time and strain readings of each channel.

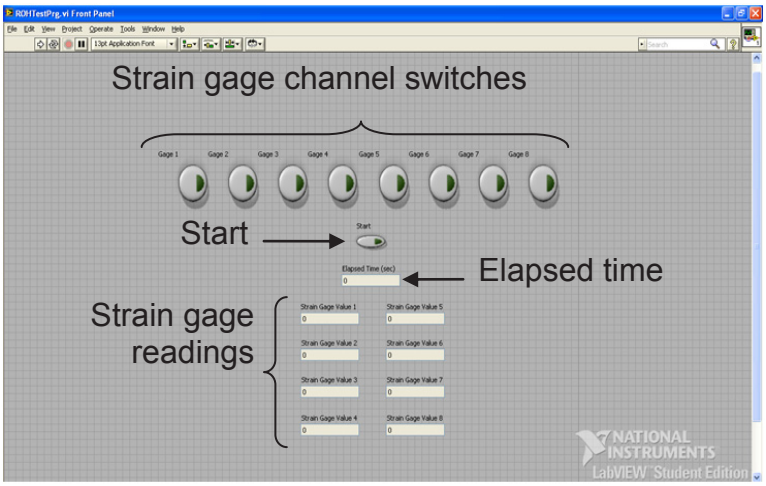

Figure 2.5. Strain gage acquisition front panel diagram

The block diagram, Figure 2.6, consisted of an outermost *While* loop including a *Write to Measurement File* control that directed the data to an appropriate LVM file, which could be opened inside an Excel spreadsheet. Inside that loop was the main *While* loop that encompassed the bulk of the program. Each strain gage was provided its own channel wherein through the program's *DAQ Assistant*, product specifications for each strain gage were input and data collection rates were assigned. More specifically, the *DAQ Assistant* allowed for selection of the required Wheatstone bridge configuration for the test, the gage factor (sensitivity of the gage relating change in electrical resistance to change in strain), gage resistance (nominal value of each of the resistance arms for a full Wheatstone bridge), lead resistance (resistance of lead wire), vex source (specified source of excitation), vex value (amount of excitation used), acquisition mode (type of collection), samples to read, and rate.

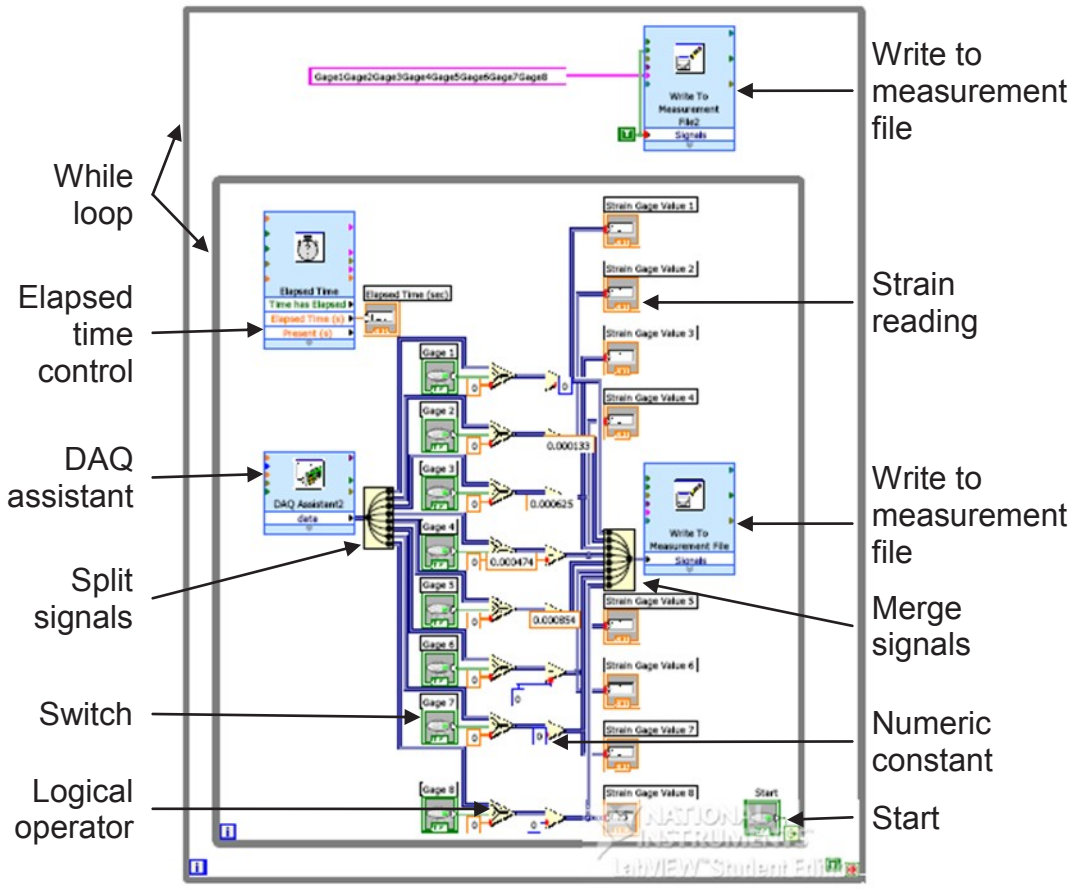

Figure 2.6. Strain gage acquisition block diagram.

From the *DAQ Assistant*, the signal was split into the eight channels needed for testing. Each channel was assigned a *Sensor* that when attached to the *Logical Operator,* functioned as an on/off switch. When powered on, the program was led to read a value from the *Numerical Constant,* which was added in order to cancel out any resistances in the wire or residual strain in the unloaded condition. To determine the numerical constant, a measurement was taken without an applied load. When the test was run under load, the numerical constant was subtracted from the strain recorded with the load, yielding the

actual strain value. Finally, each channel's reading was filtered into *Merge Signals* and placed into a *Write to Measurement File*.

For the development and subsequent validation of the computer program, a simple beam model was created to test the accuracy of the strain recordings and comparisons were made to both theoretical and experimental values. The beam used was an aluminum bar measuring 8.25 in long, 0.75 in wide and 0.123 in thick, Figures 2.7(a) and 2.7(b). A CEA-06-125UW-120 linear strain gage was applied according to the manufacturer's recommendations for beam and gage preparation (Vishay Measurements Group, 1992). The gage resistance was 120 Ω and the gage factor, k, was 2.085 as provided by the manufacturer. The gage was placed 5.25 in from the left edge of the bar, the bar was fixed at the edge of a table via a clamp, and the weight, generating a 1.089 lbf downward load was applied at 0.25 in from the left end.

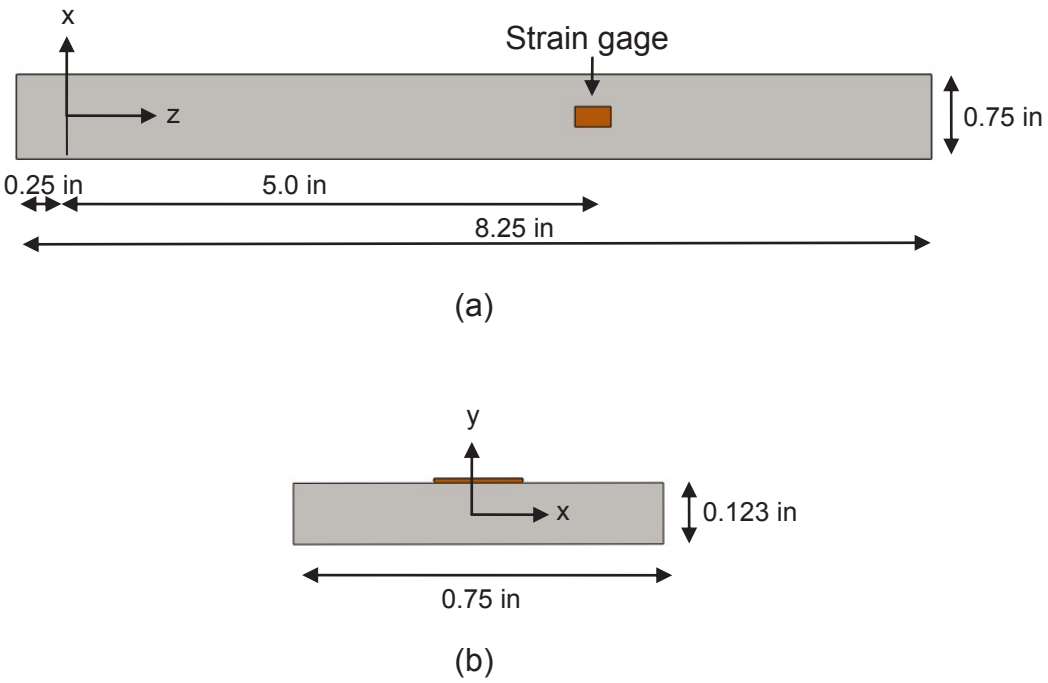

Figure 2.7. Aluminum bar geometry. (a) Top view, (b) End view

Lead wires were soldered to the strain gage and then attached to a P-3500 Strain Indicator (Vishay, Raleigh, NC) to experimentally determine the strain in the bar, Figures 2.8(a) and 2.8(b). The recorded experimental value was 293 με.

(a)

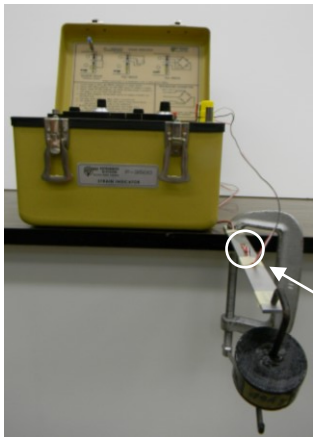

(b)

Figure 2.8. Strain validation equipment. (a) Strain indicator, (b) Experimental set up

The theoretical analysis of the bar followed classic stress analysis of a cantilever beam. The elastic modulus of the aluminum bar, *E*, was assumed to equal $10x10^6$ psi. Beginning with the fundamental isotropic, one-dimensional relationship for stress and strain, as well as the equation for stress of a member in pure bending, the equation was solved for strain.

$$\sigma = E\varepsilon_z \tag{2.1}$$

$$\sigma_{bending} = \frac{M_x y}{I_{xx}} \tag{2.2}$$

$$\varepsilon_z = \frac{M_x y}{E I_{xx}} \tag{2.3}$$

where σ is the stress (psi) and ε_z is the strain (in/in) both along the bar length. M_x is the moment (lbf-in) about the x-axis caused by the applied weight, and y is the distance from the beam's neutral axis to the point of interest. Finally, I_{xx} is the area moment of inertia. The value for the moment, M_x, was determined from the weight, w, applied times the length, l, from the weight to the center of the strain gage. The value for y was determined from half the thickness of the bar and added to the gage thickness, t. Finally, the moment of inertia, I_{xx}, for a rectangular cross-section was represented by $bh^3/3$, where b is the width of the bar and h is the height of the bar. Thus the equation for strain becomes the following:

$$\varepsilon_z = \frac{(wl)(\frac{h}{2} + t)}{E(\frac{bh^3}{12})} \tag{2.4}$$

The calculated strain was determined to be 295 με and correlated well with the experimental strain of 293 με. To then check the system to be used with the femur testing, the aluminum bar was connected to the 4-Channel Universal Analog Input Machine for determination of the strain through the LabView-created data acquisition program. Inputs to the program included the measured value in the unloaded condition as the numerical constant, a gage factor of 2.085, a gage resistance of 120 Ω, a lead resistance of zero, an internal vex source of 2.5, and a continuous sample reading of 10 samples at a rate of 60 Hz.

The measured value from the computer program was 297 με which correlated well with both the theoretical and experimental values.

2.2.3 Optical Elastography

Each femoral compression test was captured with a Sony high-definition camcorder in order to provide information about the local responses to stress and strain along the composite bone's surface. This method of non-invasive testing produces elastograms that illustrate the strain variations on a pixel level. The respective optical flow algorithm that estimates the pixel's motion is achieved by solving a brightness conservation equation (Marie et al., 2010):

$$\frac{\partial I}{\partial x}\frac{dx}{dt} + \frac{\partial I}{\partial y}\frac{dy}{dt} + \frac{\partial I}{\partial t} = 0 \tag{2.5}$$

where the image brightness function, *I(x, y, t)*, is represented by rows and columns of *x* and *y* respectively and the frame interval (time) represented as *t*. The resulting motion vector of a point is then given by:

$$u = (u, v)^T, u = \frac{dx}{dt}, v = \frac{dy}{dt} \tag{2.6}$$

A unique solution does not exist, however, in the first equation due to mathematically ambiguity caused by the aperture problem. Therefore, constraints in the form of a regulation term need to be imposed leading to:

$$obj(u, v) = (I_x u + I_y v + I_t)^2 + \lambda(u_x^2 + u_y^2 + v_x^2 + v_y^2) \tag{2.7}$$

where I_x, I_y, u_x, u_y, v_x, and v_y denote the partial derivatives of the corresponding variables and λ is the Lagrange multiplier (or regulation coefficient). The resulting solution for optical flow *(u, v)*, which is obtained by minimizing the above equation, is a compromise between the smoothness constraint and the observed motion. Detailed information regarding the derivatives of the optical elastograms can be found in Marie et al. (2010).

2.3 Test Protocol

The experimental procedure developed was based on literature review, access to resources, and consultation with both an orthopaedic surgeon and engineering faculty. A total of thirty composite femurs were obtained with twenty-one suitable for the current study. Three femurs were returned and replaced due to failure related to voids within the material or surface abnormalities, and six were placed on indefinite hold due to difficulties in obtaining additional supplies. Femurs were cataloged, cast, augmented, sanded, outfitted with strain gages, tested, videoed, and imaged as part of the experimental protocol.

2.3.1 Femoral Measurements and Cataloging

Each femur was measured, cataloged, and placed in a treatment group, Table 2.2. Midlines were marked on the anterior surface of each femur as well as mid-diaphysis, 50 mm below mid-diaphysis (location of bottom clamp during casting), and 50 mm above mid-diaphysis (location of top clamp during casting). Due to the oval shape of the diaphysis, measurements were recorded in the

anteroposterior (AP) and mediolateral (ML) directions separately. The total length was measured from top of the femoral head to the most distal point of the condyles, Figures 2.3(a) and (b).

Table 2.2. Composite femur augmentation and measurements

Sample	Treatment group	Length (mm)	Mid-shaft AP (mm)	Mid-shaft ML (mm)
1	Control	485	30.9	33.7
2	Control	491	30.6	34.3
3	Control	492	30.7	34.2
4	Cannulated screw-holes	491	30.9	33.5
5	Cannulated screw-holes	491	30.8	33.7
6	Cannulated screw-holes	490	31.0	33.7
7	Cannulated screw-cement	488	30.8	33.7
8	Cannulated screw-cement	488	31.3	32.7
9	Cannulated screw-cement	487	31.2	32.7
10	DHS-holes	490	30.8	33.9
11	DHS-holes	488	31.5	32.7
12	DHS-holes	489	31.2	32.7
13	DHS-cement	485	31.4	32.8
14	DHS-cement	495	31.1	32.6
15	DHS-cement	491	30.7	31.0
16	IHS-holes	493	30.9	33.5
17	IHS-holes	491	31.1	34.1
18	IHS-holes	490	31.0	33.6
22	IHS partial-holes	492	31.1	34.1
23	IHS partial-holes	490	31.0	32.4
24	IHS partial-holes	490	31.1	32.5
	Mean (Std. Dev.)	*490 ± 2.1*	*31 ± 0.24*	*33 ± 0.81*

The initial test matrix included controls (no augmentation), fully or partially removed hardware (cannulated screws, DHS, IHS, IHS-partial removal), and cement-filled residual holes (cannulated screws, DHS, IHS, IHS-partial removal) composite femurs. Due to some unforeseen complications with the obtainment of cement part-way through the preparation, only the cannulated screws and DHS femurs were fully prepared for testing. As such, comparisons were made primarily about the response of bone to the removal of hardware without cement fill.

2.3.2 Femoral Condyle Molding

In order to recreate the articulating surface at the knee, molds were cast of each femoral condyle. Though a time consuming process to model each condyle, it served as a better representation of the natural occurrence at the knee as opposed to fixing the entire distal portion of the femur in cement. While it was initially assumed that one mold would work for all of the composite femurs, it was determined that the trim lines at the bottom of the femur varied too much from sample to sample to allow for a firm seating in one standard mold. Therefore, molds of each condyle were cast and numbered according to its femoral parent.

This particular model of the composite femur is manufactured with an medullary canal which has a hole at the bottom of the bone. In order to effectively mold the condylar surface, the hole was filled with modeling clay prior to the casting process, Figure 2.9. The condylar surface was also lightly oiled with general purpose oil (3-In-One) as was the bottom grip's inner bowl to allow for easy unmolding.

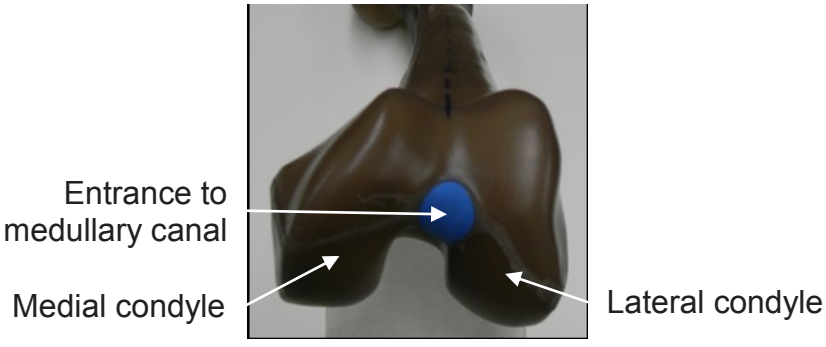

Figure 2.9. Composite femur, end view

To model the one-legged stance, a femoral angle of 10° adduction angle from the vertical, a template was created to produce a consistent method of securing the femur and maintaining the required angle during casting, Figure 2.10(a). Once the femur was placed inside the clamps, the template was applied to the back of the bottom grip. The femur was aligned to the femoral image within the anchoring screws, noting a neutral alignment, Figure 2.10(b), and a 10° adduction from the vertical, Figure 2.10(c).

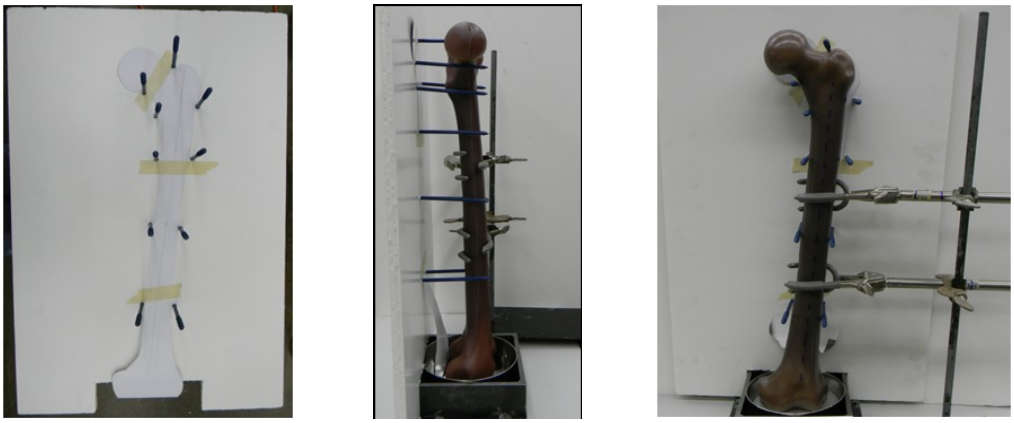

(a) (b) (c)

Figure 2.10. Femoral alignment. (a) Template, (b) Side view, (c) Front view

The chosen casting material was a low melting point, eutectic alloy (Cerrobend) that was melted in a stainless steel pan over a hot plate just under 200°F. The molten metal was poured into the front of the bottom grip's inner bowl in one smooth motion. Solidification was complete within fifteen minutes. To guarantee that the casting would not be damaged upon removal, the top of the mold was covered with several layers of taped cardboard prior to flipping the base over to remove the casting, Figure 2.11(a). The final casting was removed and allowed to cool for fifteen minutes on a wire rack, Figure 2.11(b).

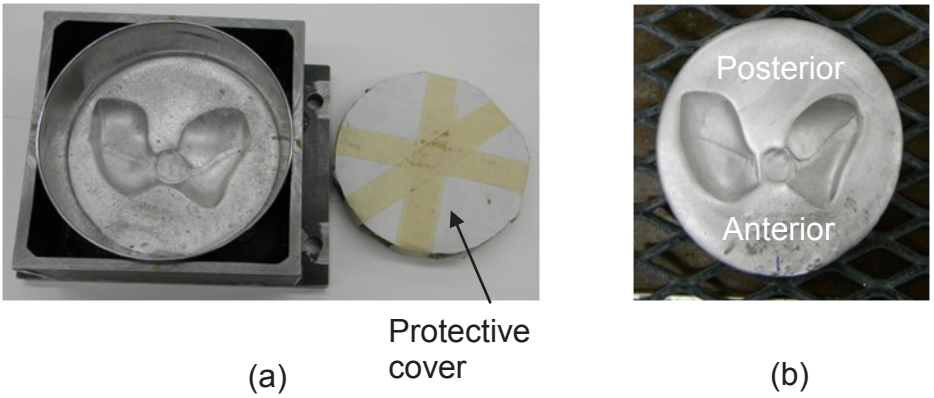

Figure 2.11. Condylar castings. (a) Bottom grip with casting, (b) Final casting

2.3.3 Femoral Augmentation

Femurs were augmented with cannulated screws, a dynamic hip screw system, or an intramedullary hip screw system. The 7.3 mm cannulated screws were composed of 316L stainless steel with a 16 mm thread and lengths of both 95 mm and 105 mm (Synthes, West Chester, PA). A parallel multiple wire guide was used to create an inverted triangle for the insertion of three cannulated screws, Figure 2.12(a). Using an Insight fluoroscope for guidance (Hologic, Bedford, MA), the first guide wire was inserted on the lateral cortex at the superior level of the lesser trochanter, just above the calcar in the AP view, Figure 2.12(b). From the lateral view, Figure 2.12(c), the wire was placed centrally in the femoral head. The wire was stopped at the subchondral level. The multiple wire guide was adjusted such that two superior wires were inserted parallel to the first in the AP view; and in the lateral view, one wire appeared anterior and one posterior to the initial guide wire. The outer cortex was opened with a 5.0 mm cannulated drill bit and screws were inserted with the two 95 mm

screws at the top of the inverted triangle and the 105 mm screw and the bottom of the triangle. All screws were inserted to the subchondral level and subsequently removed.

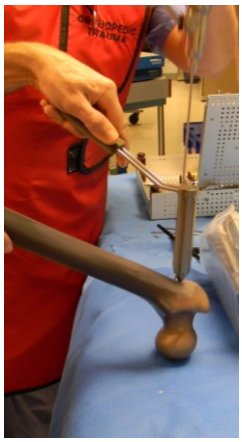

(a)

Front view

(b)

Lateral view

(c)

Figure 2.12. Cannulated screw augmentation. (a) Wire guide, (b) Screws, (c) Guide wires

The dynamic hip screw system (Synthes, West Chester, PA) consisted of three 316L steel components: a 12.7 mm threaded lag screw 85 mm long, two 4.5 mm self tapping cortex screws 44 mm long, and a 135° DHS plate. Under fluoroscopic guidance, a guide wire with a 125° guide was placed into the central area of the femoral head in the AP, Figure 2.13(a) and lateral views. The wire was inserted to the subchondral level. The depth was measured using a guide which was calibrated to guide the wire and measure from the external portion of the wire. The femur was stabilized and the region was reamed and tapped over the guide wire, Figure 2.13(b). The side plate was placed over the screw and centered over the lateral cortex. A 3.2 mm drill bit was used to make two bi-

cortical holes corresponding to the holes in the plate. Finally, the appropriate 4.5 mm cortex screws were inserted and all hardware was subsequently removed.

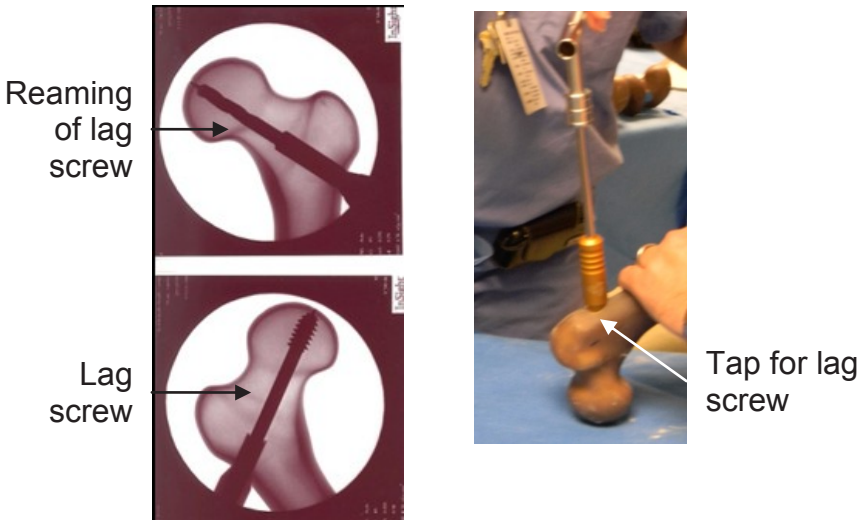

Figure 2.13. DHS augmentation. (a) Fluoroscopic images, (b) Tapping of lag screw

Norian SRS (Skeletal Repair System) cement was used to fill the residual holes from the ROH in the cannulated screws and DHS groups. The product, injectable calcium phosphate cement, sets at body temperature into carbonated apatite, which closely resembles the mineral phase of bone. The indicated use of the product is for bony voids which have been stabilized with standard AO orthopaedic techniques and implants. The chosen use of Norian in this study was to determine if the cement, used off-label as a stand-alone filler, would provide any significant increase in material properties that were lost due to ROH.

The preparation of Norian SRS was performed according to the manufacturer's instructions and transferred to the residual holes via syringe. Three holes were filled in the cannulated screws group and the lag screw and

two cortex screws were filled in the DHS group, Figures 2.14(a)-2.14(d). Curing of the cement occurred in 24 hours and mechanical testing followed a month later.

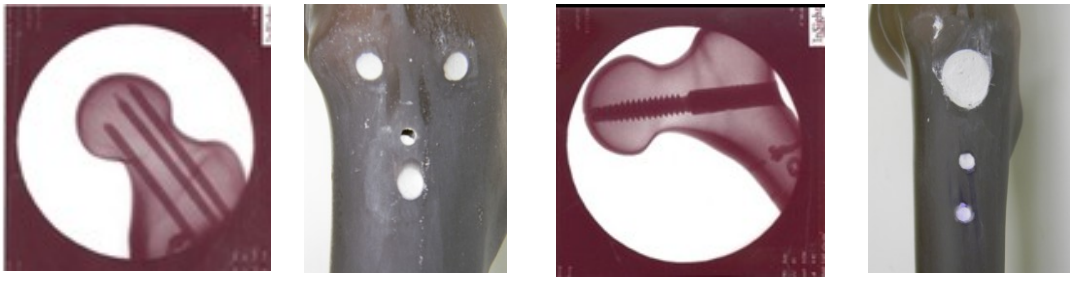

(a) (b) (c) (d)

Figure 2.14. Cement application. (a) Fluoroscopic view of filled cannulated screw holes, (b) Lateral view of filled cannulated screw holes, (c) Fluoroscopic view of filled DHS lag screw hole, (d) Lateral view of filled DHS holes

The intramedullary hip screw system or trochanter fixation nail (Synthes, West Chester, PA) also consisted of three parts: a 10 mm/130° cannulated titanium fixation nail 170 mm long, a 5.0 mm titanium alloy locking screw 44 mm long and a 11.0 mm titanium alloy helical blade 90 mm long. For insertion of the nail, a guide wire was placed just lateral to the tip of the greater trochanter in line with the long axis of the femur. The wire was inserted into the medullary cavity of the proximal femur to the lesser trochanter and its position verified by fluoroscopy. Next, a 17 mm cannulated tapered drill bit was inserted over the wire down to the level of the lesser trochanter. The guide wire and drill were removed and a long beaded guide wire was inserted into the medullary cavity and reamed in 0.5 mm increments up to 1.5 mm greater than the diameter of the intramedullary. The depth of the ream was stopped just past the length of the

nail. The nail was attached to the percutaneous handle and inserted into the canal, Figure 2.15(a). Orientation of the nail within the canal was adjusted by movement of the handle. The blade guide was attached to the handle completing the insertion jig and a guide wire was inserted and the region subsequently reamed for insertion of the helical blade. The set screw, which is built into the proximal end of the nail, was tightened to prevent rotation. The cortex screw was drilled with a 3.2 mm drill bit and inserted through the insertion jig. The cortex screw was placed obliquely through the lateral cortex from proximal lateral to distal medial, Figure 2.15(b).

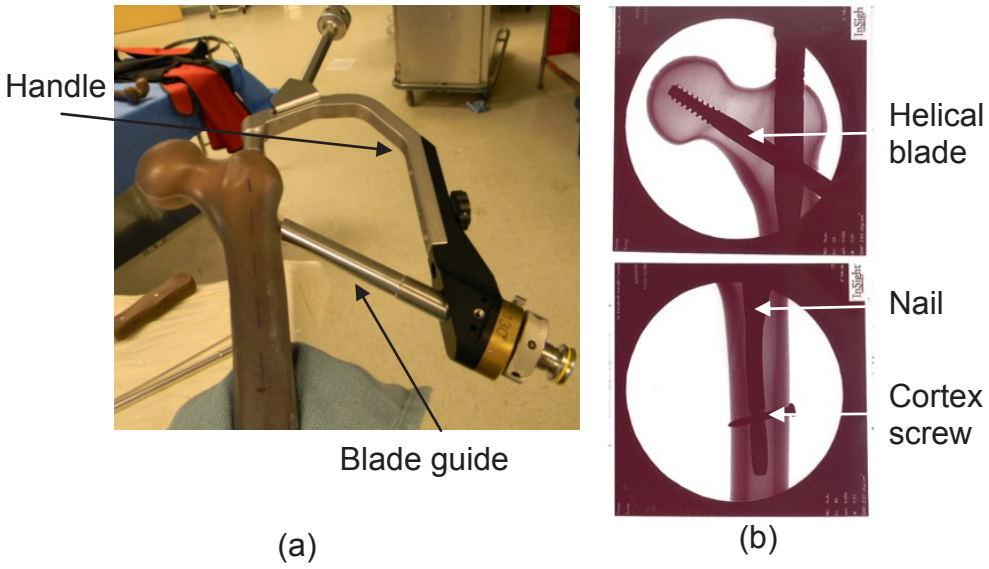

Figure 2.15. IHS augmentation. (a) Insertion jig, (b) Fluoroscopic images

2.3.4 Strain Gage Attachment

Linear strain gages were selected for the purpose of validating the finite element model. The average strain reading, provided in the longitudinal direction only, was compared to the same location on the FEA model. The linear strain

gages (CEA-06-125UW-350) chosen were a general purpose strain gage with a 350 Ω resistance, which was suggested for composite applications. The gages were attached on the proximal, lateral surface of the femur as shown, Figures 2.16(a)-2.16(d). The vertical alignment of each linear strain gage along the femur was as follows: gages one and two-50 mm from the top of the femur, gage three-105 mm from the top of the femur, gage four-145 mm from the top of the femur, and gage five-185 mm from the top of the femur. Gages three, four, and five were placed along the midline of the shaft, and gages one and two were placed 10.2 mm to the right or left of the center of the cross pin hole. The strain gage rosette was placed 60 mm vertically downward from the top of the femur with grid three of the gage placed midline.

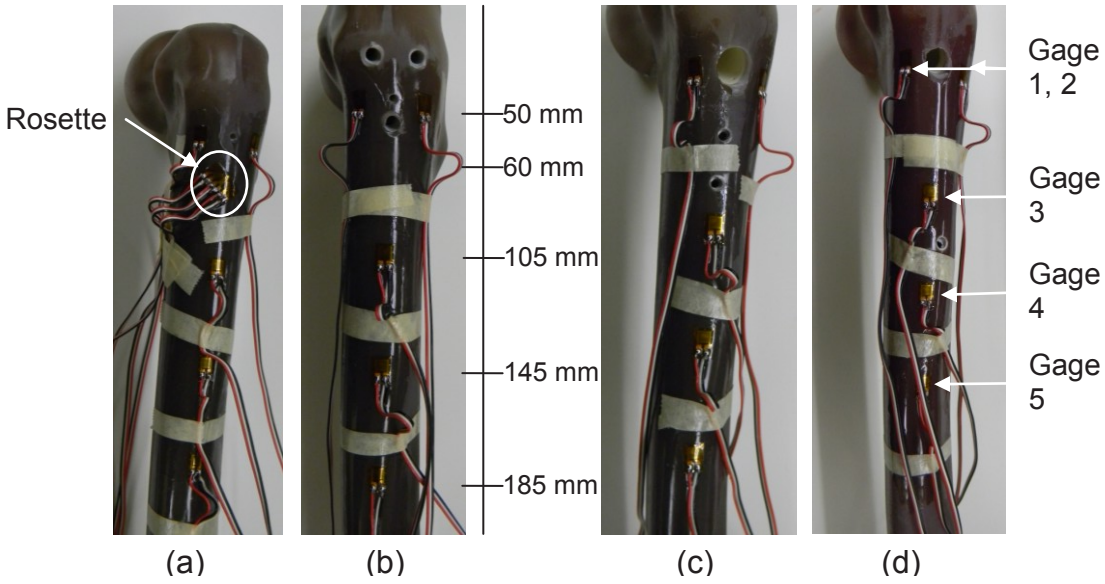

Figure 2.16. Strain gage attachment. (a) Control, (b) Cannulated screw, (c) DHS, (d) IHS

The strain gage attachment process on such an irregular surface provided several challenges and required a very specific, skilled procedure. The

installation was analogous to that provided within the technical bulletin obtained from the manufacturer with a few small modifications (Vishay Measurements Group, 1992). The lateral surface of the femur from mid-shaft to the greater trochanter was first degreased with a mild degreaser (FTF-1), Micro Measurements, Raleigh, NC), wiped with isopropyl alcohol and then dry sanded with 220 grit sandpaper and 320 grit sandpaper. This was followed by wet sanding with 320 grit and 400 grit sandpapers using M-Prep Conditioner A (Micro Measurements, Raleigh, NC). Locations for strain gages were identified and placement lines were burnished with a pencil. Next, the surface was cleaned with M-Prep Conditioner A on a cotton swab followed by a final scrubbing with M-Prep Neutralizer 5A (Micro Measurements, Raleigh, NC) on a gauze pad. Using a glass slide cleaned with isopropyl alcohol, each strain gage was first placed face up on the slide and covered with a small piece of cellophane tape. The tape was peeled back at a small angle until fully removed from the slide. The taped gage was then placed on the femur and then peeled back from the edge until the interface of gage edge and tape was visible and exposing the full bottom surface of the gage. The gage was lightly brushed with a catalyst (M-Bond 200 Catalyst, Micro Measurements, Raleigh, NC) and allowed to dry for sixty seconds. Next, a drop strain gage adhesive (M-Bond 200 Adhesive, Micro Measurements, Raleigh, NC) was applied at the tape/gage/slide interface. Holding the tape taut at a 30° angle, a piece of gauze was used to brush across the tape and seal the gage to the femur. Pressure was applied using the thumb directly over the gage for 60 seconds, then the thumb was removed and another three minutes passed

before gently removing the cellophane tape. The adhesive curing time was 6 hours; therefore attachment of the lead wires took place on the day following the gage application.

Conducting lead wires, 326-DFV (Vishay, Raleigh, NC) were attached according to the following procedure. Wires were cut to 3 ft sections, thermally stripped 0.5 in on each end and then separated (red from black and white) at a distance of 1 in on one end and 2.5 in on the other end. The wires were twisted and tinned with solder.

The adhered gages were protected by covering the grid with drafting tape. Wires were taped to the femoral surface and soldered to the gages. Rosin solvent was applied to float away the drafting tape both across the gage and across the wire. Strain relief loops were created at the base of each gage and then taped to the femur distal to the loop. In the case of the two proximal gages (numbers one and two) tape was also placed proximal to the loop due to the irregularity of the geometry and to provide stabilization of the wire and gage.

Finally, a protective coating of M-Coat A (Vishay, Raleigh, NC) was applied over the gage, solder terminals, and tape to both seal and protect the assembly.

CHAPTER 3

EXPERIMENTAL RESULTS

Fracture patterns for each treatment group were recorded noting the clinical fracture classification, potential crack initiation site(s), and any anomalies in the fractured cross-section. The load at fracture was recorded for each treatment group, means for each group were calculated, and results of the treated femur groups compared to the control mean load at failure. Load-deflection curves were prepared for all groups and compared against the mean control load-deflection curve. Longitudinal strain values were obtained from each of the five strain gages affixed to the samples. Profiles were created to illustrate the strain variations along the lateral surface of the femur at the onset of the test, at 30% of failure load, at 60% of failure load and at fracture. Strains were also recorded from the rectangular rosettes (one from each treatment group); principle stresses, strains, and von Mises stresses were calculated. Finally, each test was filmed with a high definition video camera in order to evaluate the usefulness of optical elastography in this test medium and to aid in the validation of the FEA model. Elastograms for one of the cannulated screw, residual holes samples were developed and an initial stress-strain curve was prepared based on the algorithms presented in Section 2.2.3

3.1 Fracture Analysis

Control Group

The control group was not augmented and the femurs were tested as received from the manufacturer.

The first control sample tested did not fail initially and the test ceased after obtaining a 10 mm vertical deflection. After some evaluation of the test method, it was determined that a few additional adjustments in the software were necessary to ensure that the preload and load were applied appropriately. The sample was re-run and failed within the range of the other control sample values except for the type of clinical fracture as noted below.

Clinical fracture classifications for the control group resulted in one subtrochanteric fracture and two Pauwel's Type III fractures. Sample one, a subtrochanteric fracture, Figure 3.1(a), failed through the cross pin hole found on the proximal lateral surface of the shaft. Samples two and three both exhibited Pauwel's Type III fractures, Figures 3.1(b) and 3.1(c).

(a) (b) (c)

Figure 3.1. Control fracture pattern. (a) Sample 1: Subtrochanteric, (b) Sample 2: Pauwel's Type III, (c) Sample 3: Pauwel's Type III

The proximal femoral shaft segment of sample one showed the failure of the bone through the cross pin hole on the lateral surface, Figure 3.2(a). The same cross pin holes throughout the neck geometry were shown in the cross-section views of the femoral heads from samples two and three. A crack site and secondary crack front were identified on sample two, Figure 3.2(b) and two crack lines were identified on sample three, Figure 3.2(c).

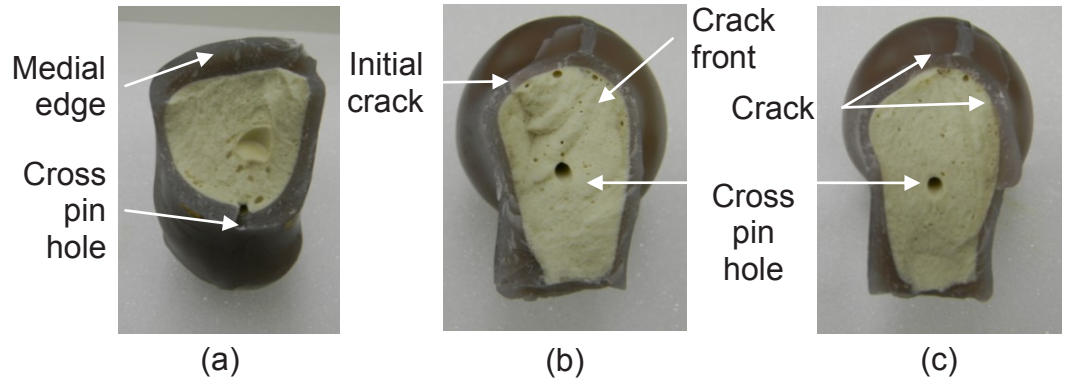

Figure 3.2. Control femoral head fracture view. (a) Sample 1, (b) Sample 2, (c) Sample 3

Cannulated Screw, Residual Holes Group

The cannulated screw group was augmented with three cannulated screws per femur and tested with the residual holes.

Fracture classifications for the cannulated screws (CS), residual holes treatment group resulted in one basicervical fracture (sample four), one Pauwel's Type III fracture (sample five), and one subtrochanteric fracture (sample six), Figure 3.3(a)-3.3(c). Sample six failed through the bottom cannulated residual screw hole.

(a) (b) (c)

Figure 3.3. Cannulated screws fracture pattern. (a) Sample 4: Basicervical, (b) Sample 5: Pauwel's Type III, (c) Sample 6: Subtrochanteric

The cross-section of sample four showed the locations of the cannulated screws and cross pin hole, Figure 3.4(a). The top, right screw location was offset and grazed the inside surface of the cortical bone. The cross-section view of sample five showed a more uniform placement of the screws in the femoral head, Figure 3.4(b). Two cracks were identified and subtle regions of crack propagation were seen in the cancellous bone. Sample six failed through the center of the bottom residual hole, Figure 3.4(c).

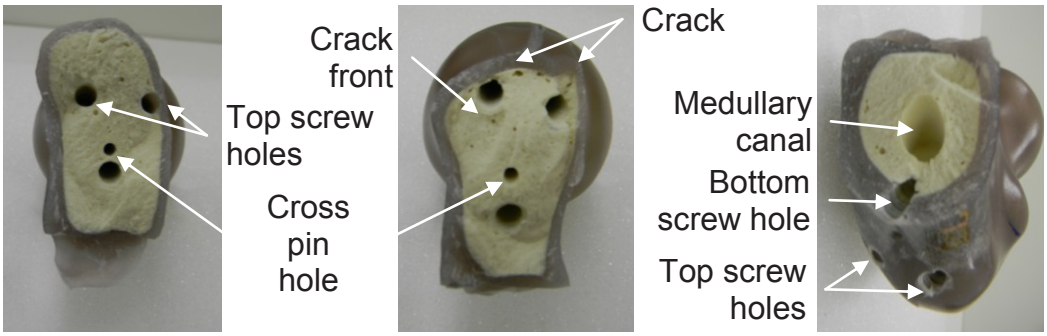

(a) (b) (c)

Figure 3.4. CS femoral head fracture view. (a) Sample 4, (b) Sample 5, (c) Sample 6

A close up of the neck region in sample five, Figure 3.5, showed a significant defect created in the cortical bone due to the placement of the top, right screw also shown in Figure 3.1(b).

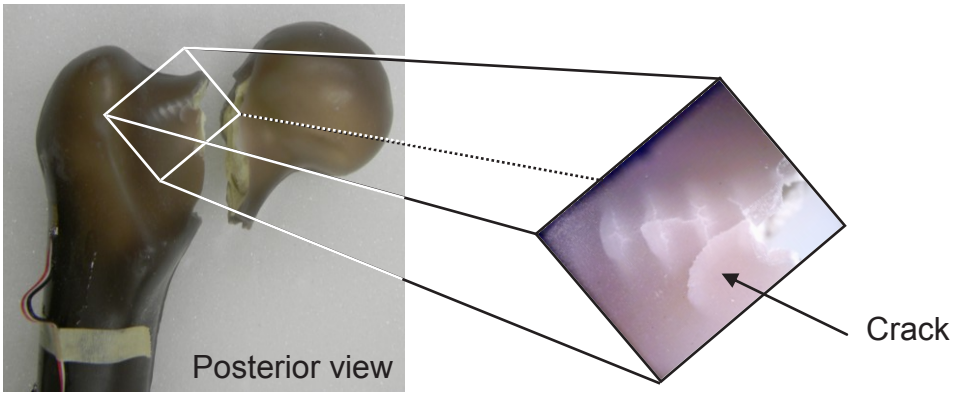

Figure 3.5. Stress riser related to residual screw hole location in neck-Sample 5

Cannulated Screw, Cement-Filled Holes Group

The cannulated screw, cement-filled group was first augmented with three cannulated screws per femur, the hardware was subsequently removed, and the holes filled with Norian SRS cement.

The cannulated screws, cement-filled residual holes (CSC) treatment group exhibited two different fracture types. The clinical fracture classifications resulted in one basicervical fracture and two Pauwel's Type III fractures. Sample seven, a basicervical fracture, Figure 3.5(a), failed at the base of the neck, just before the trochanters. Samples eight and nine both exhibited Pauwel's Type III fractures, Figures 3.5(b) and 3.5(c).

(a) (b) (c)

Figure 3.6. Cannulated screws, cement-filled holes fracture pattern. (a) Sample 7: Basicervical, (b) Sample 8: Pauwel's Type III, (c) Sample 9: Pauwel's Type III

Sample seven retained all of its cement following fracture and a neck cross-section showed the top right screw exceptionally close to the inside edge of the cortical bone, Figure 3.7(a). The cross-section view of the femoral heads from samples eight and nine showed the location of the top left screw hole impinging on the inner surface of the cortical bone, Figures 3.7(b) and 3.7(c). Crack sites were also identified. Cement remained in all but one (top left, sample eight) residual screw hole after fracture.

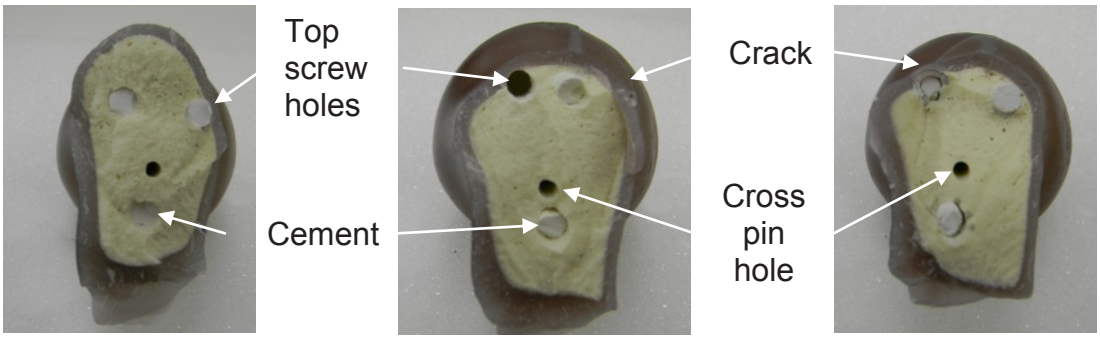

(a) (b) (c)

Figure 3.7. CSC femoral head fracture view. (a) Sample 7, (b) Sample 8, (c) Sample 9

Further inspection of the residual screw hole locations revealed defects in the cortical layer as a result of the initial screw placement in two of the samples and cracking near the hole in the second sample. A Nikon SMZ800 microscope under 1x magnification was used to evaluate the fractured surfaces. Images were captured with a PixelLINK Megapixel FireWire Camera and Megapixel Release 3.2 software. Under simple magnification, it was shown that cortical bone was removed to almost half the original thickness in sample seven, Figure 3.8(a). In sample eight, a crack through the cortical layer was located directly across from the residual screw hole, Figure 3.8(b). The cortical layer in sample nine was thinned to the point that the threads from the screw removal could be observed from the outside, Figure 3.8(c).

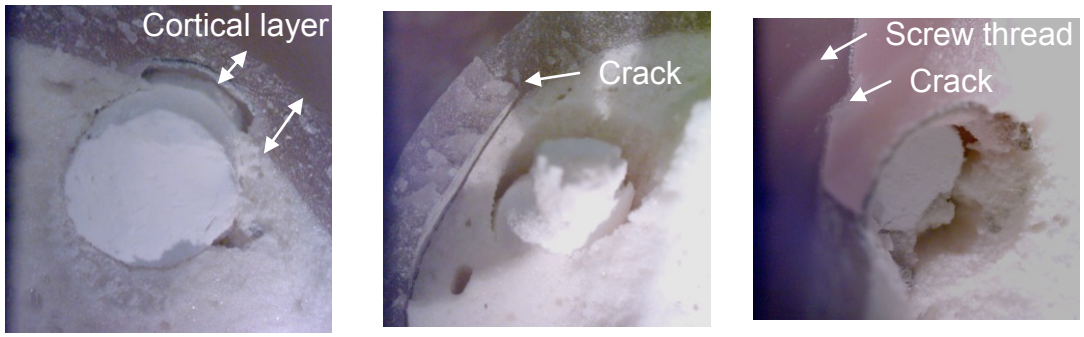

(a) (b) (c)

Figure 3.8. Femoral head fracture view magnified. (a) Sample 7, (b) Sample 8, (c) Sample 9

Dynamic Hip Screw, Residual Holes Group

The dynamic hip screw, residual holes group (DHS) was augmented with one lag screw, two cortex screws, and a plate. The hardware was removed and the femurs were tested with the residual holes.

Fracture classifications for the DHS group resulted in three subtrochanteric fractures, samples ten, eleven, and twelve. Crack(s) began at the location of the distal cortex residual screw hole on the lateral surface and propagated perpendicularly to the tensile surface. As the crack approached the compressive surface it slowed and changed direction trying to maintain its relationship with the tensile surface, leaving behind a lip (cantilever curl) just before final rapid fracture, Figure 3.9(a)-3.9(c).

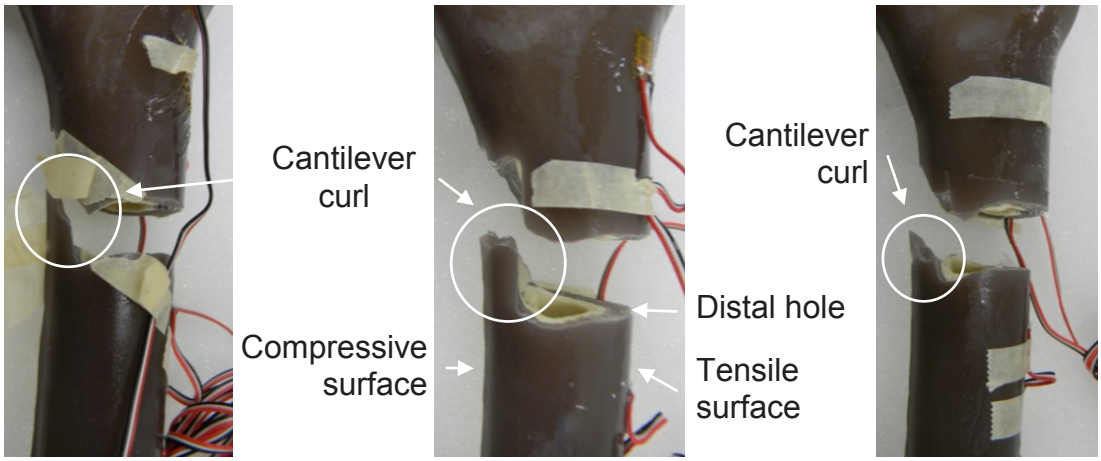

Figure 3.9. DHS fracture pattern. (a) Sample 10: Subtrochanteric, (b) Sample 11: Subtrochanteric, (c) Sample 12: Subtrochanteric

Proximal femoral shaft cross-sections of each sample clearly showed the failure of the bone through the residual distal cortex screw hole on the lateral surface, Figures 3.10(a)-3.10(c). In each case, the failure occurred through the center of the hole on the lateral surface, propagated through the lateral cancellous layer and captured the residual hole on the medial side of the cancellous layer. The crack slowed and changed direction in the cortical layer of the medial surface.

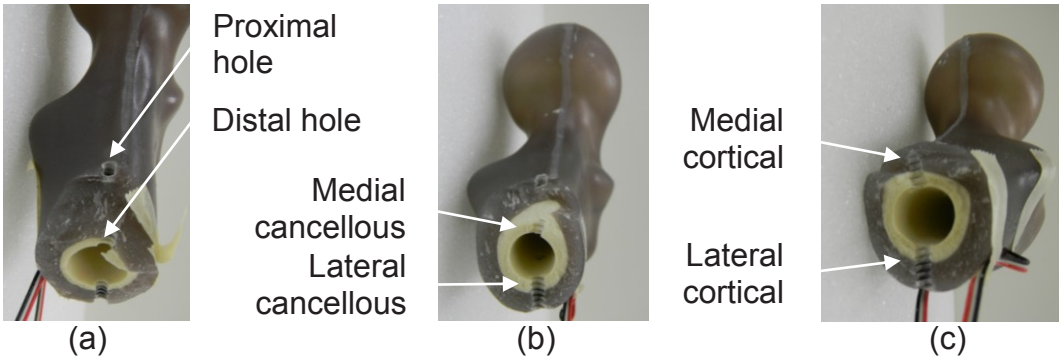

Figure 3.10. DHS proximal femur fracture view. (a) Sample 10, (b) Sample 11, (c) Sample 12

Dynamic Hip Screw, Cement-Filled Holes Group

The dynamic hip screw, cement-filled holes (DHSC) group was augmented with DHS hardware which was then subsequently removed and the residual holes filled with Norian SRS cement.

The DHSC group also resulted in three subtrochanteric fractures, samples thirteen, fourteen, and fifteen. Crack propagation was analogous to the failures in the DHS group previously described, Figures 3.11(a)-3.11(c).

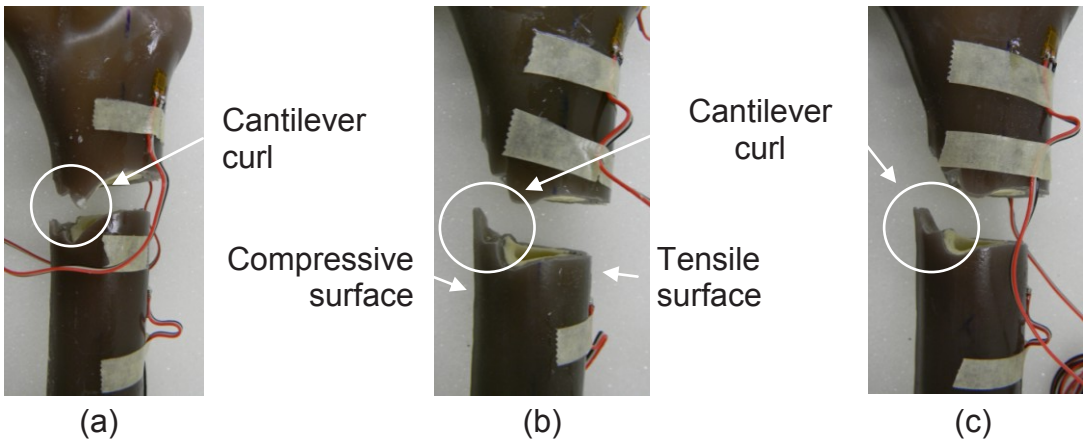

Figure 3.11. DHS, cement-filled holes fracture pattern. (a) Sample 13: Subtrochanteric, (b) Sample 14: Subtrochanteric, (c) Sample 15: Subtrochanteric

The proximal cross-sections of each sample illustrated failure similar to the DHS residual screw hole group, Figures 3.12(a)-3.12(c). However, in sample thirteen, the crack began at the proximal screw hole. Crack propagation followed the path previously described, regardless of which hole served as the point of crack initiation.

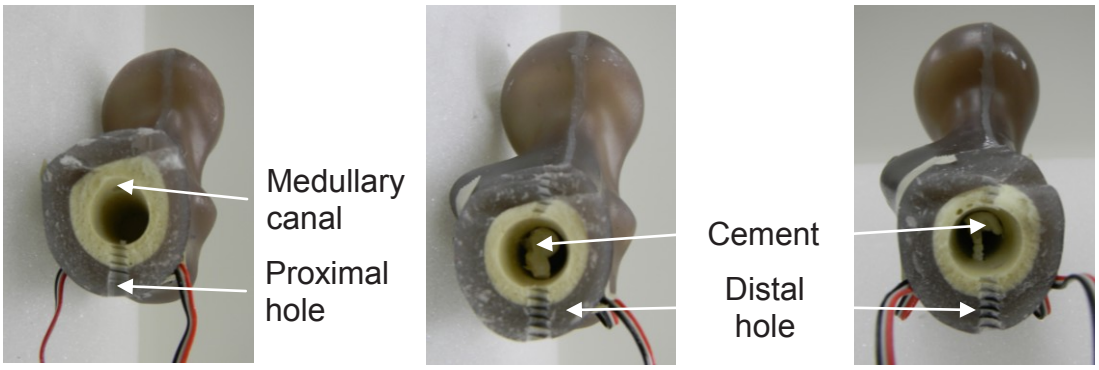

Figure 3.12. DHSC proximal femur fracture view. (a) Sample 13, (b) Sample 14, (c) Sample 15

Intramedullary Hip Screw, Residual Holes Group

The intramedullary hip screw, residual holes (IHS) group was augmented with a trochanter fixation nail (TFN), lag screw, and distal cortex screw. The hardware was removed and the femurs were tested with the residual holes.

Fractures for the IHS group resulted in one subtrochanteric fracture and two intertrochanteric fractures. Sample sixteen, a subtrochanteric fracture, Figure 3.13(a), failed through the distal cortical residual screw hole on the lateral surface of the shaft. Samples seventeen and eighteen both exhibited intertrochanteric fractures, failing through the entry hole of the TFN, Figures 3.13(b) and 3.13(c).

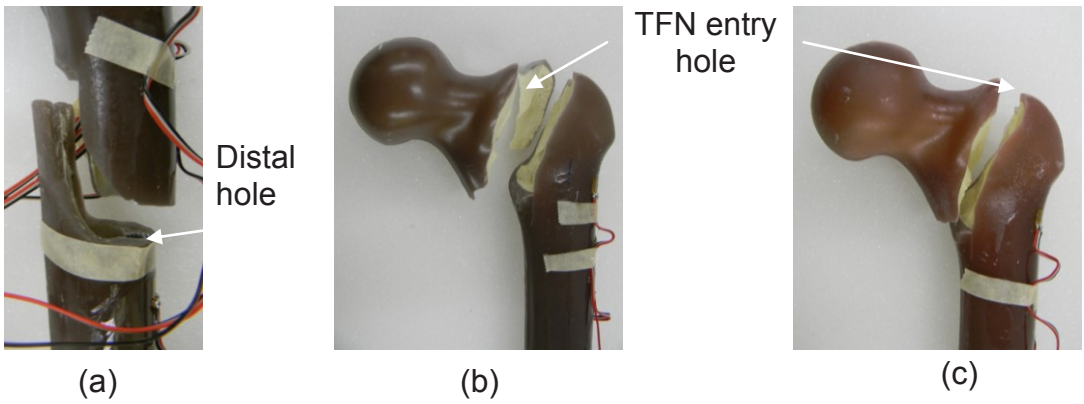

Figure 3.13. IHS fracture pattern. (a) Sample 16: Subtrochanteric, (b) Sample 17: Intertrochanteric, (c) Sample 18: Intertrochanteric

The proximal shaft of sample sixteen showed the failure of the bone through the distal locking screw and displayed a large cantilever curl, Figure 3.14(a). The cross-section views of the femoral heads from samples seventeen and eighteen showed the failure though the entry hole for the TFN and in both cases, bone fragments splintered off from the neck showing several different simultaneous crack fronts, Figures 3.14(b) and (c).

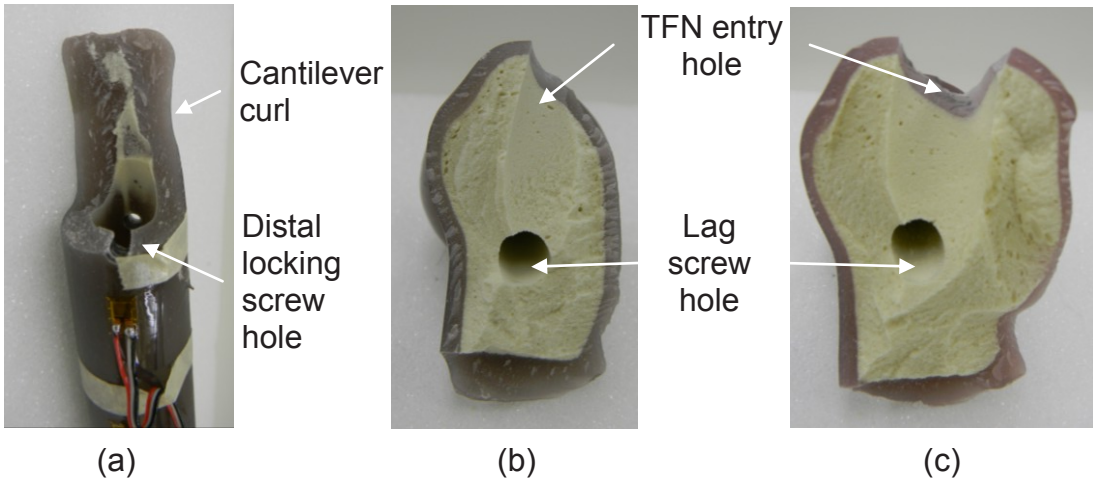

Figure 3.14. IHS fracture views. (a) Sample 16, (b) Sample 17, (c) Sample 18

Intramedullary Hip Screw, Partial-Removal Residual Holes Group

The intramedullary hip screw, partial-removal residual holes (IHSP) group was augmented with the IHS hardware followed by the removal of the lag screw. The samples were tested with the residual holes and the retained hardware.

The fracture classifications for the IHSP group resulted in two intertrochanteric fractures and one subtrochanteric fracture. Samples nineteen and twenty, failed through the entry point of the TFN, Figures 3.15(a) and 3.15(b). A subtrochanteric fractured was observed in sample twenty-one, where a medial fragment also separated from the bone, Figure 3.15(c).

Figure 3.15. IHS, partial removal fracture pattern. (a) Sample 19: Intertrochanteric, (b) Sample 20: Intertrochanteric, (c) Sample 21: Subtrochanteric

Samples twenty and twenty-one showed failure analogous to those discussed in the IHS residual holes section. In each case, the crack began at the insertion point of the TFN and propagated in two locations simultaneously, Figures 3.16(a) and 3.16(b). The cross-section view of the proximal femur from sample twenty-one showed a typical failure due to flexural stresses as discussed

in the DHS residual holes section. In addition, a medial fragment of the cortical bone occurred at the level of the tip of the TFN, Figure 3.16(c).

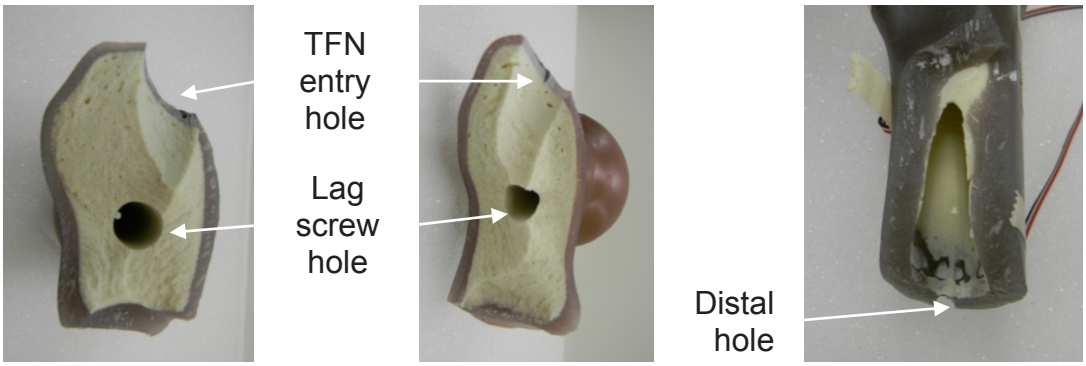

Figure 3.16. IHSP femoral head fracture view. (a) Sample 19, (b) Sample 20, (c) Sample 21

Analysis of the clinical fracture patterns led a total of four different fracture classifications, Table 3.1.

Table 3.1. Summary of fracture classifications by treatment group

Treatment group	Basicervical	Intertrochanteric	Pauwel's Type III	Subtrochanteric
Control	0	0	2	1
CS	1	0	2	0
CSC	1	0	2	0
DHS	0	0	0	3
DHSC	0	0	0	3
IHS	0	2	0	1
IHSP	0	2	0	1
Totals	*2*	*4*	*6*	*9*

3.2 Axial Load at Failure

The compressive load at failure was reported for each sample, Figure 3.17(a). A linear trendline was formulated for the data and the calculated R^2 value

was 0.4053. Data for samples eight, nine, and nineteen were significantly less than expected. Percent deviation was calculated for each sample:

$$Percent\ deviation = \frac{measured\ value - mean}{mean} \times 100 \tag{3.1}$$

where the *mean* was the mean trendline value from each sample group. The percent deviation for samples eight, nine, and nineteen fell far below the expected values. This led to some questions as to whether the failure was more indicative of the material itself (e.g.: internal voids) as opposed to a failure related to a particular treatment. Elaboration on this subject can be found in Chapter 6. Removing the samples in question led to a new R^2 value of 0.8138, Figure 3.17(b).

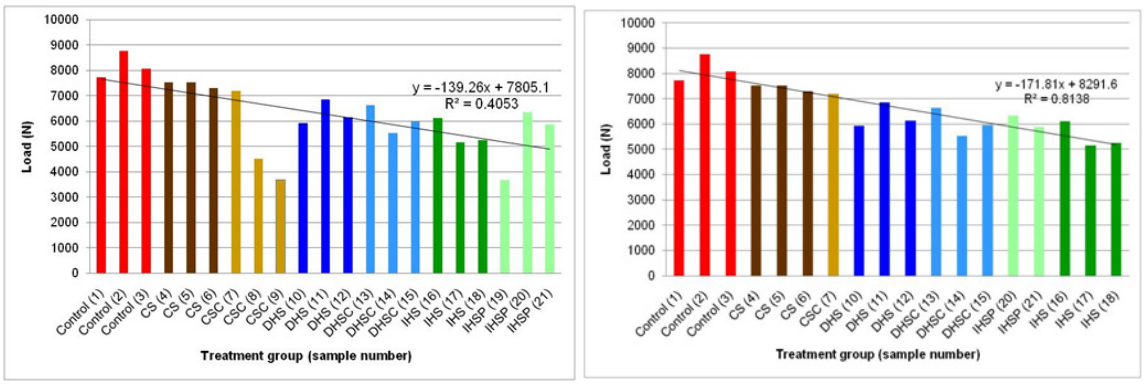

(a) (b)

Figure 3.17. Failure load by sample and treatment group. (a) Full sample set, (b) Samples 8, 9, and 19 removed

The mean load at failure was calculated and all treatment groups were reported as a percentage of the control, Figure 3.18. Loads at failure, excluding the three questionable samples, were highest in the control group, 8,183.2 ± 529.1 N and lowest in the IHS group, 5,505.3 ± 532.0 N.

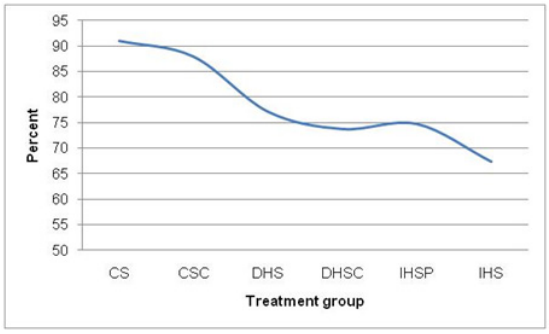

Figure 3.18. Load at failure results as percentage of mean control values

3.3 Axial Deflection

All included samples exhibited linear load-deflection behavior, Figures 3.19(a)-3.19(d).

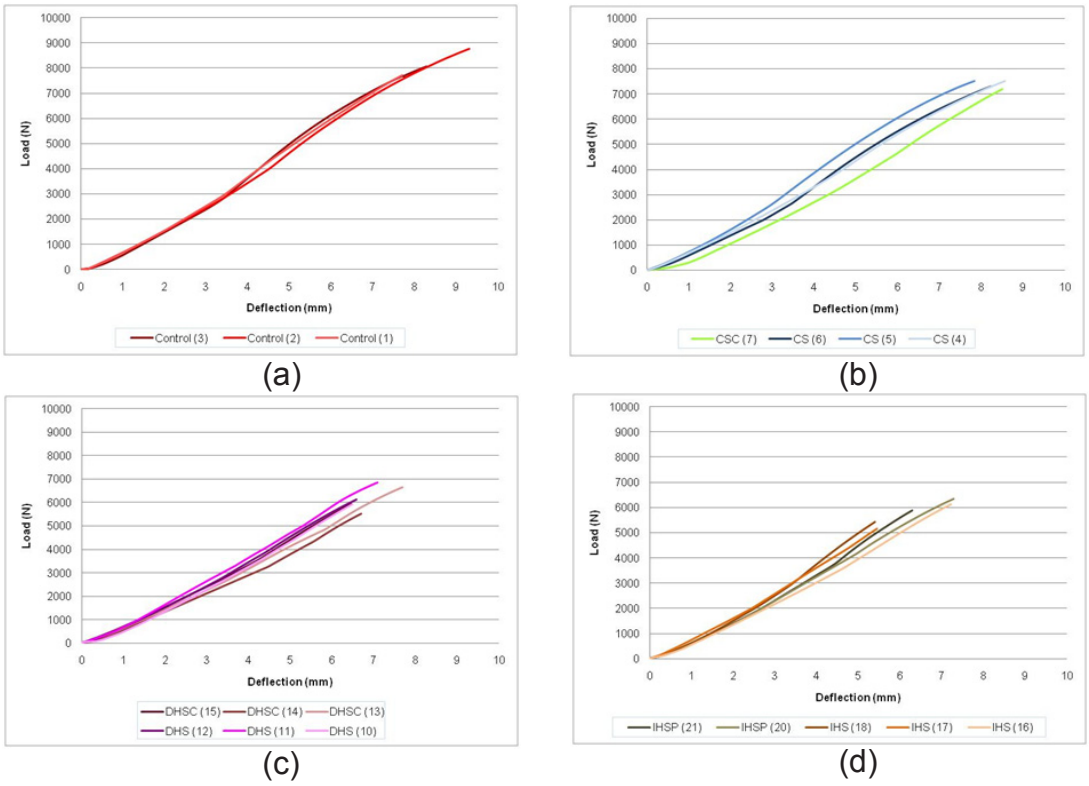

Figure 3.19. Load deflection diagrams for each treatment group. (a) Control, (b) CSC and CS, (c) DHSC and DHS, (d) IHSP and IHS

The control group, as expected, withstood the largest overall deflection and failed at the highest loads. Analysis of the cement-filled holes versus the non-treated residual holes in the cannulated screw groups and DHS groups showed that the average load at deflection was less in the cement groups. In all treatment groups, the load cell values between the initial application of the load and an overall compression of 4 mm correlated closely to each other. After 4 mm, the treatment groups diverged, Figure 3.20.

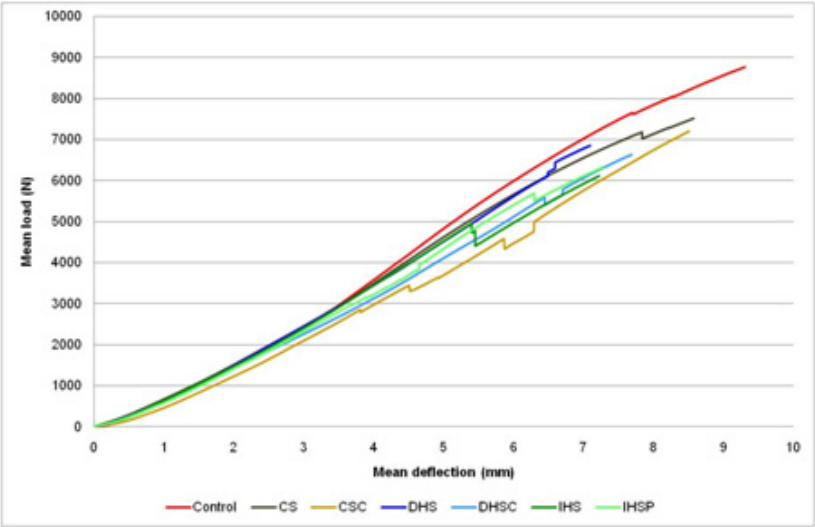

Figure 3.20. Load-deflection diagram for all treatment groups

3.4 Strain Gage Analysis

Strain data was recorded and plotted along the longitudinal axis of the femur. The first and second strain gages were located on either side of the cross pin hole (approximately 50 mm from the top of the bone). Those strains were averaged and recorded as one value. The strains increased from gages one and two through gage three, where peak strains were observed. Strains then

decreased through the fourth and fifth gages (approximately 185 mm from the top of the bone). Strains were plotted at the time of initial load, 30% of the load at failure, 60% of the load at failure, and at final failure, Figures 3.21(a)-3.21(d). The most dramatic change occurred between 60% of the load and failure, wherein a clear definition between the different treatment groups was visible. The highest strains were exhibited by the control and decreased with each subsequent treatment group.

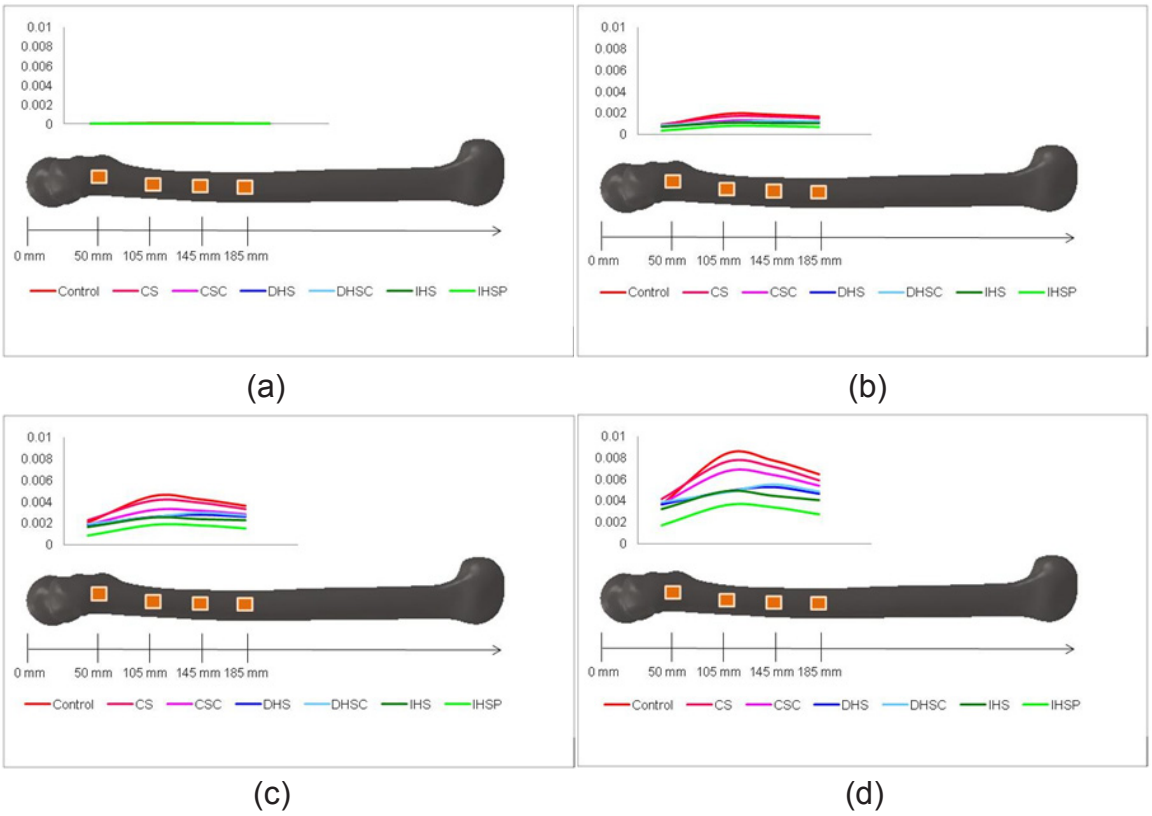

Figure 3.21. Lateral strain profile as a function of time. (a) Initial loading, (b) 30% of failure load, (c) 60% of failure load, (d) Strain at break

Mean strains at failure were also compared to the mean control strains and reported as a percentage, Table 3.2. Values at each gage location were

calculated and for the control group the results were as follows: gage 1-anterior, $3.67e^{-3} \pm 4.96e^{-4}$ mm/mm; gage 2-posterior, $3.64e^{-3} \pm 2.01e^{-4}$ mm/mm; gage 3, $8.38e^{-3} \pm 8.32e^{-4}$ mm/mm; gage 4, $7.79e^{-3} \pm 1.01e^{-3}$ mm/mm; gage 5, $6.48e^{-3} \pm 7.65e^{-4}$ mm/mm.

Table 3.2. Average strains at break as a percentage of the control

Treatment group	Gage 1	Gage 2	Gage 3	Gage 4	Gage 5
CS	77.9	75.3	90.9	92.3	91.1
CSC	104	101	80.3	82.5	83.5
DHS	63.9	68.4	57.5	67.2	71.1
DHSC	99.8	110	56.8	71.0	74.7
IHS	83.4	92.5	57.8	56.9	62.2
IHSP	53.8	84.9	63.9	65.2	63.0

Surface strains from five rectangular strain gage rosettes were collected and analyzed according to the process provided in the technical bulletin from the manufacturer (Vishay Measurements Group, 2010). The planar rosette was located just below the cross pin hole on the proximal lateral surface of the femur with grid one (gage six) oriented-circumferentially, grid two-obliquely (gage seven), and grid three (gage 8)-longitudinally, Figure 3.22.

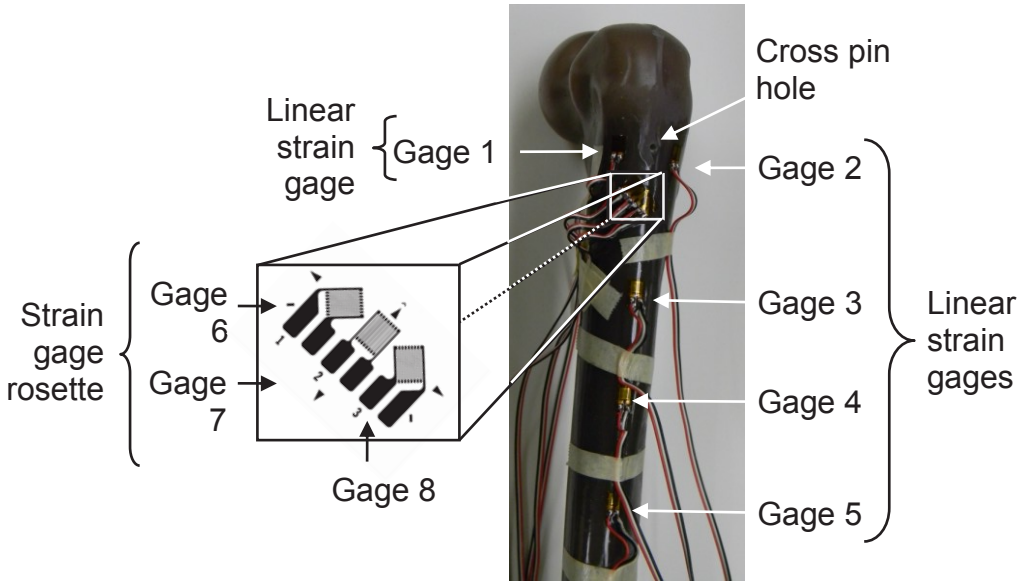

Figure 3.22. Strain gage placement

The material was assumed homogenous and isotropic with a linear stress/strain relationship. Principal strains, $\varepsilon_{P,Q}$, were determined from equation (3.2) utilizing the measured strains from each grid of the rosette, ε_1, ε_2, ε_3. Poisson's ratio, $\nu = 0.26$ for cortical bone, and the elastic modulus, $E = 167\ MPa$ for cortical bone, were provided by Pacific Research Laboratories, Inc. for the composite.

$$\varepsilon_{P,Q} = \frac{\varepsilon_1 + \varepsilon_3}{2} \pm \frac{1}{\sqrt{2}} \sqrt{(\varepsilon_1 - \varepsilon_2)^2 + (\varepsilon_2 - \varepsilon_3)^2} \tag{3.2}$$

$$\theta = \frac{1}{2} \tan^{-1}\left(\frac{\varepsilon_1 - 2\varepsilon_2 + \varepsilon_3}{\varepsilon_1 - \varepsilon_3}\right) \tag{3.3}$$

The principal angle, θ, is the angle from the principal axis to the reference grid of the rosette. The principal angle was calculated with equation (3.3) and by convention, positive angle values were located counterclockwise from the

principal axis and negative values were located clockwise from the principal axis, Figure 3.23.

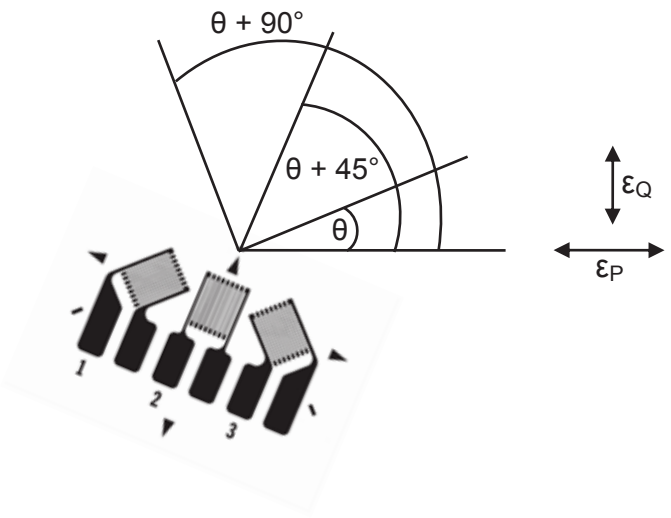

Figure 3.23. Strain gage rosette installation angles

The resulting strains, applied angles, and von Mises equivalent strain for the five rosettes are noted in Table 3.3.

Table 3.3. Principal and von Mises strains and angle calculated from rosette

Treatment group	ε_P (mm/mm)	ε_Q (mm/mm)	$\varepsilon_{von\ Mises}$ (mm/mm)	θ
Control	5.78 E^{-3}	-4.14 E^{-3}	7.02 E^{-3}	-0.06
CS	4.27 E^{-3}	-2.10 E^{-3}	4.50 E^{-3}	-0.13
DHS	3.64 E^{-3}	-1.37 E^{-3}	3.54 E^{-3}	-0.19
IHS	3.50 E^{-3}	-1.35 E^{-3}	3.43 E^{-3}	-0.21
IHSP	2.42 E^{-3}	-1.10 E^{-3}	2.49 E^{-3}	-0.23

Hooke's law, $E = \sigma/\varepsilon$, was applied to convert the principal strains, $\varepsilon_{P,Q}$, into principal stresses, $\sigma_{P,Q}$

$$\sigma_P = \frac{E}{1 - \upsilon^2}\left(\varepsilon_P - \upsilon\varepsilon_Q\right) \tag{3.4}$$

$$\sigma_Q = \frac{E}{1 - \upsilon^2}\left(\varepsilon_Q - \upsilon\varepsilon_P\right) \tag{3.5}$$

Combining equations (3.4) and (3.5),

$$\sigma_{P,Q} = \frac{E}{2}\left[\frac{\varepsilon_1 + \varepsilon_3}{1-\upsilon} \pm \frac{\sqrt{2}}{1+\upsilon}\sqrt{(\varepsilon_1 - \varepsilon_2)^2 + (\varepsilon_2 - \varepsilon_3)^2}\right] \quad (3.6)$$

The calculated principal stresses are reported in Table 3.4. Tensile stresses are indicated as (T) and compressive forces indicated as (C). The von Mises equivalent stress was also calculated using equation (3.7) and reported in Table 3.4.

$$\sigma_{von\ Mises} = \sqrt{\frac{1}{2}\left(\varepsilon_P - \varepsilon_Q\right)^2} \quad (3.7)$$

Table 3.4. Principal and von Mises stresses calculated from rosette

Treatment group	σ_P (MPa)	σ_Q (MPa)	$\sigma_{von\ Mises}$ (MPa)
Control	99.3 (T)	-8.64 (C)	72.8
CS	66.2 (T)	-22.8 (C)	68.5
DHS	58.9 (T)	-7.56 (C)	47.0
IHS	39.6 (T)	-60.4 (C)	45.5
IHSP	38.2 (T)	-8.47 (C)	33.0

3.5 Optical Elastography Preliminary Results

An elastogram for the cannulated screw, residual holes sample four was developed. The images in Figures 3.24(a)-3.24(f) show the failed femur, Figure 3.24(a), and compare it to the progression of images from the optical elastography. The image of the ROI was cropped and shown in Figure 3.24(b). The horizontal and vertical motion of the ROI just before failure was captured and shown in Figures 3.24(c) and 3.24(d), respectively. Finally, a vertical strain image

and the magnitude of the vertical strain image were prepared, Figures 3.24(e) and 3.24(f).

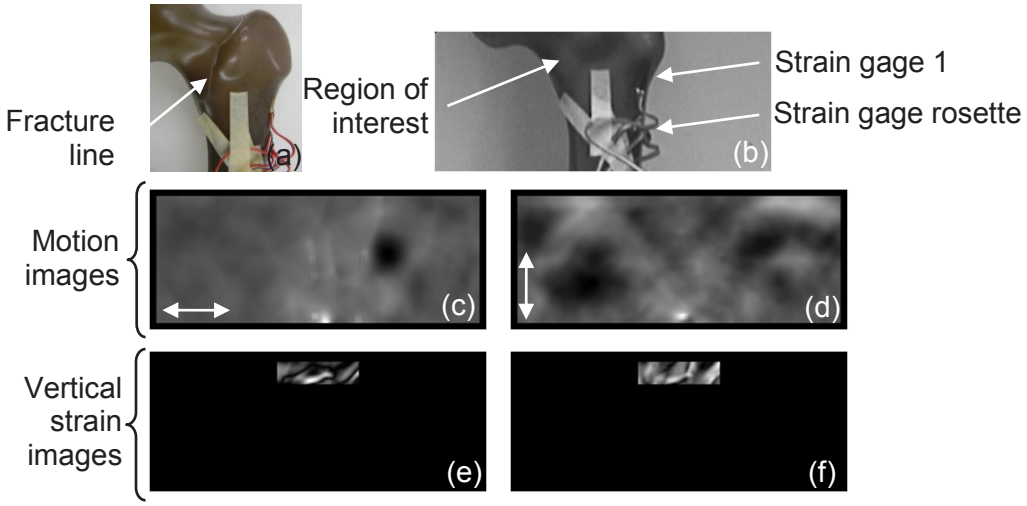

Figure 3.24. Optical elastography images. (a) Fractured femur, (b) ROI, (c) Horizontal motion, (d) Vertical motion, (e) Vertical strain image, (f) Magnitude of vertical strain image

The images were taken just before failure and in an area above the tape and wires. The brighter regions (pixels) in the vertical strain images, Figures 3.24(d) and 3.24(e) represented places of high strain. Those regions were qualitatively correlated to the fracture line of the failed femur, Figure 3.24(a).

Finally, a preliminary stress-strain curve was prepared based on the data collected from the compression tests, Figure 3.25. Both curves represented the entire deformation history of the bone, noting that the curve from the Instron was for the full length of the bone and the curve from the optical elastography was for a specific ROI. It is important to note that the data calculated from the load cell of the Instron testing machine was based on a general geometry of the specimen entered into the software, in this case an average cylinder. Therefore, the

presented stress-strain curve is only a beginning approximation and future work will be necessary in order to develop more appropriate stress-strain curves that can calibrate the strain elastograms.

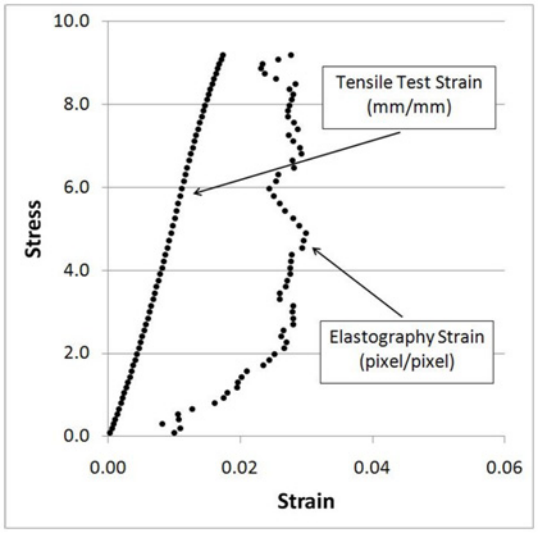

Figure 3.25. Stress-strain diagram comparing experimental to elastography

CHAPTER 4

COMPUTATIONAL ANALYSIS

Finite element analysis (FEA) was used to conduct the computational portion of this study. This form of analysis allows for the division of a complex problem into subdivisions of simpler problems that can be solved using numerical techniques. The finite elements that are used to model these smaller problems must be selected carefully in order to provide a reasonable representation of the boundaries of the problem as well as the varying deflection, stress, and strain fields of the model (Budynas, 1999). The computational process is made up of three basic stages, preprocessing (model creation, definition of elements, loads, and boundary conditions), processing (problem solving and creation of data base), and postprocessing (analysis review and graphical presentation of results). In order to solve for the deflection, stress, and strain fields of the difficult geometry of the composite femur, a simplified pipe model was first created to provide some baseline on which the FE model could be developed. Then, following the creation of the actual 3D solid models of the femurs and respective augmentations, the models were imported into a commercial FEA program, where the models were further defined by the selection of appropriate elements, nodes, loads, boundary conditions, and material parameters.

4.1 Finite Element Analysis Theory

The geometry of the composite femur was subdivided into solid elements. A tetrahedral element, a basic 3D element, was used for the building block of the model and allowed for the creation of stiffness matrices and force matrices in terms of a global coordinate system (Budynas, 1999). Each solid element allows three degrees of freedom at each of its nodes. These degrees of freedom represent the translational and rotational motion that can exist at a node; displacements *u, v, w* in the *x-, y-,* and *z*-directions, respectively, Figure 4.1.

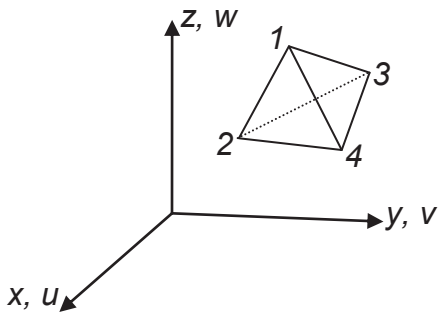

Figure 4.1. Tetrahedral element

The relationship between the nodal forces and nodal displacements of an element are given by the stiffness matrix. This stiffness matrix, *[k]*, for an element is a matrix such that

$$\{f\} = [k]\{d\} \tag{4.1}$$

where *{f}* is the local force on the element and *{d}* is nodal displacement. The stiffness matrix is reflective of the material properties and geometry of the element.

Next, the displacement functions, *u*, *v*, and *w* are defined. These functions must be linear along the edge and plane of the tetrahedral element.

$$u(x,y,z) = a_1 + a_2x + a_3y + a_4z$$

$$v(x,y,z) = a_5 + a_6x + a_7y + a_8z$$

$$w(x,y,z) = a_9 + a_{10}x + a_{11}y + a_{12}z \tag{4.2}$$

The a_i terms in equation (4.2) can be expressed in terms of the nodal coordinates ($x_1, y_1, z_1, \ldots z_4$) and the unknown nodal displacements ($u_1, v_1, w_1, \ldots w_4$) by substituting in the coordinates of the nodal points into equation (4.2).

$$u(x,y,z) = \frac{1}{6V}\{(\alpha_1 + \beta_1x + \gamma_1y + \delta_1z)u_1 + (\alpha_2 + \beta_2x + \gamma_2y + \delta_2z)u_2 + (\alpha_3 + \beta_3x + \gamma_3y + \delta_3z)u_3 + (\alpha_4 + \beta_4x + \gamma_4y + \delta_4z)u_4\} \tag{4.3}$$

when *V* is the volume of the tetrahedron.

The displacement function for *u*, given by equation (4.3), with similar developments for *v* and *w*, can be expanded and written in terms of the shape function where

$$\begin{Bmatrix} u \\ v \\ w \end{Bmatrix} = \begin{bmatrix} N_1 & 0 & 0 & \cdots & N_4 & 0 & 0 \\ 0 & N_1 & 0 & \cdots & 0 & N_4 & 0 \\ 0 & 0 & N_1 & \cdots & 0 & 0 & N_4 \end{bmatrix} \begin{Bmatrix} u_1 \\ v_1 \\ w_1 \\ \cdots \\ u_4 \\ v_4 \\ w_4 \end{Bmatrix} \tag{4.4}$$

The shape functions of the displacement function are over the domain of the element. Expressions for the shape functions, N_1, N_2, N_3, and N_4 are given by

$$N_i = \frac{(\alpha_i + \beta_ix + \gamma_iy + \delta_iz)}{6V} \tag{4.5}$$

where *i =1, 2, 3, 4* and the shape function N_i corresponds to the nodal point with coordinates (x_i, y_i, z_i).

The definition of the elemental strain state includes three normal strains and three shear strains. If the displacements of an element are small compared to the dimensions, they are related to the strains by the following linear expressions.

$$\{\varepsilon\} = \begin{Bmatrix} \varepsilon_x \\ \varepsilon_y \\ \varepsilon_z \\ \gamma_{xy} \\ \gamma_{yz} \\ \gamma_{zx} \end{Bmatrix} where \quad \begin{aligned} \varepsilon_x &= \frac{\partial u}{\partial x} & \gamma_{xy} &= \gamma_{yx} = \frac{\partial u}{\partial y} + \frac{\partial v}{\partial x} \\ \varepsilon_y &= \frac{\partial v}{\partial y} & \gamma_{yz} &= \gamma_{zy} = \frac{\partial v}{\partial z} + \frac{\partial w}{\partial y} \\ \varepsilon_z &= \frac{\partial w}{\partial z} & \gamma_{zx} &= \gamma_{xz} = \frac{\partial w}{\partial x} + \frac{\partial u}{\partial z} \end{aligned} \tag{4.6}$$

Finally, the elemental stiffness matrix for a tetrahedral element can be expressed as

$$[k] = \iiint_V [B]^T [D][B]\, dV \tag{4.7}$$

Both matrices, *[B]* and *[D]* are constant for a tetrahedral element, therefore equation (4.7) can be simplified to

$$[k] = [B]^T [D]\, [B] V \tag{4.8}$$

where *V* is the volume of the element. The specific femoral model was further defined by the selection of appropriate elements, nodes, loads, boundary conditions, and material parameters.

4.2 Finite Element Analysis Validation

The commercial FEA package used in this study was Algor Professional Edition, 2011 (Autodesk, Algor Simulation Professional 2011). To help validate the results of the software package, a simplified geometric model of the femur was generated, tested, and the results compared to the theoretical calculation. A bent, cylindrical pipe was chosen as a simplified representation of the femur. The angle of the pipe was 120°, modeling the angle of the composite bone neck. Average diameters were taken from the CAD model for use in developing the pipe geometry. The internal diameter was set at 13 mm and the external diameter was set at 32 mm. The pipe model was meshed with 3 mm edge length tetrahedral elements. Material properties were assigned according to those provided by the composite bone manufacturer, v = 0.26 and E = 16,700 MPa. A vertical load of 9,000 N was applied to the end of the pipe as shown in Figure 4.2 at a distance of 72 mm from the shaft. Boundary conditions, T_{xyz}, were applied to the bottom surface of the pipe. The resulting stresses were 220 MPa on the compressive side and 194 MPa on the tensile side.

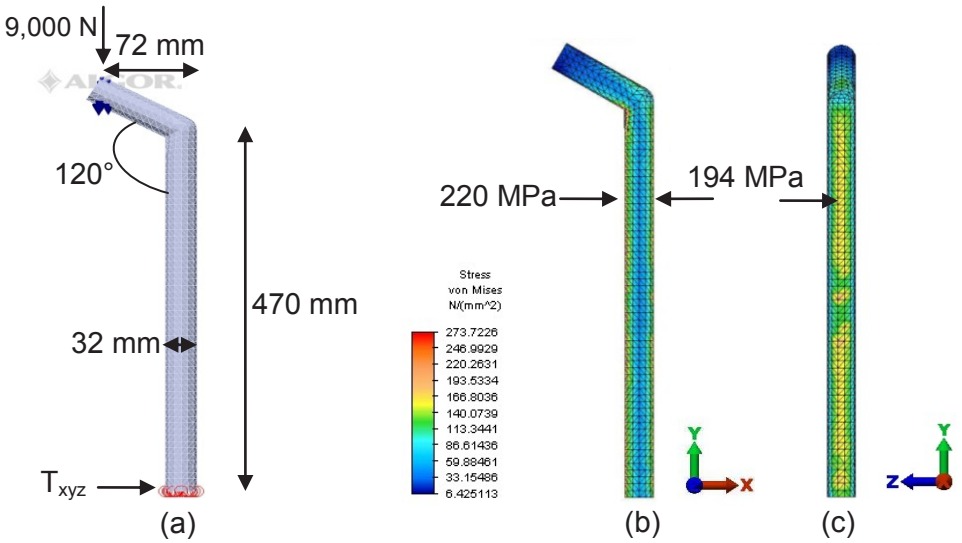

Figure 4.2. FEA pipe model. (a) Model definition, (b) Stress yy, anterior view, (c) Stress yy, lateral view

Theoretical calculations were also performed to validate the FEA model. The area, *A*, and mass moment of inertia, *I*, were calculated according to equations (4.9) and (4.10).

$$A = \frac{\pi \left({d_o}^2 - {d_i}^2 \right)}{4} \tag{4.9}$$

$$I = \frac{\pi \left({d_o}^4 - {d_i}^4 \right)}{64} \tag{4.10}$$

where d_o and d_i represented the outside and inside diameters of the pipe, respectively. These values were used to calculate the axial and bending stresses of the pipe. The axial stress of the pipe was calculated from equation (4.11), where the applied vertical load, *P*, and cross sectional area, *A*, from equation (4.9) determined the longitudinal stresses. This stress was compressive on both the compressive and tensile sides of the pipe model.

$$\sigma_{axial} = \frac{P}{A} \tag{4.11}$$

$$\sigma_{bending} = \frac{My}{I} \tag{4.12}$$

The bending stresses were determined from equation (4.12), where *M* was the bending moment, *y* was the distance from the neutral axis to the extreme fibers, and *I* was determined from equation (4.10). The bending stress was in compression on the compressive side and in tension on the tensile side of the pipe. The axial stress magnitude was calculated to be 13.4 MPa and the bending stress magnitude was 207 MPa. These results correlated to the FEA stresses of 220 MPa on the compressive side and 194 MPa on the tensile side with a percent difference of 6.4%.

4.3 Composite Bone Solid Model

A 3D solid model of the Sawbones fourth generation large, left femur (model 3406, Pacific Research Laboratories, Inc.) was obtained from the manufacturer. Models were developed in SolidWorks Education Edition 2010 to represent each treatment group by augmenting the model with solid models of the fixation hardware provided by Synthes. In most instances, the inserted hardware geometry was subtracted from the base femoral model. The exception for ROH was in the IHSP treatment groups wherein the TFN and distal cortex screw remained in the model. Solid models were then imported into Algor and assigned material properties, element type and definition, loads, and boundary conditions. The details for each model development follow.

Control

The solid model contained three imported parts, a cortical bone exterior, a cancellous bone proximal interior, and a cancellous bone distal interior. In order to simulate a one-legged stance from the compression testing previously described, the model was placed at a 10° adduction angle with respect to the global vertical y-axis, Figure 4.3(a). The manufacturer's CAD model lacked the cross pin holes that exist on the femurs as a result of the manufacturing process, Figures 4.3(b) and 4.3(c). As such, a 3.175 mm diameter hole was extruded through the neck of the femur. The angle of the extrusion was compared to the angle observed in fluoroscopic images. The measured angle for the cross pin canal was 60° from a line that was generated at the top of the greater trochanter and followed midline through the shaft, Figure 4.3(c).

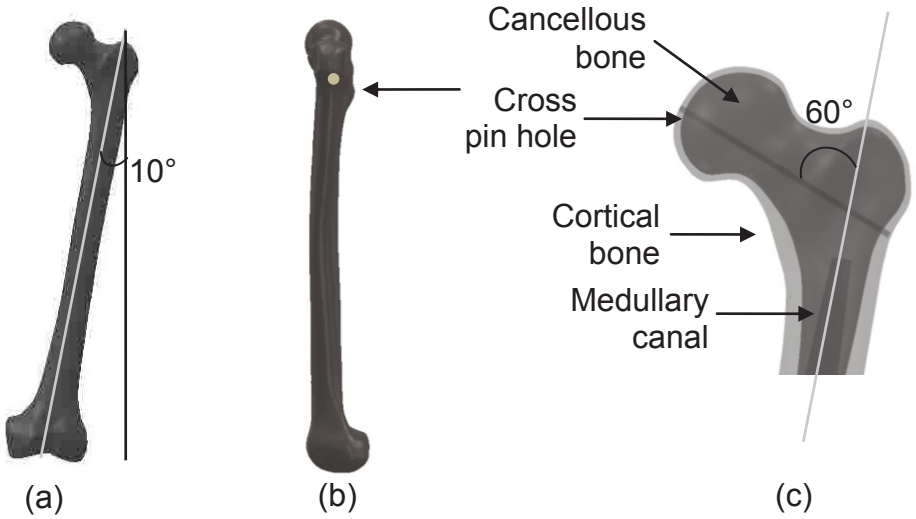

Figure 4.3. Control solid model. (a) Anterior view with 10° adduction angle, (b) Lateral view (c) Cross pin hole location in cross section

The top grip for the Instron was also modeled in SolidWorks, Figure 4.4(a). One of the problems in developing the virtual assembly of bone and top grip was the mating between the irregularly shaped femoral head and inside cone-shaped surface of the grip. The geometry of the femoral head was not uniform in any direction; therefore, only point contacts were possible between the two surfaces. To solve the problem, a sphere, slightly larger than the largest diameter of the head was drawn then attached over the head, Figure 4.4(b). A cavity was cut out from the sphere, based on the shape of the head. The new assembly successfully mated to the interior of the grip, creating a line of contact around the top of the new spherical head, Figure 4.4(c). This spherical head model served as the basis for all subsequent treatment group models.

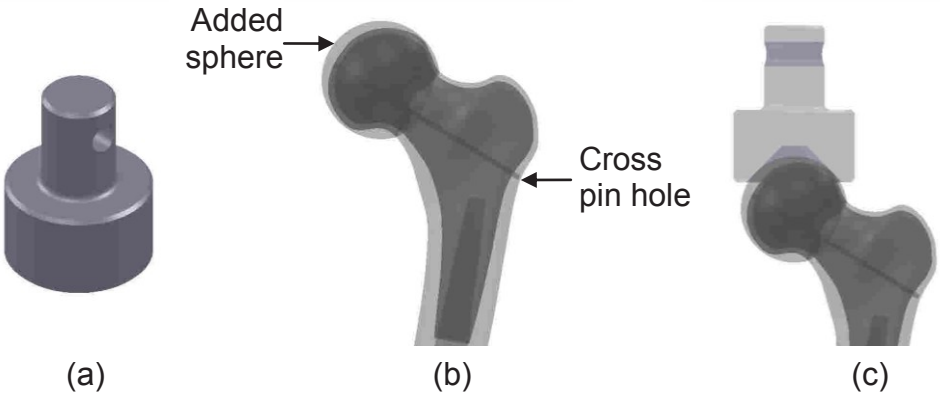

Figure 4.4. Model adjustment for Instron grip. (a) Top grip, (b) Addition of sphere (c) Full assembly in cross section

Cannulated Screws

Two cannulated screw models, 95 mm and 100 mm, obtained from Synthes were inserted into the spherical head femur model, Figures 4.5(a) and 4.5(b). The screws were placed in the composite bone solid model, according to

the locations shown the fluoroscopic images, Figures 2.12(b) and 2.12(c). The screw geometries were inserted as parts into the spherical head femur, combined with the body of the femur, and then subtracted from the overall geometry. The residual holes on the lateral surface are pictured in Figure 4.5(c).

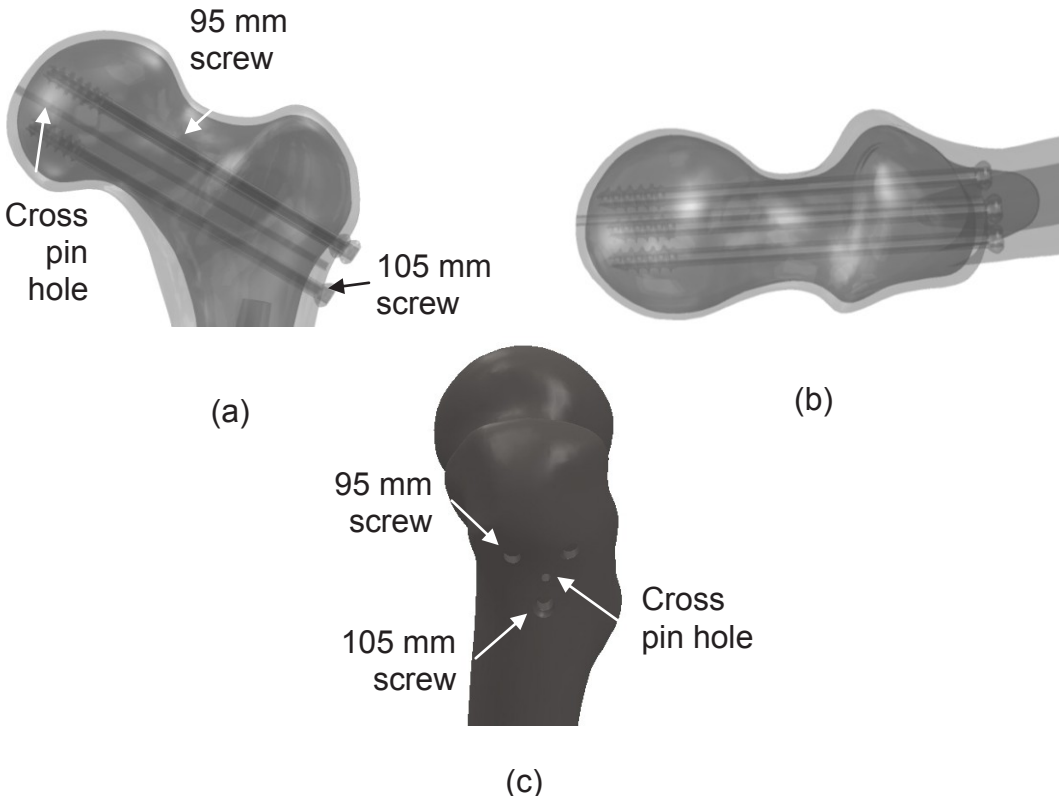

Figure 4.5. Cannulated screws model. (a) Anterior view, cross section, (b) Top view, cross section, (c) Residual holes, lateral view

Cannulated Screws, Cement-Filled

The procedure for augmentation of the spherical head cement-filled model was identical to the previously described cannulated screws model. To minimize potential problems with meshing and surface contacts in the FEA model, the cement filled holes were modeled as straight cylinders with analogous diameters and lengths to the original screws.

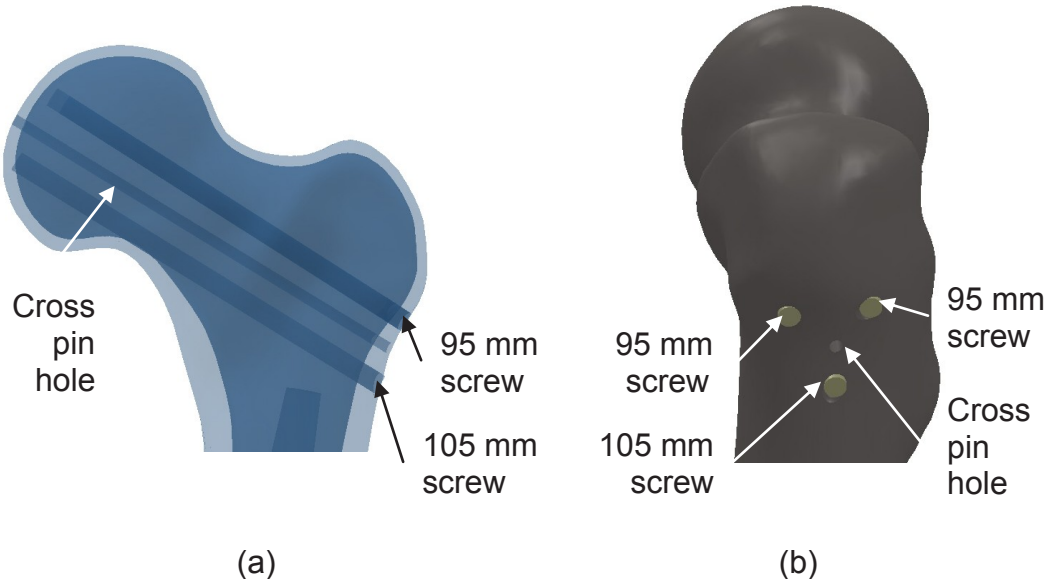

Figure 4.6. CSC model. (a) Cement insertion, cross section, (b) Cement insertion, lateral view

DHS

The DHS solid models were prepared with one-85 mm lag screw, two-4.5 mm cortex screws, and DHS plate solid models of which were obtained from Synthes, Figure 4.7(a). The fixation hardware was placed analogous to the locations on the prepared composite samples, correlating the locations to the fluoroscopic images, Figures 2.13(a). As previously done with the cannulated screws, the screw and plate geometries were inserted as parts into the spherical head femur, combined with the body of the femur, and then subtracted from the overall geometry. In each case, the cross pin hole was captured by the insertion and removal of the lag screw. The residual holes on the lateral surface are pictured in Figure 4.7(b).

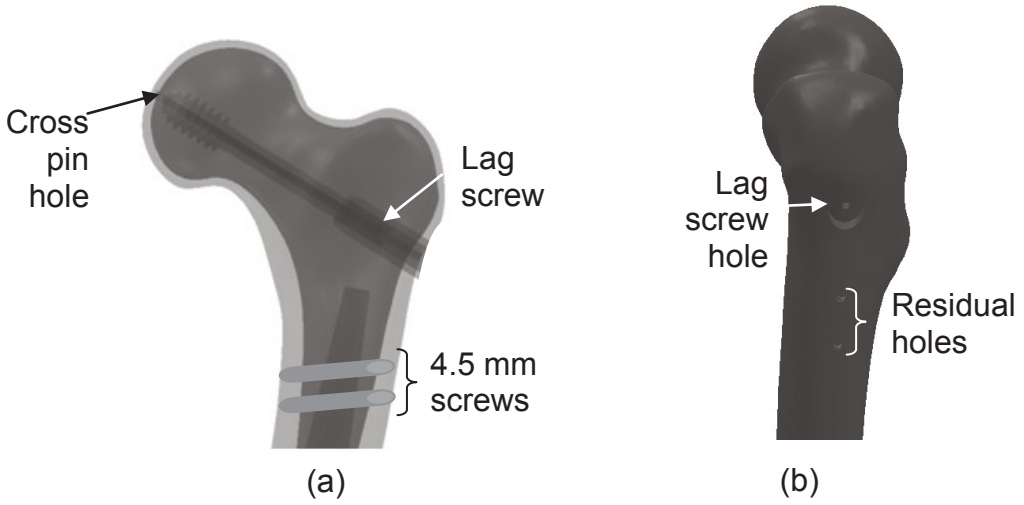

Figure 4.7. DHS model. (a) DHS inserted hardware, cross section, (b) Residual holes, lateral view

DHS, Cement-Filled

Cement augmentation of the DHS spherical head model was performed similarly to the previously described cannulated screws, cement-filled model. The residual holes were modeled as straight cylinders, maintaining the same diameters and length of the original screws, Figures 4.8(a) and 4.8(b).

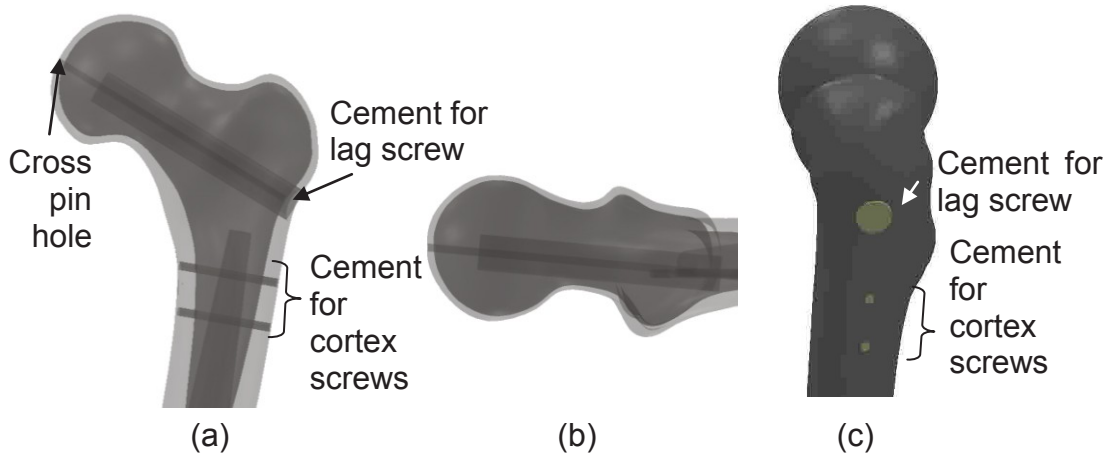

Figure 4.8. DHSC model. (a) Cement application, cross section, (b) Cement application, top view, (c) Cement application, lateral view

IHS

IHS solid models were prepared with CAD models of a lag screw, cortex screw, and a TFN, obtained from Synthes, Figure 4.9(a). Fluoroscopic images and treated composite bones were used to help determine the proper placement of the fixation hardware, Figure 2.15(b). Insertion of the CAD models followed the same format as previously discussed as well as the ROH from the solid model. Cross pin holes were captured by the insertion of the lag screw in all cases. The residual holes on the top and lateral surfaces are pictured in Figures 4.9(b) and 4.19(c).

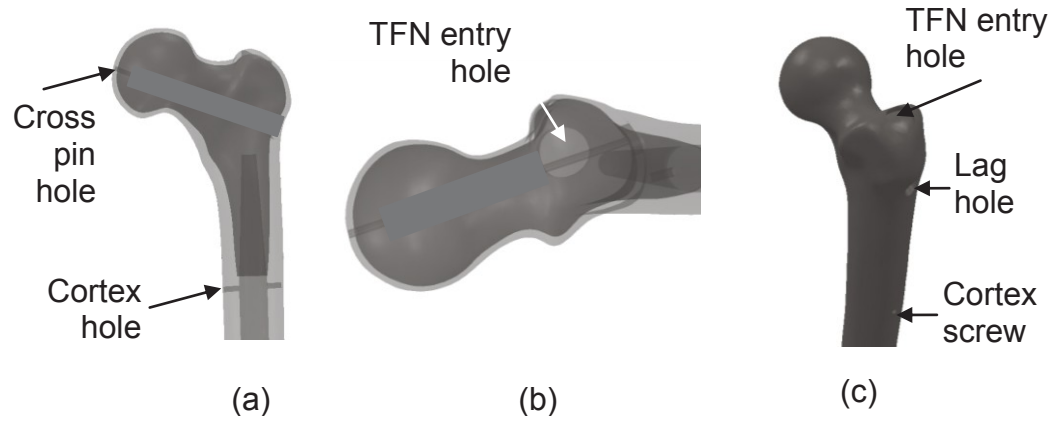

Figure 4.9. IHS model. (a) Cross section, (b) Top view, (c) Lateral view

IHS, Partial Removal

The model development for the IHS, partial removal model included the augmentation of the spherical head model with the lag screw, TFN and cortex screw and removal of only the lag screw, Figures 4.10(a) and 4.10(b). The process of inserting and subtracting the geometry was the same as done for the IHS model.

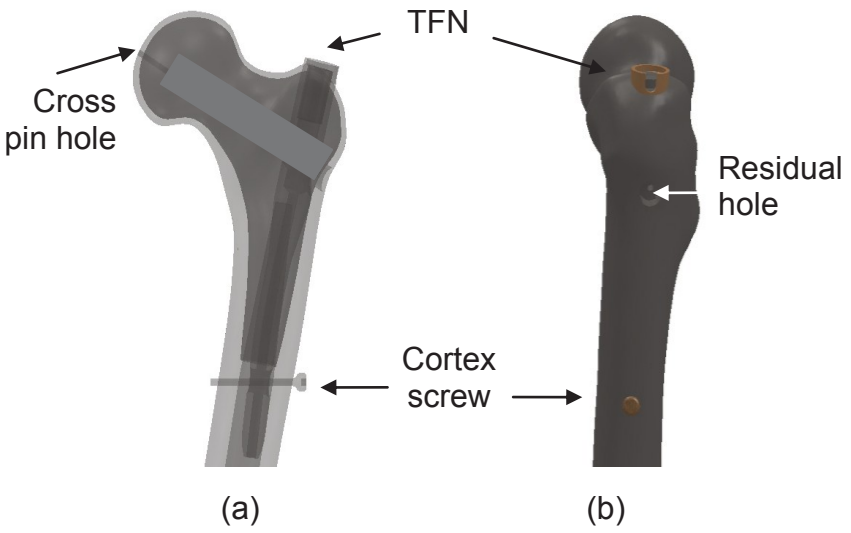

Figure 4.10. IHSP model. (a) Cross section, (b) Lateral view

4.4 Composite Bone Model Mesh

Once the SolidWorks models were complete, the assemblies were imported into the FEA preprocessor for descretization of the solid bodies into tetrahedral elements, known as model meshing. Due to some difficulties in meshing the cancellous portions of the model, a review of the literature regarding the impact of including or not including the material in FEA analyses was performed. Papini et al. (2007) found that the removal of the cancellous elements from analyses resulted in only a 1% difference in predicted values. Therefore, all cancellous bone elements were deactivated from the treatment groups for analysis.

The investigation of mesh size was limited by the computing capacity of the particular workstation. A few of the finer mesh sizes attempted for mesh convergence experienced a ‘time out’ and ceased the analysis prior to the full

loading of the specimen. However, mesh convergence as a function of displacement was completed to as fine a mesh necessary to ensure reliable results.

An initial concern occurred with the correlation of the FEA y-displacement values to the experimental values, resulting in displacements of less than half of those observed. The modulus values were adjusted from the manufacturer's material specifications in order to observe the same displacement in the FEA as was tabulated in the experimental data. Preliminary analyses were run with the full *E* value of 16,700 MPa, a three-quarters *E* value of 12,525 MPa, a half *E* value of 8,350 MPa, and a quarter *E* value of 4,175 MPa. Using an absolute edge length of 3 mm, isotropic material properties, and boundary conditions to be described in Section 4.6, the models were run and values for the displacement in the y-direction were recorded at a location on the femoral head that exhibited almost all vertical deflection. The gray shading represented a 1% scale factor of the displaced model, Figure 4.11. The quarter *E* deflection best correlated to the Instron crosshead vertical deflection of the control femurs that were run experimentally. Thus, the effective modulus of elasticity, E_{eff}, used in all the analyses was 4,175 MPa.

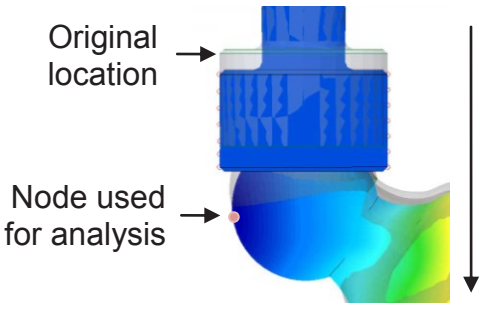

Vertical movement in y-direction	
Full *E*	1.83 mm
¾ *E*	2.51 mm
Half *E*	3.71 mm
¼ *E*	7.51 mm

Figure 4.11. Deflection of femoral head

Once the effective modulus was established, mesh convergence based on displacement continued in order to determine the optimal mesh size, Figure 4.12(a). This clearly shows that convergence began at approximately 3 mm absolute edge length. The computational time was also considered and compared with the number of elements, Figure 4.12(b). The computational time for the 2.5 mm absolute edge length element was significantly large relative to the amount of convergence obtained by the increase in elements. Therefore, all models were run at an absolute edge length of 3 mm.

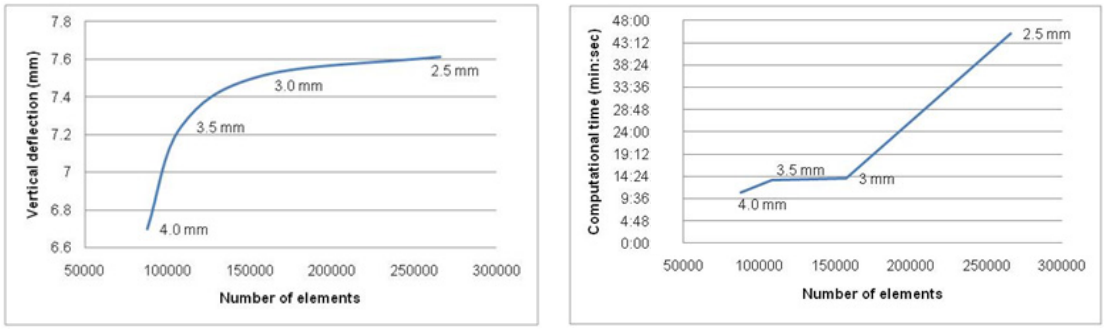

(a) (b)

Figure 4.12. Mesh convergence. (a) Convergence of y-deflection, (b) Computational time versus number of elements

Sample meshes for the cannulated screws, residual holes model and the DHS cement-filled model are shown in Figure 4.13(a) and 4.13(b).

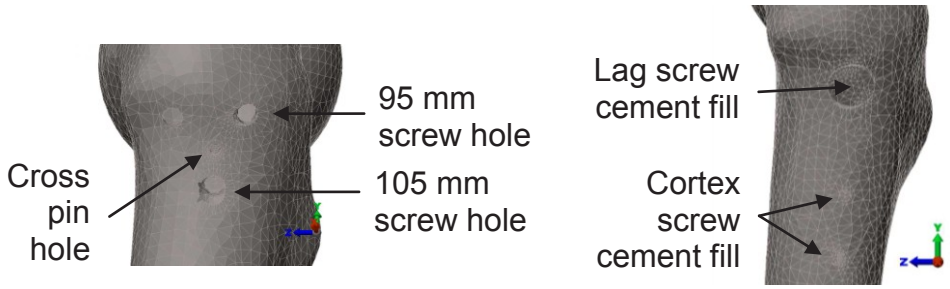

(a) (b)

Figure 4.13. Model mesh. (a) CS, (b) DHSC

4.5 Model Material Properties

For FEA analysis, the cancellous bone was deactivated, therefore material properties were not assigned to these two cancellous bone parts. The outside shell, the simulated cortical bone, was assigned a Poisson's ratio value, v = 0.26, and an effective modulus value, E_{eff} = 4,175 MPa (based on discussion in Section 4.4). The custom top grip for the Instron was made from A36 steel bar and assigned a Poisson's ratio value, v = 0.30, and modulus value, E = 200 MPa. The TFN and corresponding cortex screw were both made of Ti-6Al-7Nb and assigned the following values, v = 0.33 and E = 123 GPa. Finally, the Norian SRS cement was assigned values of v = 0.30 and E = 674 MPa (VanLieshout et al., 2011). In each case, the tetrahedral element was considered isotropic for the analyses.

4.6 Loading and Boundary Conditions

Following the mesh development and assignment of material properties, boundary conditions and loads were applied to each model. For all treatment groups, a mechanical event simulation-nonlinear analysis was employed and all models were analyzed with the same boundary conditions and loading scheme. To model the articulating surface between the condyles and the casting, one node was pinned, T_{xyz}, (translation in all three global directions) at the center of the bottom to prevent slippage from the casting and a selection of T_y (translation in the global y-direction) were placed in areas of greatest contact with the

casting, Figures 4.14(a) and 4.14(b). The top grip from the Instron was also constrained in the T_{xz}, (global x- and z- translation) thereby allowing only a global y- direction vertical movement as the load was applied to the femoral head, Figure 4.14(a). Finally, a vertical surface force of 9,000 N was applied to the top surface of the grip and was applied incrementally in twenty time steps, Figure 4.14(a).

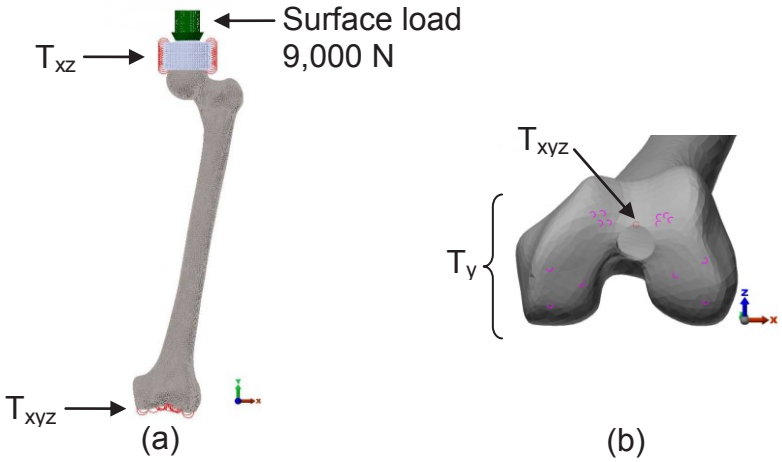

Figure 4.14. FEA model. (a) Load and boundary conditions, (b) Bottom boundary conditions

All parts of the bone, including fixation hardware and cement when applicable were created with bonded contact. However, since experimentally the femoral head could slide in the top grip of the Instron, the next step in the model development was to investigate surface-to-surface contact between these two surfaces. In order to achieve this interaction between the parts that likely occurs experimentally, surfaces in the solid model had to be identified as to which would line up as contact surfaces and parameters had to be adjusted so that there would be a sliding contact instead of penetration of the parts. A first attempt in

matching the surfaces resulted in an unsolvable model and subsequent tries led to penetration of one of the surfaces into the other, Figures 4.15(a) and 4.15(b) illustrate the deformation early in the loading cycle (step two of twenty) at a 1% scale factor and a 5% scale factor of the displaced model. To simplify the model, it was decided to bond the surfaces between the femoral head and the top grip. This made for a stable model. In addition, the general movement of the femur still correlated with what was found experimentally and with the bonded contact from the FEA, however, a significant amount of work is still needed to optimize this portion of the model.

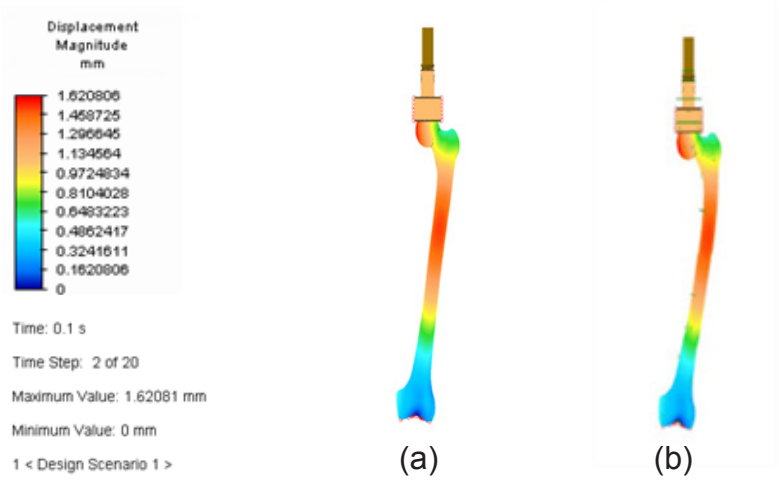

Figure 4.15. Surface contact model. (a) 1% scale factor of displaced model, (b) 5% scale factor of displaced model

4.7 Local Axis Development

In order to be able to compare the strains obtained from the linear gages in the experimental set up to the FEA results, a local axis had to be created. The strain gages, by design, only 'feel' the longitudinal strains and the model of the

femur in the FEA was set at an angle of 10° adduction, therefore a coordinate transformation had to be performed in order to obtain the proper strain values from the FEA.

To verify that the proper coordinate transformation had occurred, a simplified beam model was developed. The beam had a uniform 1 in by 1 in cross section and a length of 12 in, Figure 4.16(a). One end of the beam was fixed, while a vertical load of 5000 lbs causing bending in the cantilever beam was applied at the opposing end. The beam was rotated 10° off of the global x-axis. AISI 4130 steel was chosen for the material, E = $30x10^6$ psi. A local coordinate axis was chosen along the bottom edge of the beam, allowing the software to calculate the transformation. The FEA calculated local stress, σ_x, was 193.3 psi and the local strain, ε_x, was 6.442 in/in. Stress and strain values were

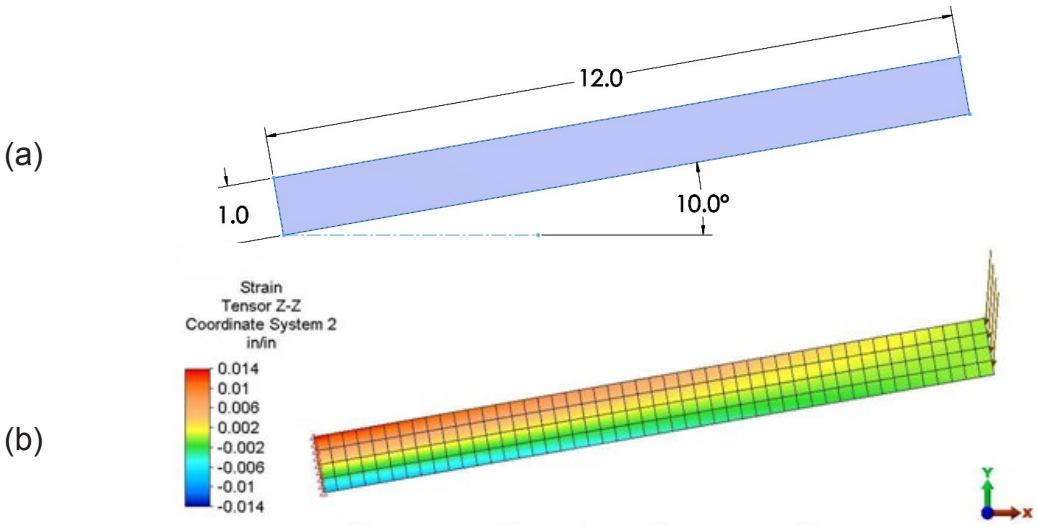

Figure 4.16. Local axis validation. (a) Beam model, (b) Strain tensor zz

found along the top edge of the beam, Figure 4.16(b). The global stress values for σ_x, σ_y, and τ_{xy} were found to be 187.7 psi, 5.6 psi, and 32.5 psi, respectively. Likewise, global strain values ε_x, ε_y, and γ_{xy} were found to be 6.199 in/in, -1.698 in/in, and 1.409 in/in, respectively.

Theoretical calculations were also performed to verify the local axis values obtained from the FEA were representative of an appropriate axis transformation. The 2D axis transformation was executed using equations (4.12) and (4.13), for both stress and strain respectively, where θ is the angle of rotation.

$$\sigma'_x = \sigma_x * (\cos\theta)^2 + \sigma_x * (\sin\theta)^2 + 2 * \tau_{xy} * (\sin\theta\cos\theta) \quad (4.12)$$

$$\varepsilon'_x = \varepsilon_x * (\cos\theta)^2 + \varepsilon_x * (\sin\theta)^2 + 2 * \gamma_{xy} * (\sin\theta\cos\theta) \quad (4.13)$$

The results from the theoretical calculations revealed a stress, σ_x, of 193.3 psi and a strain, ε_x, of 6.443 in/in. The results of the theoretical calculation were well correlated with the FEA, and as such determined that the interactive local coordinate axis application in the software was an appropriate method to help obtain the proper strain values.

CHAPTER 5

COMPUTATIONAL RESULTS

Finite element analysis was performed on each treatment group model, control, CS, CSC, DHS, DHSC, IHS, and IHSP and evaluated for the stresses and strains at particular regions of interest (ROI). In addition, regions were identified wherein areas of high stress occurred, sometimes in correlation with the physical failure of the bone and other times not. Finally, stresses were investigated at the stress risers created by the removal of hardware. As a reminder, the E_{eff} value for each of these tests was set at 4,175 MPa in order to obtain an overall vertical deflection that matched the experimental data, and all results were from bonded contact between all finite element bodies, including the spherical head and Instron top grip. Finally, all reported values were from the average load at failure, as determined by the experimental tests.

5.1 Composite Bone FEA Results

The composite model was evaluated for von Mises precision, the maximum von Mises stress location, von Mises stress at the location of each of the five linear strain gages, von Mises stress at the rosette, and strains in the local longitudinal direction at the locations of each of the linear strain gages. The location number corresponds with the strain gage number. Each model was

virtually disassembled to uncover any hidden stresses underneath mated parts. For each strain reading, the local coordinate axis was applied to the model and strains were recorded in the bone's longitudinal direction. To determine the appropriate load step at failure, the mean load at break was calculated from the Instron data. That value was taken as a percentage of the applied vertical load, 9,000 N. The percentage calculated was then applied to the twenty load steps. Thus, the failure load steps considered for each treatment group were as follows: control-load step 18; CS-load step 17; CSC-load step 16; DHS-load step 14; DHSC-load step13; IHS-load step12; and IHSP-load step 14. Detailed results for each model follows.

5.1.1 Von Mises Precision

Von Mises precision was evaluated for the whole bone, then more closely in the femoral neck, Figure 5.1. This plot is another tool to verify that the mesh used is adequate for analysis of the part. Values of less than 0.1 are preferred and keen attention should be paid to not only the precision value, but its location. The von Mises precision plots for each test model can be found in Figure 5.1. In each model, the largest von Mises precision values were under 0.19, Table 5.1. The highest values for the region are represented by a pink dot on the neck of each femur model. Qualitatively, the DHS model exhibited the widest spread of its highest value, but even so, the precision is still acceptable.

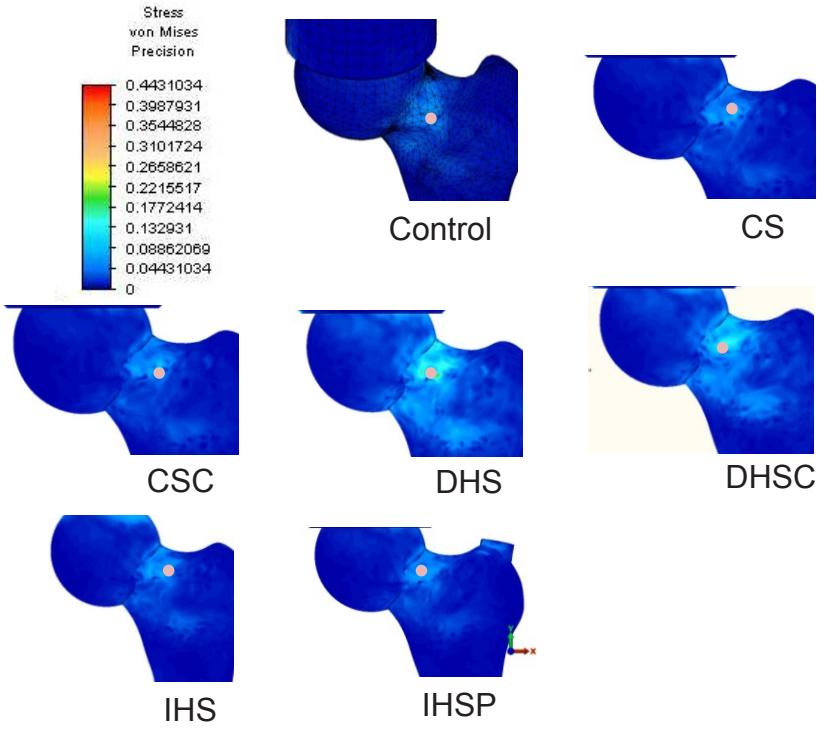

Figure 5.1. Von Mises precision

The largest values for von Mises precision were located in the femoral neck and were reported in Table 5.1.

Table 5.1. Von Mises precision

Treatment	von Mises Precision
Control	0.116
CS	0.111
CSC	0.193
DHS	0.178
DHSC	0.099
IHS	0.079
IHSP	0.080

5.1.2 Axial Deflection

The deformed shape, representative of a 1% scale factor of a displaced model, deflected as expected and is shown in Figure 5.2. The gray, transparent mesh is the initial, unloaded condition. The local axis is shown on the figure in the zz-direction.

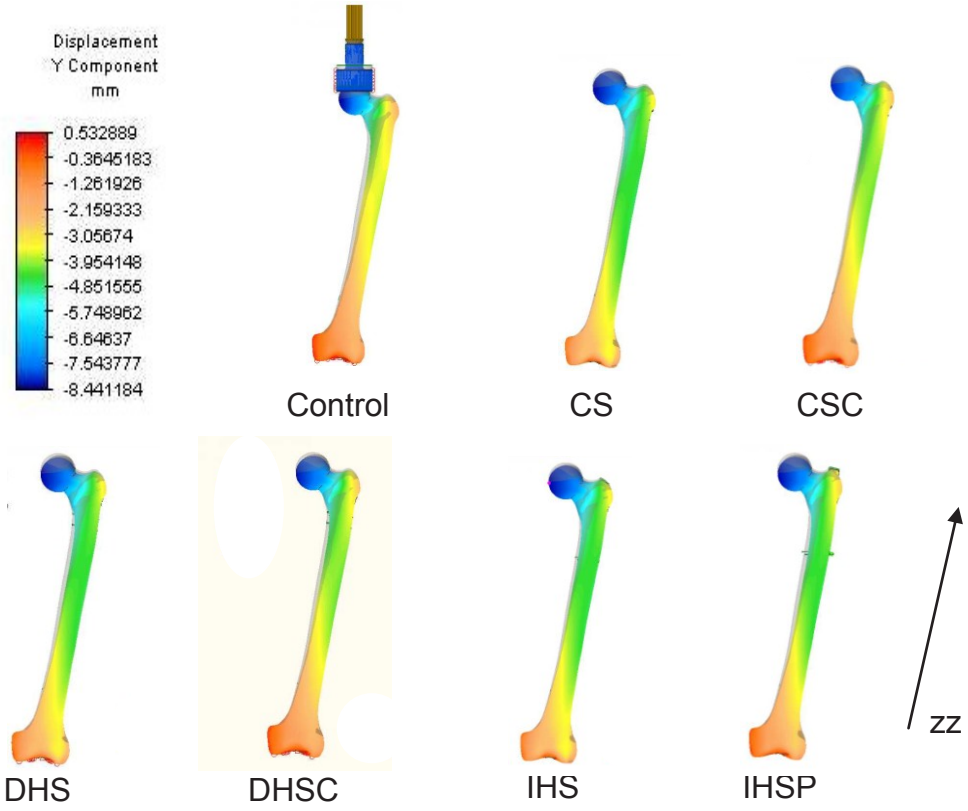

Figure 5.2. Axial deflection

5.1.3 Von Mises Stress

The highest region of stress was located in the neck of the femur at the interface between the sphere and the bone, Figure, 5.3. The graduation of the stresses across this region is important to note as well as recorded value.

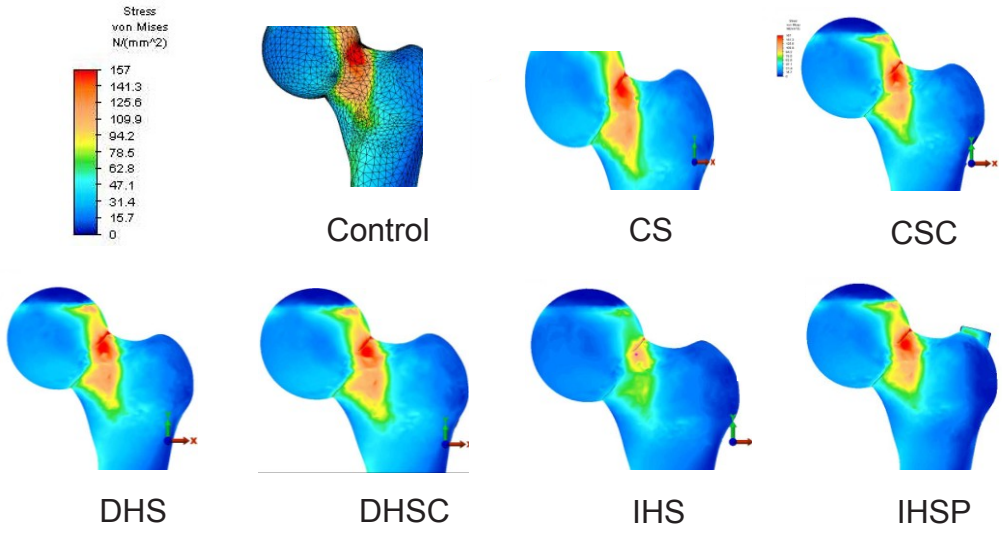

Figure 5.3. Maximum von Mises stress

The Instron top grip holder was removed to reveal the extent of the stresses at the interface of the spherical head and holder, Figure 5.4. In the control model, two small regions of high stress were uncovered at the interface on the side closest to the neck.

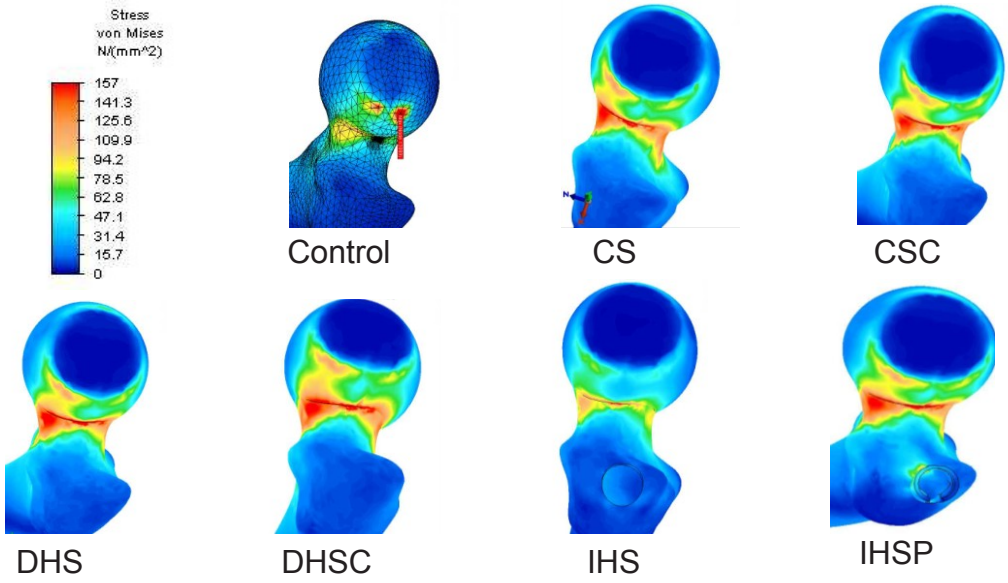

Figure 5.4. Von Mises stress at holder

5.1.4 Stress at ROH

Regions surrounding the CS residual holes due to the ROH were analyzed. The plot range was adjusted to reflect a scale of 0-30 MPa into order to note any regions that would be prone to high stress, especially in the region of the residual holes. In the cannulated screw model, top right and bottom center residual screw holes showed sites of high stress with the bottom screw hole exhibiting von Mises stress of 29.9 MPa, Figure 5.5. Stresses were also higher at the border of the cross pin hole ranging from 30.1 to 32.0 MPa. The largest stresses at the 95 mm screw holes were between 22.2 and 23.4 MPa.

An investigation of the regions surrounding the DHS residual holes, showed large stresses at the anterior and posterior sides of the hole left by the lag screw, Figure 5.5. Observed von Mises stresses in this region were as high as 25.2 and 29.6 MPa, respectively. Sites of high stress also occurred at the edges of the cortex screw residual screw holes, ranging from 22.6 MPa at the proximal cortex screw and 25.3 MPa at the distal cortex screw.

A closer look at the regions surrounding the DHSC cement-filled holes revealed a decrease in von Mises stresses to the side of the lag screw hole (21.7 MPa) and also surrounding the cortex screw holes. Stresses in that region ranged from 16.3 to 19.9 MPa with the distal cortex screw still exhibiting the largest stress values along the edge of the hole.

In the case of the IHS screw holes, the largest stresses were located on the sides of the lag screw exhibiting values ranging from 29.8 to 30.7 MPa. The

distal locking screw hole had a maximum stress of 19.2 MPa, and finally the entry hole of the TFN had a maximum stress of 22.6 MPa.

The IHSP model exhibited the least stresses on the surface in the location of the stress risers with a maximum stress of 14.2 MPa at the lag screw hole and 16.1 MPa at the distal locking screw.

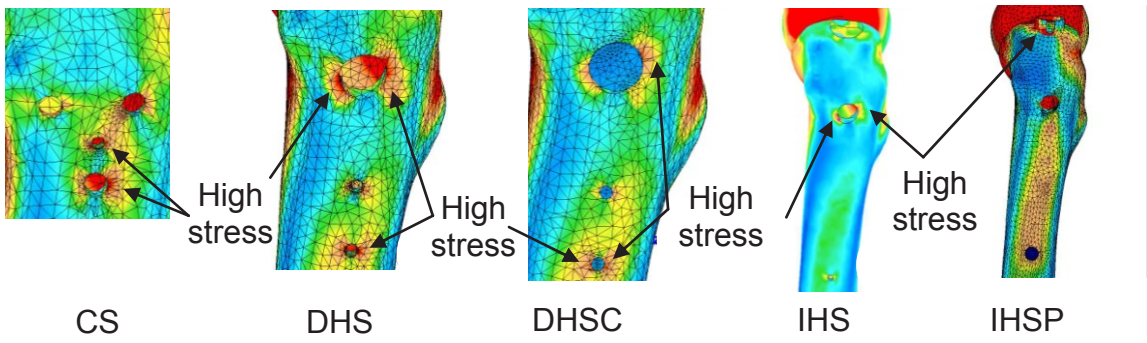

Figure 5.5. Von Mises stress at ROH

Von Mises stresses were also recorded at the locations of each strain gage on the lateral aspect of the shaft, Table 5.2.

Table 5.2. FEA von Mises stress results

	Location 1	Location 2	Location 3	Location 4	Location 5
Control (MPa)	13.1	16.0	18.7	18.1	9.88
CS (MPa)	10.9	13.3	12.0	15.2	8.77
CSC (MPa)	8.99	10.4	18.7	15.8	8.74
DHS (MPa)	9.67	17.4	12.9	11.8	5.01
DHSC (MPa)	6.90	10.3	13.5	9.75	6.97
IHS (MPa)	10.5	12.2	12.7	9.81	5.06
IHSP (MPa)	4.42	4.86	16.2	11.3	6.46

5.1.5 Strain

Lastly, strains were recorded in the local zz-direction along the lateral shaft at intervals analogous to the locations of the linear strain gages, Figure 5.6. The images in Figure 5.6 illustrate both the strain variations in the different treatment groups along the lateral shaft, but also show the variations on the anterior surface.

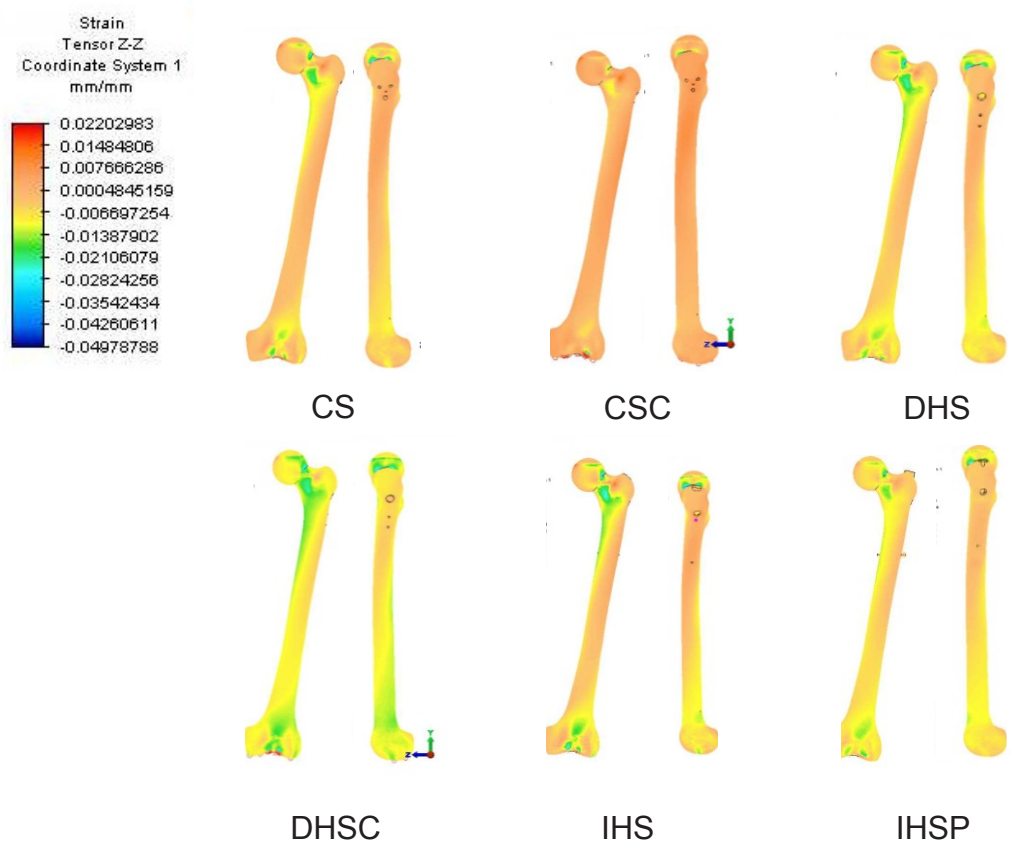

Figure 5.6 Longitudinal strain

The recorded strain values for each strain gage location are listed in Table 5.3.

Table 5.3. FEA strain results

	Location 1	Location 2	Location 3	Location 4	Location 5
Control (mm/mm)	$3.26E^{-3}$	$4.41E^{-3}$	$4.73E^{-3}$	$4.72E^{-3}$	$2.53E^{-3}$
CS (mm/mm)	$2.05E^{-3}$	$3.41E^{-3}$	$4.37E^{-3}$	$4.03E^{-3}$	$2.29E^{-3}$
CSC (mm/mm)	$1.66E^{-3}$	$2.71E^{-3}$	$4.75E^{-3}$	$4.20E^{-3}$	$2.27E^{-3}$
DHS (mm/mm)	$1.17E^{-3}$	$4.54E^{-3}$	$3.28E^{-3}$	$3.10E^{-3}$	$1.27E^{-3}$
DHSC (mm/mm)	$1.02E^{-3}$	$2.40E^{-3}$	$3.37E^{-3}$	$2.49E^{-3}$	$1.77E^{-3}$
IHS (mm/mm)	$2.12E^{-3}$	$3.17E^{-3}$	$3.25E^{-3}$	$2.60E^{-3}$	$1.36E^{-3}$
IHSP (mm/mm)	$1.07E^{-3}$	$1.38E^{-3}$	$4.18E^{-3}$	$2.66E^{-3}$	$1.73E^{-3}$

5.2 FEA Strain Profile

A strain profile was generated based on location of the gage on the bone, similar to those created with the experimental data. As described previously, the locations (1, 2, …5) refer to the distance from the top of the femur. Locations one and two correlate with the 50 mm distance, location three with the 105 mm distance, location four with the 145 mm distance and locations five with the 185 mm distance, Figure 5.7.

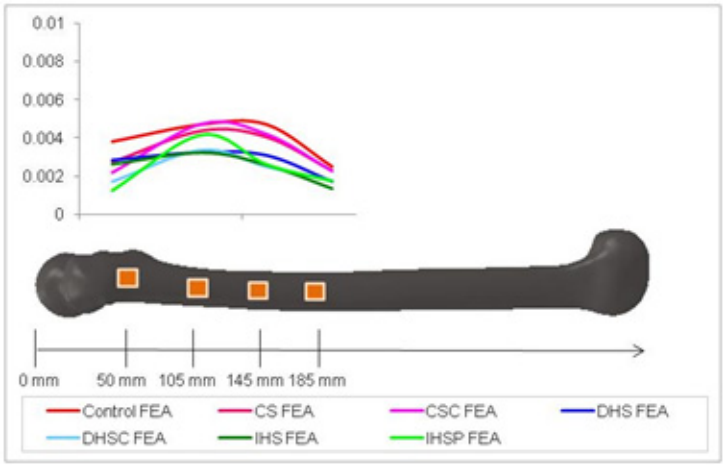

Figure 5.7. FEA strain profile

CHAPTER 6

DISCUSSION

Once the experimental and computer modeling data was collected and evaluated, comparisons could be made between the experimental and computational approaches as well as with findings from literature.

6.1 Experimental vs. Literature

The aim of the experimental portion of the study was to create a simplified testing model of the whole femur and evaluate the response of the composite bone to a compressive load. This was done by axial testing to failure, strain gage application and data collection, and optical elastography. Data compiled from the biomechanical testing was then used to help validate a simplified FEA model.

Direct comparison of the results to literature was difficult because of the high degree of variation in methodologies. This study is the only known investigation to include a more anatomically correct distal articulating surface, and extracted data from mechanical testing, strain gages, FEA, and optical elastography all in the same study.

Beginning with the base femoral model, only the bone was considered, not soft tissues. It has been shown that muscle activity has a major influence on the internal loading of the femur (Duda et al., 1997). Percent errors of up to 10% in

the proximal region can occur if as little as two muscle groups, abductors and vasti, are included. Therefore, it is expected that any results from this research would serve only to identify potential trends and not determine or predict values that occur *in vivo*. The authors found that internally, the proximal and distal ends of the femur show the highest axial and shear forces and movement toward the diaphysis yields reduced internal loads. This loading scenario is due to the muscle loading across the femur. Additionally, the bending moments are minimal compared to a study that does not consider any muscle activity. Here the medial cortex exhibits higher compression than the lateral surface across the full gait cycle. The acting load within the cortex is axial compression and bending moments are alternating and not constantly oriented in one direction. Considering these findings by Duda et al. (1997), it would be expected that in this study a larger magnitude of bending moments would be observed by the femurs. Furthermore, work performed by Garden (1961) showed that if a femur were mounted vertically (condyles in a horizontal plane), with an applied vertical compressive load, the bone, due to its structural geometry, would tend to rotate medially, thereby introducing an element of torsion.

6.1.1 Clinical Bone Failure

Some treatment groups failed consistently, such as the DHS and DHSC groups, and some were inconsistent failures, such as those in the CS and CSC groups. The control group resulted in two Pauwel's Type III fractures and one high subtrochanteric fracture. The Pauwel's fractures are indicative of a high

energy failure in a fully healthy bone, and occur due to shearing at the femoral neck. Sample one, did not fail in this manner, but rather failed through the cross pin hole which was a stress riser on the lateral surface. This particular sample however, had been tested through an unknown deflection without failure and then run a second time to failure, and thus was considered compromised.

The CS and CSC groups combined led to a total of three Pauwel's Type III fractures, two basicervical fractures, and one subtrochanteric fracture. A few anomalies were discovered within this group. Two of the samples, numbers eight and nine failed at less than half the mean load at break leading to questions about the effect of material versus the particular augmentation. The bones were manufactured on a separate date from the other bones obtained for the study, begging the question, could a batch problem have contributed to the failure. Internal voids can occur within the epoxy matrix of the cortical bone leading to undetectable internal stress risers that could have played a role in the failure at a location other than in the neck. For future testing, it would be beneficial to have some means of verifying the integrity of the material internally prior to testing, such as X-ray or CT. Another concern identified was the inconsistency of the screw placements within the femoral neck. Samples five, seven, eight, and nine exhibited some intrusion of the initial drilling into the cortical layer, and in the case of sample five, an obvious stress riser could be seen from the surface, Figure 3.5. The weakening of the cortical layer by defects related to the augmentation process must be considered as contributors to the ultimate failure of the specimens.

The DHS and DHSC groups all failed as subtrochanteric fractures with five of the six breaking through the distal cortex screw hole. The remaining femur failed through the proximal hole. In the study by Strauss et al, (2007), the researchers evaluated DHS ROH cadaveric femurs augmented with calcium phosphate cement. The resulting fractures from that study included ten neck fractures, three subcapital neck fractures and three basicervical fractures. An inability to correlate with the type of failure could be attributed to the methodology and the fact that cadaver bones exhibit high variability not seen in the composite models. The fact that all six femurs failed with the same type of fracture, point toward experimental reproducibility.

Finally, in the IHS and IHSP groups, the failures resulted in two subtrochanteric fractures and four intertrochanteric fractures. Sample nineteen was another femur that failed far below the mean load at failure. Again, no obvious defects were found that would lead to early failure. Miller et al, (1993) tested cadaveric femora for the effect of entry hole size from intramedullary nails on bone strength. Control femurs failed by oblique subcapital fractures (analogous to Pauwel's) and all treated femurs, regardless of hole size or placement failed by basicervical fractures through the entry hole of the nail. Again, a direct comparison cannot be made due the inconsistencies of the cadaver geometry and material properties.

The effect of the cement to the residual holes in the CSC group cannot be determined by the experimental results. Two of the three samples, as mentioned previously, failed at such low loads comparatively, that they were excluded from

analysis, leaving only one CSC cement-filled femur. That femur, sample seven, failed at a load of 7,196 N and the mean of the CS failures was 7,447 N, too insignificant of a difference to make any analysis based on one femur.

In the case of the cement-filled DHS femurs, there was a small decrease in the average load at failure; 6,306 N for the DHS group versus 6,044 N for the DHSC group. This seems counterintuitive as one would expect the filled-hole samples to recover strength and thus fail at a higher load than those left with empty hole stress risers. As stated before, the sample size was not really large enough to be able to draw convincing conclusions, rather only to point to potential trends.

The load at failure graphs indicated a trend of decreasing fracture load, which is inversely proportional to the amount of simulated bone material removed from the femurs. The cannulated screws are a long thin geometry compared to the IHS hardware that consists of a larger diameter screw through the neck plus the TFN that runs the length of the proximal femur. A preliminary trend, therefore, could relate volume of bone material lost to its mechanical performance. The control group, as expected, failed at the highest loads while the IHS group failed at the lowest loads. A trendline illustrated this relationship and contained an R^2 value of 0.81.

Load-deflection diagrams were created based on the information provided through the load cell and fed into the Bluehill 3 software package. An average load-deflection curve showed that all bones have the same constant of proportionality between load and deflection and thus, stress strain until reaching

about 4 mm compression; and then the groups diverged. However, the divergence is still not enough to consider significant non-linear material behavior.

6.1.2 Strain Gage Results

Strain profiles were created for each sample group, at four different time intervals, by comparing the recorded strains to the placement along the lateral surface of the femur, Figures 3.1(a)-3.1(d). The strains varied across the surface, achieving their maximum strains at gage 5, or 105 mm from the top of the femur. A qualitative correlation was found to the strain profiles reported by Duda et al (1997). The authors used twenty strain gages per model to best portray the strain fields on each side of the femur. Szivek and Gealer (1991) measured strains in the femoral neck (which this study did not consider) and proximal shaft. The location of lateral strain gage that the author's measured was 91 mm from the top of the femoral head, which would be close to the location of the strain gages one and two on the control femur in this study. The authors reported the average strain value for the six composite bones as $2.69E^{-3}$ mm/mm. The average recorded value (combining gages one and two) in this study at break was $3.52E^{-3}$ mm/mm. In the author's experimental set up, the distal end of the femur was potted and the loading frame also applied a tensile load to the trochanter region to account for some muscle action, which could account for the variation.

6.1.3 Optical Elastography

This is an emerging technology that certainly has a great deal of potential in non-invasive biomechanical testing. The elastograms showed areas of high strain compared to surrounding areas in a region near the known fracture path. The results presented are just the preliminary steps to determining and calibrating elastograms that can in turn be used to help validate FEA models. Additional work will need to be done in order to achieve a more accurate stress-strain curve for each of the models. This is work that is ongoing.

6.2 Computational vs. Literature

The model development presented in this study was for a fundamental model that focused exclusively on the bone, eliminating soft tissue affects and minimized computing time. The focus was to recreate the experimental set up. There were some challenges in the development of this model, especially in the modeling of the interface of the femoral head to the grip in the axial testing machine. Geometric inconsistencies in the femoral head did not allow for anything more than point contact to the inside surface of the top grip, as discussed in Chapter 4. Solving the mating problem with the addition of a spherical cap certainly introduced stress risers at the intersection of the sphere and body of the main part (cortical bone), Figures 5.1(c), 5.4(c), 5.7(c), 5.10(c), 5.13(c), 5.16(c), and 5.19(c). Constant errors occurred while attempting to modify these surfaces as a unit in SolidWorks. Future work to refine the model will require one to revisit this mating.

The surface contact between the sphere and the grip was another area of difficulty. Algor, the FEA package used, allows for the selection of point to surface or surface to surface contact with the ability to choose the amount of friction between the sliding of interest. In each of the trials attempted, analysis timed out and in some cases there was also penetration of a part into another part. Further investigation on the method of applying this feature will be the next important step toward basic model refinement.

Comparison of results to those reported in literature is also difficult due to the variation in model definition, loading scenarios, and the range of applied technologies to develop the FE model, e.g. CT-based modeling. Mahaisavariya et al (2006) modeled the augmented and ROH conditions of a trochanteric gamma nail (similar to the TFN used in this study). An important finding from the authors' work was that the femoral neck had a much higher strain and strain energy density than the entry point of the gamma nail, the region for the lag screw, and region for the distal cortex screw. This correlates with the findings in this study wherein all treatment groups exhibited the highest stresses in the neck region compared to any other location along the model. This statement would also mean that in ROH of this particular implant, the femoral neck would still be more likely to fail than at a subtrochanteric level where stress risers are left from the lag and cortex screws. In the experimental section of this study the IHS and IHSC fractures resulted in four intertrochanteric fractures, failing through the TFN entry hole, and two subtrochanteric fractures. None of the femurs failed through the femoral neck.

An interesting stress pattern observed in the FEA was the stresses around the line of contact between the spherical head and the inside surface of the top grip, Figures 6.1(a) and 6.1(b). On the experimental samples, especially in the control, CS, and CSC femurs, a distinct dark gray mark was found on the surface where the point of contact was made with the inner surface of the holder; see encircled locations on Figure 6.1(a). On the opposite side of the encircled marks are another set of marks with cracks emanating in both directions. The FEA model shows those areas as regions of higher von Mises stress, Figure 6.1(b). This indicates that the contact of the top grip *may* be a contributor to the fractures that began on the lateral-most side of the femoral head.

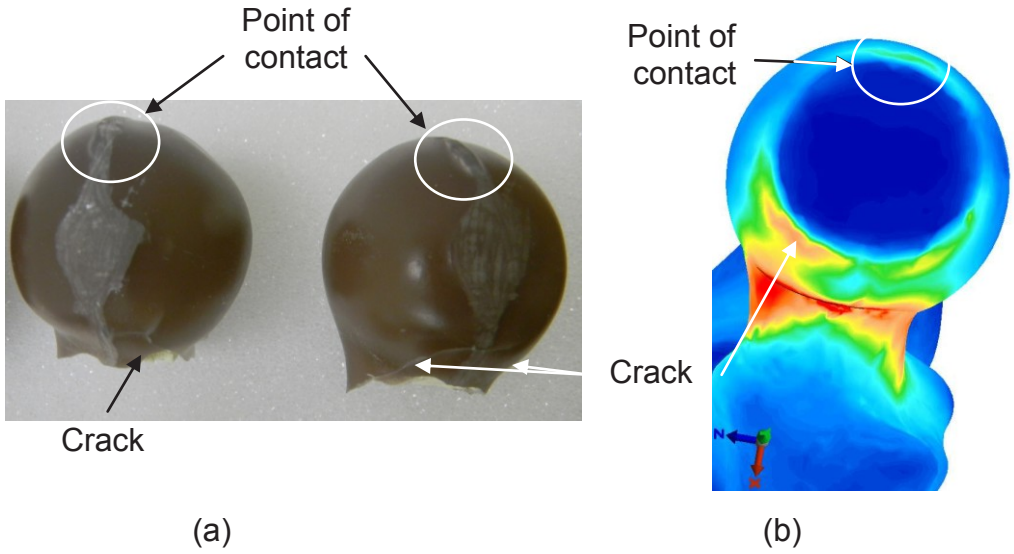

Figure 6.1. Femoral head comparison. (a) Experimental, (b) FEA

6.3 Computational vs. Experimental

The results of the experimental composite bones and the preliminary FEA model suggest a few potential trends that are worth further investigation with

refinement of the FEA model. First, the experimental strain profile of the lateral surface was generally correlated with curves presented in literature (Szivek & Gealer, 1991) and shown in the FEA, Figures 6.1(a) and 6.1(b).

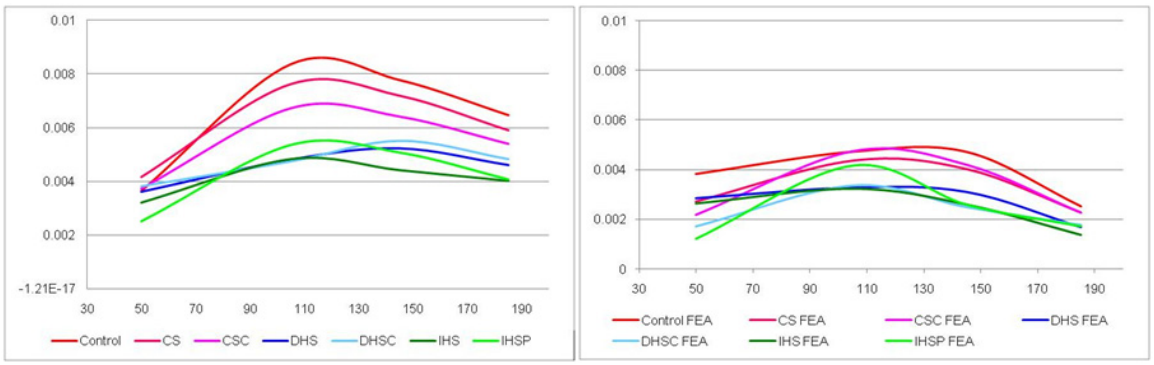

(a) (b)

Figure 6.2. Strain profile comparison. (a) Experimental, (b) FEA

Second, none of the FEA models predicted stress high enough to create any type of clinical fracture other than a Pauwel's fracture. It is possible that the augmentation process leaves larger stress risers around the holes, that are not picked by up by the modeling in the FEA. Therefore, any jagged edge or chip of the material could initiate a failure in a location other than the neck.

Finally, the elastic modulus provided by the manufacturer would not give the deflection in the FEA that was found experimentally. This certainly causes concern when a quarter of the modulus employed still does not provide correlated deflections. Most FEA studies focus on using the varying bone properties of the cortical and cancellous layers to develop the model.

6.4 Future Work

For future model developments, the addition of a more accurate physiological loading scenario would be necessary. In that instance, all loads imposed on the proximal femur would be included and then any testing through FEA would give a better approximation of the biomechanical response of the bone. In addition to adding appropriate muscle group forces, a look into methods where the density of the cancellous bone can be varied according to location within the proximal femur would better simulate the load transfer that occurs *in vivo*. Some of this work can be done by remodeling the base femur adding layers of material of representative densities, but it could also be performed by using CT-based modeling techniques often employed in biomedical analyses.

Once a validated model is designed, then further work can be done to investigate the effects of changing bone porosity on the implantation and removal of hardware.

REFERENCES

Alford, J. W., Bradley, M. P., Fadale, P. D., Crisco, J. J., Moore, D. C., & Ehrlich, M. G. (2007). Resorbable fillers reduce stress risers from empty screw holes. The *Journal of Trauma, 63*(3), 647-654.

Bartel, D. L., Davy, D. T., & Keaveny, T. M. (Eds.). (2006). *Orthopaedic biomechanics: Mechanics and design in musculoskeletal systems*. Upper Saddle River, N.J.: Pearson/Prentice Hall.

Bessho, M., Ohnishi, I., Matsuyama, J., Matsumoto, T., Imai, K., & Nakamura, K. (2007). Prediction of strength and strain of the proximal femur by a CT-based finite element method. *Journal of Biomechanics, 40*(8), 1745-1753.

Brown, R. M., Wheelwright, E. F., & Chalmers, J. (1993). Removal of metal implants after fracture surgery--indications and complications. *Journal of the Royal College of Surgeons of Edinburgh, 38*(2), 96-100.

Budynas, R. C. (1999). *Advanced strength and applied stress analysis* (Second ed.) McGraw-Hill.

Busam, M. L., Esther, R. J., & Obremskey, W. T. (2006). Hardware removal: Indications and expectations. *The Journal of the American Academy of Orthopaedic Surgeons, 14*(2), 113-120.

Chen, S. H., Yu, T. C., Chang, C. H., & Lu, Y. C. (2008). Biomechanical analysis of retrograde intramedullary nail fixation in distal femoral fractures. *The Knee, 15*(5), 384-389.

Chirodian, N., Arch, B., & Parker, M. J. (2005). Sliding hip screw fixation of trochanteric hip fractures: Outcome of 1024 procedures. *Injury, 36*(6), 793-800.

Collinge, C., Merk, B., & Lautenschlager, E. P. (2007). Mechanical evaluation of fracture fixation augmented with tricalcium phosphate bone cement in a porous osteoporotic cancellous bone model. *Journal of Orthopaedic Trauma, 21*(2), 124-128.

Cristofolini, L., Viceconti, M., Cappello, A., & Toni, A. (1996). Mechanical validation of whole bone composite femur models. *Journal of Biomechanics, 29*(4), 525-535.

Duda, G. N., Schneider, E., & Chao, E. Y. (1997). Internal forces and moments in the femur during walking. *Journal of Biomechanics, 30*(9), 933-941.

Egol, K. A., Kubiak, E. N., Fulkerson, E., Kummer, F. J., & Koval, K. J. (2004). Biomechanics of locked plates and screws. *Journal of Orthopaedic Trauma, 18*(8), 488-493.

Garden, R. S. (1961). The structure and function of the proximal end of the femur. *The Journal of Bone and Joint Surgery*, *43*(3), 576-589.

Gosling, T., Hufner, T., Hankemeier, S., Zelle, B. A., Muller-Heine, A., & Krettek, C. (2004). Femoral nail removal should be restricted in asymptomatic patients. *Clinical Orthopaedics and Related Research, (423)*(423), 222-226.

Greer, B., Wang, E., Jiang, Y. On the appropriateness of using the Standardized Femur for FEA in the proximal region. ASME, New York, BED-Vol. 42, Summer Bioengineering Conference, Big Sky, MT, 1999.

Haidukewych, G. J., & Berry, D. J. (2003). Hip arthroplasty for salvage of failed treatment of intertrochanteric hip fractures. *The Journal of Bone and Joint Surgery. American Volume, 85-A*(5), 899-904.

Hanson, B., van der Werken, C., & Stengel, D. (2008). Surgeons' beliefs and perceptions about removal of orthopaedic implants. *BMC Musculoskeletal Disorders, 9*, 73.

Hausmann, J. T. (2006). Sawbones in biomechanical settings-A review. *Osteosynthesis and Trauma Care, 14*(4), 259-264.

Heiner, A. D. (2008). Structural properties of fourth-generation composite femurs and tibias. *Journal of Biomechanics, 41*(15), 3282-3284.

Heiner, A. D., & Brown, T. D. (2001). Structural properties of a new design of composite replicate femurs and tibias. *Journal of Biomechanics, 34*(6), 773-781.

Iesaka, K., Kummer, F. J., & Di Cesare, P. E. (2005). Stress risers between two ipsilateral intramedullary stems: A finite-element and biomechanical analysis. *The Journal of Arthroplasty, 20*(3), 386-391.

Imura, S., & Hip Biomechanics Symposium, (Eds.). (1993). *Hip biomechanics*. Tokyo; New York: Springer-Verlag.

Jamil, W., Allami, M., Choudhury, M. Z., Mann, C., Bagga, T., & Roberts, A. (2008). Do orthopaedic surgeons need a policy on the removal of metalwork? A descriptive national survey of practicing surgeons in the United Kingdom. *Injury, 39*(3), 362-367.

Johnell, O., & Kanis, J. A. (2006). An estimate of the worldwide prevalence and disability associated with osteoporotic fractures. *Osteoporosis International: A Journal Established as Result of Cooperation between the European Foundation for Osteoporosis and the National Osteoporosis Foundation of the USA, 17*(12), 1726-1733.

Klotzbuecher, C. M., Ross, P. D., Landsman, P. B., Abbott, T. A., 3rd, & Berger, M. (2000). Patients with prior fractures have an increased risk of future fractures: A summary of the literature and statistical synthesis. *Journal of Bone and Mineral Research: The Official Journal of the American Society for Bone and Mineral Research, 15*(4), 721-739.

Koval, K. J., & Zuckerman, J. D. (Eds.). (2000). *Hip fractures: A practical guide to management*. New York: Springer.

Kukla, C., Pichl, W., Prokesch, R., Jacyniak, W., Heinze, G., Gatterer, R., et al. (2001). Femoral neck fracture after removal of the standard gamma interlocking nail: A cadaveric study to determine factors influencing the biomechanical properties of the proximal femur. *Journal of Biomechanics, 34*(12), 1519-1526.

Lenich, A., Fierlbeck, J., Al-Munajjed, A., Dendorfer, S., Mai, R., Fuchtmeier, B., et al. (2006). First clinical and biomechanical results of the trochanteric fixation nail (TFN). *Technology and Health Care: Official Journal of the European Society for Engineering and Medicine, 14*(4-5), 403-409.

LeVeau, B. F., & Williams, M. (Eds.). (1992). *Williams & Lissner's biomechanics of human motion* (3rd ed.). Philadelphia: W.B. Saunders Co.

Logan, D. L. (2001). *A first course in the finite element method using algor* (Second ed.). Pacific Grove, California: Brooks/Cole.

Lotz, J. “Hip fracture risk predictions by x-ray computed tomography,” Ph.D. Dissertation, Department of Mechanical Engineering, Massachusetts Institute of Technology, 1988.

Magaziner, J., Hawkes, W., Hebel, J. R., Zimmerman, S. I., Fox, K. M., Dolan, M., et al. (2000). Recovery from hip fracture in eight areas of function. *The Journals of Gerontology.Series A, Biological Sciences and Medical Sciences, 55*(9), M498-507.

Mahaisavariya, B., Sitthiseripratip, K., & Suwanprateeb, J. (2006). Finite element study of the proximal femur with retained trochanteric gamma nail and after removal of nail. *Injury, 37*(8), 778-785.

Marie, H., Zhang, Y., Heffner, J., Dorion, H.A., Fagan, D. L. (2010). Biomechanical and Elastographic analysis of Mesenchymal Stromal cell treated tissue following surgery. *Journal of Biomechanical Engineering*, *132*(7), 074503.

Miller, S. D., Burkart, B., Damson, E., Shrive, N., & Bray, R. C. (1993). The effect of the entry hole for an intramedullary nail on the strength of the proximal femur. *The Journal of Bone and Joint Surgery. British Volume, 75*(2), 202-206.

Minkowitz, R. B., Bhadsavle, S., Walsh, M., & Egol, K. A. (2007). Removal of painful orthopaedic implants after fracture union. *The Journal of Bone and Joint Surgery. American Volume, 89*(9), 1906-1912.

Mostofi, S. B. (2006). *Fracture classifications in clinical practice*. London; New York: Springer.

Mow, V. C., & Huiskes, R. (Eds.). (2005). *Basic orthopaedic biomechanics & mechano-biology* (3rd ed.). Philadelphia: Lippincott Williams & Wilkins.

Orthopaedic basic science (1994). Simon S. R. (Ed.), American Academy of Orthopaedic Surgeons.

Papini, M., Zdero, R., Schemitsch, E. H., & Zalzal, P. (2007). The biomechanics of human femurs in axial and torsional loading: Comparison of finite element analysis, human cadaveric femurs, and synthetic femurs. *Journal of Biomechanical Engineering, 129*(1), 12-19.

Pacific Research Laboratories, Inc. (2011). Personal communication. January 26, 2011.

Ramos, A., & Simoes, J. A. (2006). Tetrahedral versus hexahedral finite elements in numerical modelling of the proximal femur. *Medical Engineering & Physics, 28*(9), 916-924.

Remiger, A. R., Miclau, T., & Lindsey, R. W. (1997). The torsional strength of bones with residual screw holes from plates with unicortical and bicortical purchase. *Clinical Biomechanics (Bristol, Avon), 12*(1), 71-73.

Resnick, B., Magaziner, J., Orwig, D., & Zimmerman, S. (2002). Evaluating the components of the exercise plus program: Rationale, theory and implementation. *Health Education Research, 17*(5), 648-658.

Richards, R. H., Palmer, J. D., & Clarke, N. M. (1992). Observations on removal of metal implants. *Injury, 23*(1), 25-28.

Rosson, J., Egan, J., Shearer, J., & Monro, P. (1991). Bone weakness after the removal of plates and screws. cortical atrophy or screw holes? *The Journal of Bone and Joint Surgery.British Volume, 73*(2), 283-286.

Rudman, K. E., Aspden, R. M., & Meakin, J. R. (2006). Compression or tension? The stress distribution in the proximal femur. *Biomedical Engineering Online, 5*, 12.

Sanderson, P.L., Ryan, W., & Turner, P.G. (1992). Complications of metalwork removal. *Injury*, *23*, 29-30.

Seligson, D. (Ed.). (1985). *Concepts in intramedullary nailing*. Orlando: Grune & Stratton.

Shi, X.H., Jiang, W., Chen, H.Z., Zou, W., Wang, W.D., Guo, Z., Luo, J.M., Gu, Z.W., & Zhang, X.D. (2008). The study of mechanical behavior on the interface between calcar-defect femur and restorations by means of finite element analysis. *Applied Surface Science*, *255*, 290-292.

Sobelman, O. S., Gibeling, J. C., Stover, S. M., Hazelwood, S. J., Yeh, O. C., Shelton, D. R., et al. (2004). Do microcracks decrease or increase fatigue resistance in cortical bone? *Journal of Biomechanics, 37*(9), 1295-1303.

Strauss, E. J., Pahk, B., Kummer, F. J., & Egol, K. (2007). Calcium phosphate cement augmentation of the femoral neck defect created after dynamic hip screw removal. *Journal of Orthopaedic Trauma, 21*(5), 295-300.

Szivek, J. A., & Gealer, R. L. (1991). Comparison of the deformation response of synthetic and cadaveric femora during simulated one-legged stance. *Journal of Applied Biomaterials: An Official Journal of the Society for Biomaterials, 2*(4), 277-280.

Testi, D., Viceconti, M., Baruffaldi, F., & Cappello, A. (1999). Risk of fracture in elderly patients: A new predictive index based on bone mineral density and finite element analysis. *Computer Methods and Programs in Biomedicine, 60*(1), 23-33.

Tortora, G. J., & Anagnostakos, N. P. (1987). *Principles of anatomy and physiology* (Fifth ed.). New York: Harper & Row, Publishers, Inc.

Van Lieshout, E. M., Van Kralingen, G. H., El-Massoudi, Y., Weinans, H., & Patka, P. (2011). Microstructure and biomechanical characteristics of bone substitutes for trauma and orthopaedic surgery. *BMC Musculoskeletal Disorders, 12*, 34.

Vishay Measurements Group, Inc. (2010). *Strain gage rosettes: Selection, application and data reduction* (TN-515 ed.).

Vishay Measurements Group, Inc. (1992). *Student manual for strain gage technology* (Bulletin 309E ed.).

Who are candidates for prevention and treatment for osteoporosis? (1997). Osteoporosis International: A Journal Established as Result of Cooperation between the European Foundation for Osteoporosis and the National Osteoporosis Foundation of the USA, 7(1), 1-6.

Zdero, R., Walker, R., Waddell, J. P., & Schemitsch, E. H. (2008). Biomechanical evaluation of periprosthetic femoral fracture fixation. *The Journal of Bone and Joint Surgery.American Volume, 90*(5), 1068-1077.